Ultrafast quasiparticle dynamics and the role of screening in WS_2 monolayers

DISSERTATION
zur Erlangung des akademischen Grades

doctor rerum naturalium (Dr. rer. nat.) im Fach Physik
Spezialisierung: Experimentalphysik

eingereicht an der
Mathematisch-Naturwissenschaflichen Fakultät der
Humboldt-Universität zu Berlin

von
Herrn M.Sc. Stefano Calati

Präsident der Humboldt-Universität zu Berlin
Prof. Peter A. Frensch, PhD

der Mathematisch-Naturwissenschaftlichen Fakultät
Prof. Dr. Caren Tischendorf

Gutachter/innen: 1.
2.
3.

Tag der mündlichen Prüfung:

Declaration of Authorship

I declare that I have completed the thesis independently using only the aids and tools specified. I have not applied for a doctor's degree in the doctoral subject elsewhere and do not hold a corresponding doctor's degree. I have taken due note of the Faculty of Mathematics and Natural Sciences PhD Regulations, published in the Official Gazette of Humboldt-Universität zu Berlin no. 42/2018 on 11/07/2018.
I declare that the written and electronic version of the dissertation written by me in the University Library agrees with the accepted dissertation.

Abstract

The optical properties of transition metal dichalcogenides (TMDC) are dominated by excitons, due to quantum confinement and reduced screening characteristic of their 2D nature. Exactly the screening of the Coulomb interaction (CIA) has a fundamental role in determining the steady-state and dynamic properties of such material. Excitons are particularly sensitive to the dielectric screening of a substrate or, even to dynamic screening originating from the presence of quasiparticles which can be transiently present in the system upon photoexcitation for instance. Time resolved optical spectroscopies are a fundamental tool to investigate non-equilibrium physics of TMDC materials. Previous studies evidenced how different phenomena, such as dynamic screening of the CIA, phase-space filling, scattering, and thermal effects, contribute to the non-equilibrium response of TMDCs. Nevertheless, the comparison between previously reported studies, due to the different experimental conditions, is difficult if not impossible. Furthermore, the role of the screening in the non-equilibrium response of the TMDC is yet to be understood.

I investigate monolayers WS_2 placed on various substrates with time-resolved transmittance/reflectance contras. I report a simple formalism that allows the reliable comparison of the exciton static and dynamic response independently of sample, substrate and measurement technique. This is achieved by the retrieval of the exciton contribution to the dielectric function upon photoexcitation. Moreover, with this formalism I extracted the pump-photon energy and fluence-dependent exciton peak shift and broadening. These quantities are reproduced using a basic two/three-level model which was found in good agreement with the data and supported by a good agreement of the extracted parameters with literature values. Through this model the competition of quasiparticle dynamic screening, scattering and thermal effects was unravelled. The excitons' or QFC's effective impact on the exciton dynamic response is unveiled: the broadening is governed by scattering, specifically QFC-exciton scattering when QFC are present in the system, and exciton-exciton scattering when excitons are present. Regarding the exciton shift, QFC induce a global red-shift of the exciton resonance, reproduced with an effective QFC dynamic screening-induced bandgap renormalization. Excitons, instead, induce a blueshift, which can be reproduced with an effective exciton dynamic screening induced binding energy reduction. It is concluded that the QFC induced red-shift is minor than the exciton-induced blue-shift, for the same excited quasiparticle density. Finally, the influence of the static screening on the non-equilibrium exciton response is addressed. It is found that the quasiparticle scattering and QFC dynamic screening are unaffected by a different dielectric environment. On the contrary, the exciton dynamic screening is more effective for higher dielectric permittivity of the substrate. This effect is tentatively attributed to a higher degree of delocalization of the exciton. Ultimately, this thesis contributes to a comprehensive picture of the non-equilibrium dynamics and the role of screening in TMDC and, possibly, other 2D materials.

Kurzzusammenfassung

Die optischen Eigenschaften von Übergangsmetall-Dichalcogenide (TMDC) werden aufgrund des Quanteneinschlusses und der geringen Abschirmung, die für ihre zweidimensionale Natur charakteristisch sind, von Exzitonen dominiert. Gerade die Abschirmung der Coulomb-Wechselwirkung (engl. Coulomb interaction CIA) spielt eine entscheidende Rolle bei der Bestimmung der stationären und dynamischen Eigenschaften derartiger Materialien. Exzitonen reagieren besonders empfindlich auf die dielektrische Abschirmung eines Substrats oder sogar auf die dynamische Abschirmung von Quasiteilchen, welche z. B. nach Photoanregung vorübergehend im System vorhanden sein können. Zeitlich aufgelöste optische Spektroskopien sind ein grundlegendes Instrument zur Untersuchung der Nicht-Gleichgewichtsphysik von TMDC-Materialien. Frühere Studien haben gezeigt, wie verschiedene Phänomene wie etwa dynamische Abschirmung der CIA, Phasenraumfüllung, Streuung oder thermische Effekte zur Nicht-Gleichgewichtsdynamik von TMDCs beitragen. Allerdings ist der Vergleich zwischen bisherigen Studien aufgrund der unterschiedlichen Versuchsbedingungen schwierig, wenn nicht sogar unmöglich. Außerdem ist die Rolle der Abschirmung für die Nicht-Gleichgewichtsdynamik von TMDCs noch nicht geklärt.

Ich untersuche WS2-Monoschichten auf verschiedenen Substraten mit zeitaufgelösten Transmissions-/Reflexionskontrasten. Ich stelle einen einfachen Formalismus vor, der den zuverlässigen Vergleich der statischen und dynamischen Reaktion der Exzitonen unabhängig von der Probe, dem Substrat und der Messtechnik ermöglicht. Dies wird erreicht, indem der Beitrag des Exzitons zur dielektrischen Funktion bei Photoanregung ermittelt wird. Darüber hinaus habe ich mit diesem Formalismus die Pump-Photonen-Energie und die fluenzabhängige Exziton-Peakverschiebung und -Verbreiterung extrahiert. Diese Größen werden durch ein grundlegendes Zwei-/Drei-Niveau-Modell reproduziert, das die experimentellen Daten beschreibt und überdies durch eine gute Übereinstimmung der extrahierten Parameter mit Literaturwerten unterstützt wird. Mit Hilfe dieses Modells konnte die Konkurrenz zwischen dynamischer Abschirmung der Quasiteilchen, Streuung sowie thermischen Effekten entschlüsselt werden. Der effektive Einfluss der Exzitonen oder QFCs auf die Dynamik der Exzitonen wird enthüllt: Die Verbreiterung wird durch Streuung bestimmt, bei Anwesenheit von QFC insbesondere durch QFC-Exzitonen-Streuung, und bei Anwesenheit von Exzitonen durch Exzitonen-Exzitonen-Streuung. Was die Exzitonenverschiebung anbelangt, so bewirken QFC eine globale Rotverschiebung der Exzitonenresonanz, die mit einer effektiven, durch QFC-Dynamik verursachten Renormierung der Bandlücke reproduziert wird. Exzitonen induzieren stattdessen eine Blauverschiebung, die mit einer effektiven, durch dynamische Abschirmung der Exzitonen induzierten Verringerung der Bindungsenergie modelliert wird. Es

wird darüber hinaus festgestellt, dass die QFC-induzierte Rotverschiebung bei gleicher Quasiteilchendichte geringer ist als die Exzitonen-induzierte Blauverschiebung. Schließlich wird der Einfluss der statischen Abschirmung auf die Nicht-Gleichgewichts Exzitonendynamik untersucht. Es wird festgestellt, dass die Quasiteilchenstreuung und die dynamische QFC-Abschirmung durch eine unterschiedliche dielektrische Umgebung nicht beeinflusst werden. Im Gegenteil, die dynamische Abschirmung der Exzitonen ist effektiver für eine höhere dielektrische Permittivität des Substrats. Dieser Effekt wird versuchsweise mit einem höheren Grad der Delokalisierung des Exzitons erklärt. Letztlich trägt diese Arbeit zu einem umfassenden Bild der Nicht-Gleichgewichtsdynamik und der Rolle der Abschirmung in atomar dünnen TMDCs und möglicherweise auch in anderen 2D-Materialien bei.

Acknowledgements

First of all, I want to reserve an exceptional thank you to Julia, for supervising my project and your huge help in the last few years. Thanks for allowing me to develop new ideas and always providing the needed adjustment and support. I know that sometimes, maybe, especially when I was writing up thesis and papers, you had to cope with some very very long, sometimes even redundant, phrases that I wrote, but other than the jokes, you really guided my development as a scientist and as a person.

I want to thank Martin Wolf for the opportunity he gave me to work in the Fritz-Haber-institute's amazing facilities and in the PC department's stimulant atmosphere. Furthermore, thank you for reviewing my thesis.

The same thanks are extended to the Humboldt University for providing the infrastructures through my last year of PhD. I want to thank Prof. Dr. Oliver Benson for co-supervising my thesis.

A huge thank goes to Selene because you guided me through my first years of PhD, being a mentor scientifically and non-scientifically. In good memory of the long nights in the lab, the dinners and all the DB.

Obviously I need to thank the eDynamiX group, with all its former and present members, because without you the PhD would have been much much harder. Particular thanks to Lukas, Sam, Sarah and Sesha for the very nice and fundamental discussions. Obviously thank to Subhadra for taking forward the work that I started. Not to forget, Angelika, Boubacar, Elsie, Marco, Philipp, Conny, Sergey, Radoslaw, Katarina, Laura thanks to all of you.

I want to thank all the technicians in the FHI. Sven (Always tutti paletti), Albrecht, Daniel, Harald, Joachim, Reinhard and Patrick for the technical support and the amazing moments! Obviously, a special mention goes to Marcel because of the constant support in and out of the FHI. Not to forget the PC-sek, Daria and Manuel, I can't even say how much you helped me out. Thanks to all the non-scientific staff of the PC department because you fundamentally contribute to make it the amazing place it is.

Talking of the PC department, many thanks to all the scientific staff as well, I had unforgettable memories with so many people that it is impossible to mention all of them. A few special mentions go to Alex for the good times when sharing the office, obviously Ivana and the cool kidz. Thanks to Ralph and Alex because the discussion with you, either in front of a cigarette or in conferences, lead to some breakthrough of my research.

I want to extend a HUGE thank to the people of Mehringdamm 65, present and past members, with whom I shared a house and always had a place that I looked forward to returning to. Suru, obviously, you became more than a friend and this bond is going to last for very long time. It was wonderful sharing those years with

you, sharing the PhD life and all the marvellous moments that are going to stay with me.

Johannes, I can't thank you enough for how good of a friend and a person you are. The super deep discussion on your terrace and the support you gave me are not quantifiable in words.

I want to thank all the other friends that made my years in Berlin unforgettable: Martina, Paolo, Luc, Kathy, Laura, Dennis, Sophie… all the others! I can't name all of you because you are too many.

And now I switch to Italian…

Grazie Simone, siamo amici da una vita e la distanza non è diventato un problema ma anzi, ci ha forse unito ancora di più. Non è possibile quantificare quanto tu sia stato d'aiuto. Sei una persona speciale.

Grazie a tutti gli amici storici, rendete Brescia un posto meraviglioso in cui tornare. Un ringraziamento alle mie fantastiche sorelle, Nicole, Chiara ed Elena, perché la famiglia è sempre la famiglia e non posso quantificare il bene che vi voglio. Siete speciali. Grazie anche a tutto il resto della famiglia Calati e Fusaro.

Ovviamente per finire mamma e papà, come avrei potuto fare tutto questo senza di voi? Grazie mille per avermi sempre lasciato libero di crescere e prendere la mia strada. Sapere di avere delle fondamenta come voi e un posto dove sentirsi a casa non è descrivibile a parole. Grazie.

And to finish, I am sure that I am forgetting someone, because you know, it's me at the end of the day. I would ultimately thank all of you, aforementioned and not, in person.

Contents

List of Figures

List of Tables

List of Abbreviations

BGR	**B**and **G**ap **R**enormalization
BER	**B**inding **E**nergy **R**eduction
FS	**F**used **S**ilica
CIA	**C**oulomb **I**nteraction
QFC	**Q**uasi-**F**ree **C**arriers
BE	**B**inding **E**nergy
TMDC	**T**ransition **M**etal **D**ichalcogenides
CVD	**C**hemical **V**apour **D**eposition
TC	**T**ransmittance **C**ontrast
RC	**R**eflectance **C**ontrast
CB	**C**onduction **B**and
VB	**V**alence **B**and
PSF	**P**hase-**S**pace-**F**illing

Chapter 1

Introduction

Semiconductors were first investigated in the 19th century[1]. Still, it took until 1947, with the invention of the transistor, when they revolutionized the field of electronics, setting the foundations for modern electronic devices. Semiconductors, and silicon in particular, are used to make integrated circuits which are the core of any electronic device. The development from the first computer, which occupied full rooms, passing through the first microprocessor to the contemporary laptops or smartphones that we are using in our everyday life, originated from the refinements in the manufacturing process of silicon. This process led to the miniaturization of the devices and their increase in efficiency. Moore's law [2], which is more of a projection based on historical data than an actual physical law, describes this miniaturization trend by saying that the number of transistors in dense integrated circuits doubles every two years. If this trend was respected up to now, this was mainly due to the miniaturization of the transistors [3], allowing to fit more computational units in the same space by reducing their size, which now is roughly in the range of a few nanometers. Though, we are now reaching a limit. Heat dissipation and quantum effects at the nanoscale threaten the Moore's law [4, 3].

As always, few alternatives to silicon technology have emerged in a scenario where technological progress is reaching a critical limit. For example, one of the most promising candidates to solve the scaling problem of microchips are atomically thin semiconductors [5]. Due to their low dimensionality and high carrier transport properties, 2D semiconductors, and in particular the class of transition metal dichalcogenides (TMDC) [6], offer great potential for being integrated or even wholly substitute silicon-based technology in semiconductor devices [7, 8, 9]. The discovery of MoS_2 being a direct semiconductor [10], when thinned down in their monolayer form, was the starting point that drove exponentially increasing scientific interest in the physics of these materials. Even the use of these materials to make a transistor was already reported in recent years [11, 12], showing promising results. However, before competing with the conventional silicon architecture [13], these devices need optimization [13].

The main difference between silicon and TMDC is the nature of the excited quasiparticles and the optical bandgap. If excited carriers in the conduction band in conventional semiconductors are generally treated as quasi-free particles, this is not the

case for TMDC materials. In fact, the in-plane quantum confinement of the carriers' wavefunction and the reduced screening due to the two-dimensional nature of these materials give rise to strongly bound excitons, a quasiparticle state composed of a Coulomb bound electron and hole, which are stable at room temperature. These room-temperature stable excitons were already observed in quantum wells [14]. The particularity of the TMDC is that excitons are strongly bound, meaning that the exciton binding energy, proportional to the Coulomb interaction (CIA) strength between the electron and hole constituting the exciton, is high. This interaction strength, called exciton binding energy (BE), is on the order of the hundreds of meV, which was not reported before in any other material.

The new exotic and unique physical properties that excitons in TMDC materials display opens up a vast range of applications, not only in the electronic field, but also in the fields of optoelectronics [15, 16], hydrogen production [17], photonics [18], energy conversion and storage [19], sensing [20], and also more exotic applications such as valleytronics [21] or neuromorphic computing [22]. Last but not least, TMDC are very intriguing materials from a fundamental point of view [6].

The main requirement to use TMDC materials in any of the above-listed application fields is that their basic physical properties must be comprehensively understood. This is achieved by understanding the fundamental phenomena that govern the materials properties of TMDC. Let's consider the simple example of a TMDC based transistor. To create a competitive TMDC based device that can compete with silicon-based technology, we first need to understand the key phenomena determining the steady-state and non-equilibrium properties of the material itself. With this, the design process of devices can be made possible so that optimization strategies can be developed.

In particular, the non-equilibrium physics is crucial for using this material in semiconductor devices applications since, for instance in a transistor, when a current is switched on or off, there is an arbitrarily fast transient build-up phase where the properties of the material are not necessarily the same as the steady-state properties. In the non-equilibrium response of a material, a multitude of different phenomena can compete on different timescales. In two-dimensional material particularly, the screening effects play a fundamental role in the steady-state and dynamic response. In fact, the absence of a bulk material that screens the Coulomb interaction means that the electric field lines between the electron and the hole constituting the exciton extend outside of the material itself. This renders monolayer TMDC particularly sensitive to their environment, precisely to the dielectric screening of the Coulomb interaction [23]. The exciton field lines, as a matter of fact, permeate in the dielectric surrounding, such as a substrate, changing the Coulomb interaction strength and determining the excitonic properties [24]. The higher Coulomb interaction strength leads to an increase in the quasi-free particle bandgap of the TMDC. Furthermore, the interaction strength of the CIA between the electron and the hole constituting the excitons determines the exciton binding energy. Thus, the competition between

the two determines the exciton resonance energy.

Changes in the CIA strength can originate from the variation of the dielectric screening. For instance, a substrate with higher dielectric permittivity screens the CIA more effectively, reducing the interaction strength and leading to more loosely bound exciton. Moreover, not only the screening from the dielectric environment contributes to the determination of the exciton energy, but also the dynamic screening resulting from the presence of quasiparticles in the system can influence the electronic band structure of the TMDC. For these materials, in particular, the dynamic screening plays a crucial role [25, 26]. During non-equilibrium transients, excited quasiparticle populations are present in the system, screening the CIA and changing the excitonic properties [27].

Now, the excited state population in semiconductors relaxes on timescales that range between femtosecond to nano [28] or even microsecond [29]. Another factor to consider is that the strong light-matter coupling that characterizes the TMDC materials guarantees that the excitons dominate the optical response. The last two facts are then the main reason why it is convenient to use ultrafast time-resolved optical techniques to investigate the non-equilibrium physics of these materials. Specifically, ultrafast time-resolved optical spectroscopy allows perturbing the system out of its equilibrium, such as photo-generating an excited particle population in the system. Simultaneously, the probe monitors the dynamic material response on timescales that extend down to the tenths of femtosecond timescale, tracking the exciton resonance variations on ultrafast timescales.

Monitoring the exciton resonance on ultrafast timescales is fundamental since the changes of the exciton resonance contain information regarding the main phenomena governing their non-equilibrium response. As a matter of facts, works performing optical pump and probe spectroscopy on WS_2 monolayers were already reported in literature [30, 31, 32, 33, 27, 34]. All these studies retrieve or directly measure various observables, modelled in different ways and for dissimilar excitation conditions. Unfortunately, the consistency between these is not broadly investigated, and all this renders the comparison between the various approaches difficult, if not impossible. Even so, these studies reported exciton peak shift and broadening of the resonance upon photoexcitation. Moreover, those dynamics were attributed qualitatively to multiple causes, among which phase-space-filling effect, thermal effects, dynamic screening of the CIA, and scattering, all competing on different timescales. However, despite the different studies reported in the literature, a comprehensive quantitative picture of the multiple phenomena and their interplay concurring in the observed dynamics is not reported yet.

To provide such a comprehensive picture, tracking the excited particle time evolution is then the key to understanding the fundamental mechanisms governing the exciton dynamic response. Moreover, understanding the quasiparticle specific effects on the dynamic response of the exciton is crucial because of the different nature of the dynamic screening originating from excitons or QFC. To complicate the

scenario, as mentioned before, the screening of the Coulomb interaction is not the only mechanism determining the exciton response after photoexcitation since other competing effects, such as thermal effects[32], phase-space filling effects [34], defect trapping [35], or the generation of multi-particle state [36], can be present simultaneously. Particular attention must be taken to disentangle all these competing effects and isolate each of every contribution. This is the path to determine the specific role of the static and dynamic screening in the exciton dynamic response, as stated by the title of this thesis. This would ultimately bring new insight toward a complete understanding of the non-equilibrium dynamics in TMDC and other 2D materials.

In summary, the univocal understanding of the non-equilibrium dynamics in TMDC and other 2D materials is thus essential for future applications of such materials and from a fundamental point of view. Firstly, it is necessary to retrieve quantitative information about the exciton steady-state and dynamic response independently of the sample, substrates, and measurement technique, enabling a reliable comparison between different experiments. To do that, a proper formalism describing the light-matter interaction of these materials is required. Once this formalism is established, the fundamental questions that are investigated are outlined in the following. First, how does the screening of the CIA influence the steady-state and, in particular, the non-equilibrium properties of TMDC material? On top of this, how is the interplay of static and dynamic screening and other phenomena such as ultrafast thermalization or phase-space filling? Eventually, is it possible to unravel how different quasiparticles, such as quasi-free carriers and excitons, affect the non-equilibrium response and through which relaxation mechanisms and pathways they relax after a perturbation? By answering all these questions, we can provide, or at least contribute to, a comprehensive picture of the non-equilibrium dynamics in TMDC and other 2D materials and their transient properties.

The approach used in this work to find an answer to all these questions is outlined in the following.

Outline of the thesis: The second chapter discusses the main physical, electronic and optical properties of low-dimensional TMDC materials, focusing on the new exotic phenomena that arise when a system transitions to the two-dimensional state. In particular, the Coulomb-bound quasiparticle constituted by an electron and a hole, called an exciton, is introduced, and the effects that a variation of the screening of the Coulomb interaction, originating from the dielectric environment or the presence of other quasiparticles, have on the excitonic properties of the material is outlined. The third chapter introduces the fundamental theoretical basis of light-matter interaction that is necessary in order to investigate those low-dimensional materials quantitatively with optical techniques. Eventually, the next chapter specifies the experimental techniques of time-resolved reflectance/transmittance contrast (tr- RC/TC) used throughout this work to access the non-equilibrium optical response of monolayers TMDC.

Finally, before showing the results, Chapter 5 reviews the available literature on

the non-equilibrium dynamical response of TMDC, recalling and contextualizing the above mentioned scientific question that this thesis aims to answer.

Chapter 6 presents the results of this work. Specifically, the first part derives a formalism that allows the quantitative comparison of the exciton static and dynamic response in WS_2 monolayers from independent time-resolved optical spectroscopy experiments. This is achieved with two different models to retrieve and track the exciton contribution to the complex dielectric function in the steady-state and dynamic response upon photoexcitation of monolayer WS_2 deposited on two different substrates from two independent measurement techniques. Comparing these two experiments shows that slight differences in the dielectric environment impact the steady-state exciton absorption, but the dynamic response is left unaffected. This suggests that the exciton dynamic response depends on the excitation conditions and, in particular, on the initial excited quasiparticle density.

To test this hypothesis, in the second part of the chapter 6, the pump photon energy and fluence dependence of the exciton dynamic response upon photoexcitation for a monolayer WS_2 placed on a Si/SiO_2 substrate, extracted from tr-RC measurements, are investigated. By modelling the excited quasiparticle population with a simplified phenomenological two/three-level model, the relaxation mechanisms governing the recovery of the system back to equilibrium after photoexcitation are unveiled, as well as determining the exciton formation time, exciton linear recombination lifetime, and the rate of the Auger recombination, respectively, all in good agreement with literature values. The consistency of this model with the experimental data supports this essential view of the dynamic exciton response. It allows the disentanglement of the thermal, exciton, and free carrier effective contribution to the exciton peak shift and broadening. The resulting effect of the competition of exciton binding energy reduction and quasi-free particle bandgap renormalization is captured quantitatively in this two/three-level model. The different exciton peak shift originates from the different quasiparticle dynamic screening of the attractive and repulsive Coulomb interaction. Particularly, the effective role of the QFC is pictured in the model through a QFC induced broadening of the exciton resonance through QFC-exc scattering. Additionally, QFC are largely responsible for band gap renormalization through dynamic screening. The effective exciton contribution, instead, consists in a blueshift of the excitonic resonance, modelled with an effective binding energy reduction as the dominant source of peak shift. In addition, the presence of excitons induces broadening of the resonance through exc-exc scattering. Furthermore, the QFC effective dynamic screening results in a red-shift which is minor than the exciton induced blueshift per unit of quasiparticle. The presence of double the amount of QFC with respect to excitons, though, explains the comparably larger effect of a QFC density on the exciton peak shift. The model is an effective model, meaning that the real changes of the binding energy and bandgap are not isolated but the resulting effect of their competition. Nevertheless, assuming that the QFC screen the Coulomb interaction more effectively than excitons, due to the

localized nature of the latter and their lower polarizability, the relative weight of the single effects can be analyzed. The conclusion is that the exciton induced quasi-free particle bandgap renormalization is the weaker contribution, followed by the exciton induced binding energy reduction. For the same absorbed photon density, the QFC induced bandgap renormalization is stronger than the corresponding binding energy reduction. The last two effects, within the approximation of QFC more effectively screening the Coulomb interaction, are also stronger than the exciton induced ones. This provides an estimation of the relative strength of the dynamic screening induced effect concurring to the exciton peak shift upon photoexcitation.

The last part of chapter 6 investigates the correlation between the static dielectric screening of the Coulomb interaction and the exciton dynamic response upon photoexcitation. The tr-TC in a monolayer WS_2 placed on a sapphire substrate is studied. By extracting the time-dependent exciton contribution to the dielectric function upon photoexcitation and fitting the latter with the two/three-level model developed in the previous sections, it is evidenced that a different dielectric environment does not influence the linewidth broadening, therefore the exc-exc and QFC-exciton scattering, nor the QFC induced dynamic screening of the Coulomb interaction. Instead, the exciton dynamic screening is dependent on the dielectric environment. This may be attributed to a higher degree of delocalization of the excitons when placed in a more effectively screened environment.

Lastly, chapter 7 summarizes the conclusions of the result section to outline a comprehensive picture of the effect of the screening of the Coulomb interaction in the steady-state and dynamical response of the exciton upon photoexcitation in monolayers WS_2, ultimately providing a comprehensive picture of the non-equilibrium dynamics in this and other 2D materials' transient properties.

Chapter 2

Transition metal dichalcogenides

Transition metal dichalcogenides acquired substantial scientific interest thanks to their relevance in electronic applications, to the point that they are considered as the main candidate to substitute conventional silicon-based electronics, as already mentioned in the introduction. The main reason for this is the fact that they are low dimensional semiconductors since they can be thinned down to the monolayer form. This renders them ideal for the miniaturization of electronic circuits when used in combination with other 2D materials.

From a more fundamental point of view, atomically thin TMDCs are also relevant since they display new exotic physical properties. In particular, they show excitons, a Coulomb bound quasiparticle constituted by an electron and a hole with binding energies in the order of the hundreds of meV, rendering them stable at room temperature. Such excitons offer intriguing possibilities for many applications of such materials in semiconductor devices and more [37]. Furthermore, the energetic structure of these materials offers valley selective coupling to circular light, thus providing an ideal candidate for spintronics applications. The main physical phenomena behind the exotic physical properties of these materials that render them so promising were the topic of research in the last 15 years, after the first observation of the monolayer TMDC was reported.

This chapter aims to provide a review of exactly the basic physical properties of TMDC monolayers. The first section focuses on the fundamental electronic and optical properties of those materials. In particular, the changes arising when the bulk material is thinned down to its monolayer form and how the aforementioned properties change. It then introduces the concept of exciton, discussing its optical properties and ultimately the effect that external factors, such as temperature, have on them. The second section focuses on the role of the screening in influencing the exciton properties of TMDC. Precisely, the effect of static and dynamic screening are discussed in detail. The main points that are introduced and discussed in the chapter are finally summarized in the last section.

Due to the relatively recent discovery and scientific interest in monolayer TMDC materials, books about them are not numerous yet. Therefore the following chapter is based on the available literature of scientific papers and reviews, which will be expressly referenced.

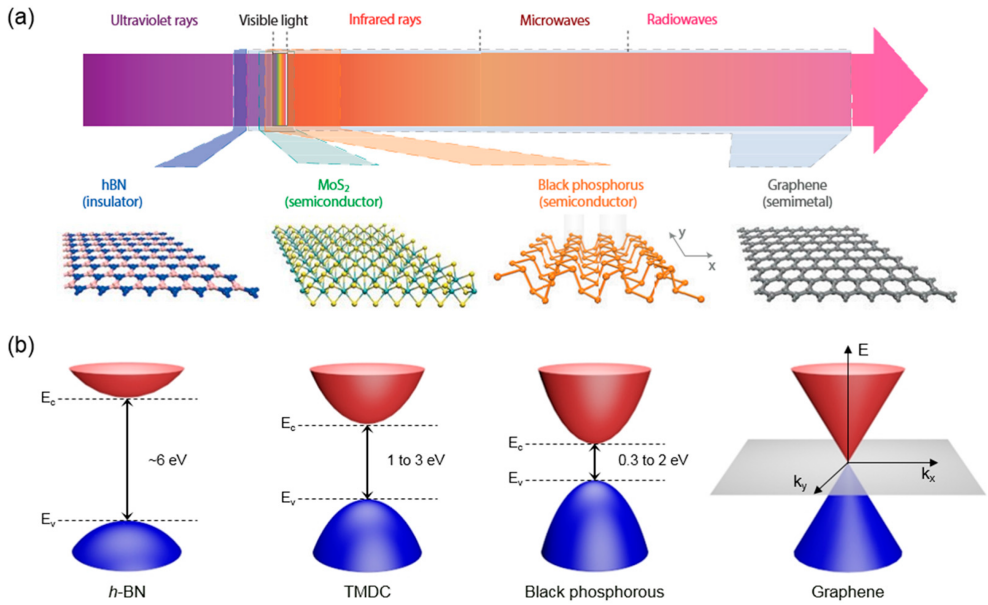

FIGURE 2.1: a) Bandgap energy range in the electromagnetic spectrum spectrum and b) sketch of electronic structures of various two-dimensional (2D) material. Figure taken from [44]

2.1 Low dimensionality and transition metal dichalcogenides

When transitioning from a 3D to a 2D geometry, new exotic physical properties of a material or a system arise. Let us take, for example, graphite. When it gets thinned down to a monolayer, we obtain graphene [38], which is the prototypical example of 2D material. In this case, Graphene is a semimetal that displays remarkable mechanical, electric and thermal properties with respect to its bulk counterpart [39, 40]. After the discovery of the graphene [38], in later years, the research on two-dimensional materials continuously increased [41], eventually leading to the discovery of new low dimensional materials, such as HBN [42], black phosphorus [43] and the whole class of TMDC material[10] . The combination of these 2D materials offers strong potential for a new generation of miniaturized electronics and opto-electronics devices [44]. Fig. 2.1 shows why these materials are so important and potentially relevant for device applications since they cover a huge part of the electromagnetic spectra. Particularly, Graphene is a semimetal, the black phosphorous a narrow band semiconductor, the TMDC semiconductors with a bandgap in the visible range, and HBN a wide bandgap semiconductor. The combination of these materials through stacking or lateral heterojunctions offers the ability to create heterostructures that have relevant applications for miniaturized devices [7].

In this thesis, we focus on the investigation of TMDC materials. As a matter of fact, this class of materials, after the discovery [10] of the monolayer MoS_2, became one of the most promising candidates to substitute conventional semiconductors in electronics applications. In particular, with this work, we will focus our attention on the investigations of the optical response of a monolayer WS_2, one of the most

extensively studied TMDC after MoS_2.

This section discusses the theoretical background and main properties of these materials, and it is structured as follows. The first part discusses the main differences between the TMDC monolayer form and its bulk counterpart. Secondly, the details of highly bound excitons, the quasiparticle constituted by an electron and a hole that are bounded due to Coulomb interaction, are introduced. These quasiparticles will be introduced and described in the second section. Particular focus will be given in the third section to the novel optical properties that the excitons display. Finally, we will review the primary studies regarding the influence of external factors, particularly the temperature, have on the excitonic properties of the WS_2 on them. The influence of the screening requires a separate section, and it is discussed in section 2.2.

2.1.1 Atomically thin TMDC

TMDC, in their bulk form, are known materials and were already investigated in the seventies [45]. As mentioned in the introduction, these materials attracted much interest in recent years, when the mean of isolating thin or even monolayers became available. However, the physical and optical properties of the low dimensional crystals differ substantially from their bulk counterpart [46].

In this subsection, we will describe the main physical properties of TMDCs and how these change when these materials are thinned down to their monolayer form. Particular focus is given to the structural properties of both bulk and monolayer forms, their corresponding electronic band structure and the fundamental optical selection rules derived from symmetry considerations.

Transition metal dichalcogenides are Van der Walls layered materials in their bulk form with the chemical formula MX_2, where the most common elements are M=Mo,W and X=Se,S. These materials are stable at room temperature and ambient pressure.

The crystalline structure of the bulk TMDCs is characterized by a D6h point symmetry group in their bulk form and 2H phase, as shown in Fig. 2.2.a). The atoms are disposed in a trigonal prismatic structure. The layers are organized such that every second layer is rotated by 180 degrees, thus the basic unit cell possesses inversion symmetry, and it contains atoms from two layers. Furthermore, in the same figure, the sketch of the top view of the crystal clearly shows the hexagonal in-plain structure that these materials display in the 2H phase.

Using exfoliation [10] or chemical vapour deposition [48] techniques, it is possible to obtain monolayers or few-layers thick samples. In the case of a single monolayer, the crystalline structure is characterized by the D3h symmetry group. The unit cell of the monolayer consists of only half of the bulk counterpart, and it possesses broken inversion symmetry, as it is shown in Fig. 2.2.a).

When we analyze the electronic band structure [47], shown in Fig. 2.2.c), and the corresponding Brillouin structure, (Fig, 2.2. b) we evince that the bulk material

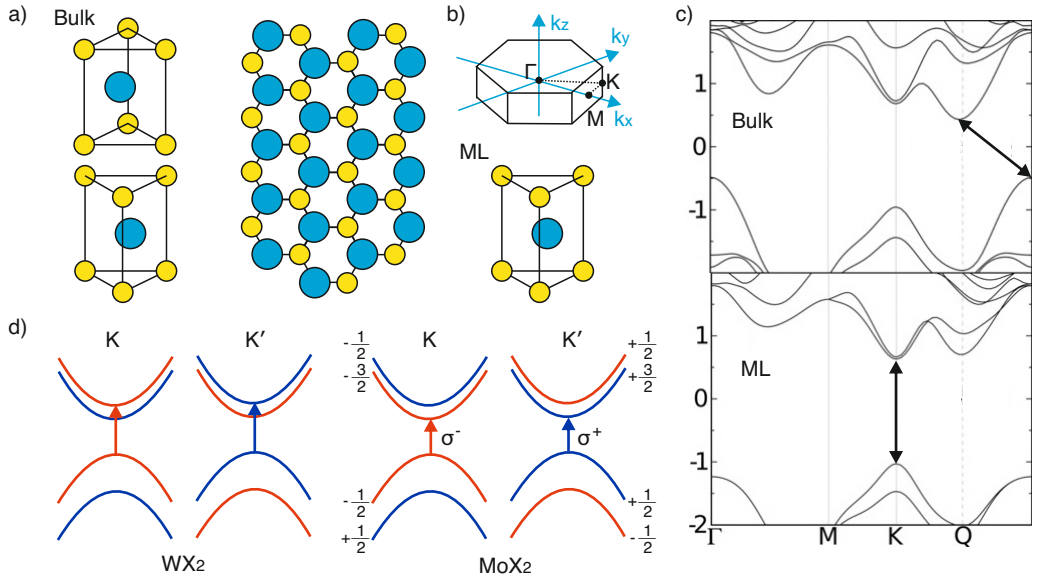

FIGURE 2.2: a) Unit cell of bulk and monolayer (ML) and corresponding Brillouin zone of TMDC. Top view of crystalline structure. c) Band structure of bulk and monolayer TMDC. Figure taken from [47]. d) Valley degeneracy and optically allowed transition.

is an indirect semiconductor. In fact, the top of the valence band is at the Γ point. Instead, the conduction band minimum is located at the Q point, located between the K and gamma points. On the contrary, the band structure of the monolayer WS_2 shows a direct semiconductor, with the bandgap at the K point, as clearly visible in Fig. 2.2.c).

Another essential property of such materials is their valley selectivity. Due to strong spin-orbit coupling [49] the valence band splits by hundreds of meV. Other than the spin splitting of the valence band, the conduction band also undergo spin-orbit splitting, even though with a smaller amplitude than in the valence band [50]. A finite split in the orders of the tenths of meV is then present in the conduction band. This splitting of both conduction band and valence band allows the coupling of circularly polarized light, characterized by positive or negative helicity, with the specific transition occurring at the K or K' valley [51]. This phenomenon gives rise to optical selection rules sketched in Fig 2.2.d). The selection rules can be formalized by giving the quantum numbers m +1/2 and -1/2 to the valence bands at the K valley spin-up and spin-down, respectively [52]. Instead, the conduction bands have quantum numbers -3/2 and -1/2 for the spin-down and spin-up. For time-reversal symmetry, the sign changes at the K' valley. When circularly polarized light, carrying angular momentum 1, is incident on the sample, only specific transitions that conserve the spin are allowed as sketched in Fig. 2.2.d). The peculiarity here is that the electronic transition between the top of the VB and the lower CB at the K valley in Mo-based monolayers is an optically allowed transition since a left circularly polarized light carries $\Delta m = -1$ momentum and conserves the spin. Analogously,

at the K' valley right circularly polarized light couples to the intra-valley transition. Instead, in W based monolayer, the allowed transition is the one to the higher lying CB.

This difference is fundamentally important and must be considered when analyzing electron or quasiparticle dynamics in TMDC. Further explanation of this is given in section 2.1.3, but before that, it is necessary to introduce the concept of exciton. In fact, the selection rules introduced in this section arise from purely symmetry reasons, and they are valid in terms of a one-particle picture, where the Coulomb interaction between electrons and holes is ignored. This approximation is not accurate for TMDC materials though, as we see in the next subsection.

2.1.2 Excitons in 2D semiconductor

The derivation of the fundamental optical properties and selection rules of TMDC materials described in the previous section was made in a single-particle approximation. This approximation means that the electrons are considered in a single electron state and do not interact with other electrons, phonons or lattice. This assumption is not valid in the case of low dimensional TMDC. Due to reduced screening in fact, the electrons interact with the corresponding hole through electrostatic force. In this section, the results and effects of this non-negligible interaction are discussed.

Generally, in a semiconductor, when an electron is promoted from the valence band to the conduction band, it leaves a hole in the valence band. If the Coulomb interaction between these two carriers is strong enough, they form a quasiparticle called an exciton [53]. This quasiparticle is simply a bound state formed by an electron and a hole that interacts with each other due to electrostatic attraction. The interaction strength between the constituting particle is also called exciton binding energy, corresponding to the energy required to bring the constituting electron and hole to the quasi-free state, where they do not interact anymore through Coulomb force. Excitons are charge neutral and are free to move in a solid. In terms of energetic structure, the exciton is represented as an energy level bounded with respect to the quasi-free particle bandgap by the exciton binding energy amount, as sketched in Fig. 2.3.a).

In general, there are two formalisms to describe excitons in solids, corresponding to Frenkel excitons or Warnier-Mott excitons. The main difference between the two formalisms is in the level of localization (i.e. spatial extension) of these excitons with respect to the atomic displacement in a lattice. When the spatial extent of an exciton is comparable to the average distance of the atoms in a lattice, then the Frenkel exciton formalism [55] is used. In this case, the high degree of localization is due to strong Coulomb attraction, corresponding to a high exciton binding energy. Instead, when the Coulomb interaction is weaker, the exciton can be delocalized on multiple unit cells and in this case, it can be described with the Wannier-Mott formalism [56]. Generally, the average distance of the electron and the hole constituting an exciton is defined as the Bohr radius.

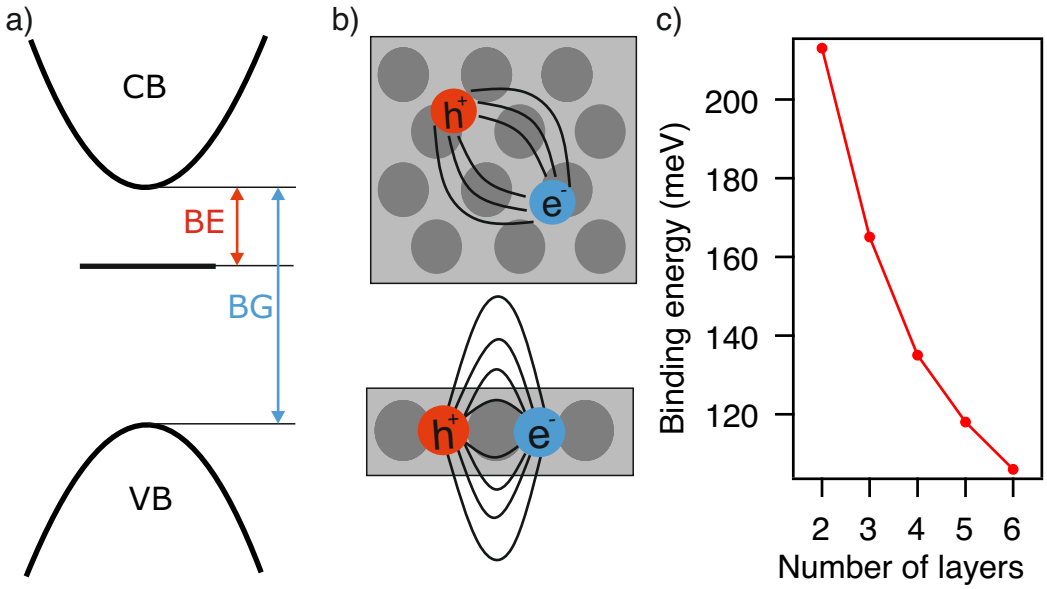

FIGURE 2.3: a) Sketch of exciton energy level, b)sketch of exciton in bulk and monolayer, showing quantum confinement and reduced screening. c) Binding energy as a function of number of layers of Black phosphorus, data digitized form [54]

The main factor defining the Coulomb interaction strength of the electron and hole forming an exciton is the screening. The more the exciton is screened, the weaker the Coulomb interaction strength is, leading to lower binding energies, thus more delocalized excitons. When transitioning from a solid to a thin film or even to atomically thin material, the exciton localization and screening change drastically, and particular consideration must be taken into account. First, the electron and hole wavefunction overlap is restricted along one direction, in what is called quantum confinement, since both the electron and hole are confined in the plane. Secondly, the electric field lines between the electron and the hole can penetrate outside the monolayer material, as sketched in Fig. 2.3.b). If we assume a suspended monolayer, the electric field lines between the electron and the hole constituting the exciton are not screened by the media in the surrounding, as it happens for the bulk material shown in Fig. 2.3.b). Therefore, the reduced screening in the low dimensional case increases the coupling strength of the electron and the hole, thus leading to higher binding energies for the 2D case with respect to the bulk. This effect is visible for the case of black phosphorous as reported in [54] and shown in Fig. 2.3.c). In this figure, the exciton binding energy is displayed as a function of the number of layers, therefore the thickness, of the constituting material. It is clearly seen that, by increasing the thickness of the sample, the binding energy decreases.

In this section, we introduced the exciton, described its origin, and its enhancement in 2D materials due to quantum confinement and reduced screening. The role of the screening is quite involved since it depends mainly on the environment but also on the presence of quasiparticles in the system. This topic requires a separate

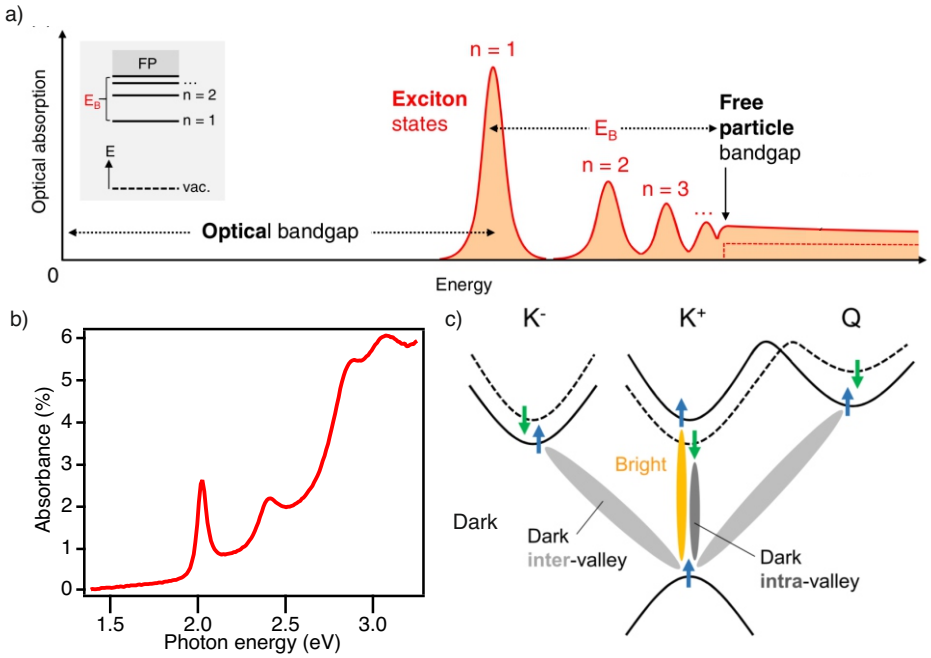

FIGURE 2.4: a) Optical absorbtion spectra of an excitonic series of a ideal 2D semiconductor and corresponding energy levels in the inset. Taken from [6]. b) Absorbance of a monolayer WS_2 as a function of photon energy. Data digitized from [57]. c) Sketch of optically bright and dark excitons, taken from [6]

section and will be discussed in section 2.2. Before discussing the influence of the screening on the excitons, it is necessary to recall the optical selection rules, introduced at the end of subsection 2.1.1, to discuss the optical properties of the monolayer TMDCs. This will be done in the following subsection.

2.1.3 Optical properties

In the previous sections, we introduced the basics of the electronic band structure of the monolayer TMDCs, and we defined the concept of excitons. Due to the strong light-matter interaction in TMDC materials, excitons are commonly investigated using optical techniques. In fact, excitons have a clear and distinct signature in the optical spectra, which carries information about the fundamental physical processes governing its response.

This section aims to provide the basic optical properties of exciton in TMDCs, explaining how they appear in optical spectra, discussing the fundamental optical transitions that can occur and the respective selection rules, which determines the bright or dark nature of an exciton.

In section 2.1.2, we saw that the exciton energy level corresponds to a bound state, with reference to the quasiparticle bandgap, by an amount called binding energy. These excitons appear in optical spectra as a resonance with energy corresponding to the difference of the quasi-free particle bandgap and binding energy. In that case, we mention only the ground state of the exciton. It has been shown that

excitons exhibit a series of excited states [58] that, analogously to the Rydberg series for the H atom, consist of a discrete number of energy levels to which a quantum number n is assigned. n is the principal quantum number, and it determines the binding energy of the respective excited state. The excited states correspond to specific degrees of freedom for the relative motion of electron and hole constituting the exciton. The inset of Fig. 2.4.a) shows the energetic structure corresponding to the series of excited excitonic states for an ideal 2D semiconductor. The energy spacing becomes smaller the higher the quantum number, up to the continuum of state of the quasi-free particle band gap, which is the excited state with $n = \infty$. This energetic structure has a clear signature in the optical spectra as displayed in Fig. 2.4.a). Here, resonances in the absorption spectrum, corresponding to the ground excitonic state and excited states, are visible below the quasi-free particle conduction band for an ideal semiconductor. It is also important to mention that the absolute energy of the exciton ground state is often referred to as the optical bandgap.

What has been discussed so far was referring to an ideal 2D semiconductor. The real absorbance spectrum of a monolayer WS_2 measured by [57] is reported in Fig. 2.4.b). Resonant contributions in the absorption spectra are visible, the lowest of which corresponds to the ground state of the A exciton. Other excitonic absorption features are present in the spectra at higher energies, corresponding to higher-lying electronic transition and not to the excited series of the A exciton. In particular, the peak at 2.4 eV photon energy corresponds to the B exciton [59], when an electron is excited from the lower valence band to the conduction band, and the other peak at 2.9 eV is often referred to as C exciton [60], corresponding to the excitation at the gamma point in the band structure.

We now have discussed the optical response of monolayer TMDC. It is now important to discuss the optical selection rules. Excitons are composed of an electron and a hole, and if the latter one tends to be in the upper valence band at the K or K' point, the electron can be in a different position in the band structure. Nevertheless, excitons can be optically generated only at a specific point of the band structure and can recombine in different ways, either radiatively or non radiatively. A proper understanding of optically allowed/not allowed transition is fundamental, as outlined in the following.

In section 2.1.1, we saw how the spin-orbit coupling induces spin splitting of both the valence and conduction bands, giving rise to intra-valley spin selection rules. This set of rules arise from purely lattice symmetry reason, and therefore they are valid also for the excitons. In W-based TMDCs, excitons can be optically generated only when an electron is promoted to the higher lying conduction band, leaving a hole in the top valence band. This exciton is called bright exciton because it can undergo radiative recombination satisfying the selection rules, as sketched in Fig. 2.4 b). In general, electrons can move to different points of the band structure [61] due to scattering events. When the electron constituting the exciton is at another point in the conduction band other than the upper VB at the K point, it can

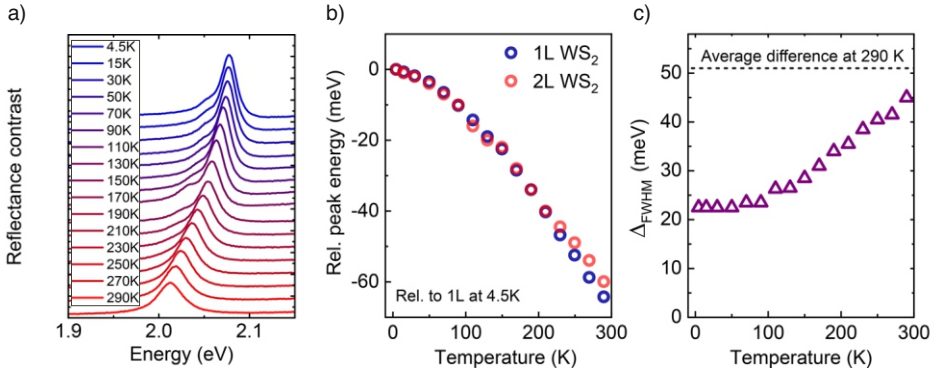

FIGURE 2.5: a) Temperature dependent photoluminescence as a function of photon energy for a monolayer WS_2 and corresponding relative peak energy (b) and FWHM (c) of the exciton with respect to the lowest temperature data. Figures taken from [63]

not undergo radiative recombination due to spin or momentum conservation rules, forming therefore the so-called dark exciton. For example, when an electron is in the lower conduction band at the K point, for instance, direct recombination can not occur because of spin conservation reasons. This exciton is referred to as dark intra-valley exciton. Otherwise, at room temperature, phonons can scatter excitons to either the neighbouring valleys. When carriers are present in the reciprocal valley K^- or at the Q valley, radiative recombination can not occur because of momentum conservation, and it requires a scattering event to occur. These excitons are then called dark inter-valley excitons. These dark excitons, as the name suggests, are not visible in optical spectra. The first experimental evidence of the dark intra-valley exciton was performed by brightening it with a magnetic field [62].

The fundamental point is that despite these dark excitons are not clearly visible as their name suggests, they are present and influence especially the dynamic response of the exciton upon photoexcitation. Therefore, they need to be considered when investigating TMDC materials.

The basic optical properties and the exciton signature in the optical spectra were then provided, and the presence of bright and dark exciton was discussed. Now that it is clear how optical measurements can be insightful regarding the excitonic properties of TMDC materials, we can discuss the influence of external factors on the excitonic properties.

2.1.4 Factors influencing the excitonic resonance: Influence of temperature

We saw the fundamental physical properties of monolayer TMDC material and the basics of their optical response. One crucial aspect to consider when working with these materials is the role that external influences have on the excitonic properties. Many factors can contribute to changing such properties, such as as environment

[64], preparation technique [65], defect density [65], doping [26], strain [66], and temperature [67].

In this subsection, we discuss the role that temperature has on the excitonic resonance and how the optical signature of the exciton changes with temperature, providing the explanation of the physical mechanism behind such changes.

In general, in semiconductors, the temperature can influence the physical properties of the material [68]. In the case of TMDC, non trivial temperature-induced broadening and shift of the excitonic resonance were reported in literature [63, 69, 70, 71, 72, 73]. Fig. 2.5.a) shows the result obtained from Raja et al. [63], where they measure the reflectance contrast of a monolayer WS_2 as a function of the photon energy for different temperatures. Their main observation is that the exciton absorption redshift and broadens with increasing temperature. They also extract both the peak shift and broadening as a function of temperature, which are reported in Fig 2.5.b) and Fig 2.5.c), respectively, as a function of temperature.

The peak shift originates from a renormalization of the quasi-free particle bandgap due to lattice expansion. Furthermore, the renormalization of the transition energy occurs due to a polaron, a phonon-assisted polarization of the material [74]. The broadening instead is caused by multiple factors discussed in detail in [70, 75]. In an attempt to simplify this complex topic, we can intuitively understand that the broadening generates from the higher carrier-phonon scattering, which increases with increasing temperature.

It is immediately evident how the temperature-dependent trends of broadening and peak shift and their quantitative description are non-trivial. Nevertheless, it is sufficient for the measurements in this work to approximate the temperature-dependent shift and broadening with a linear scaling. Such approximation is valid for small changes of temperature in the proximity of room temperature. This approach was discussed and performed by [32], and they found, by comparing different experiments, that the temperature-induced shift is comprised between 0.25 and 0.5 meV/K. The temperature-dependent linewidth broadening instead returns a value between 0.12 to 0.25 meV/K for small temperature changes in the proximity of room temperature.

In conclusion, we summarized the effects of temperature on the excitonic resonance, which induces redshift and broadening. Temperature is not the only factor influencing the excitonic resonance. Many other factors can renormalize the TMDC energetic structure or change the optical response. On top of all the screening of the Coulomb interaction that is discussed in the next section.

2.2 Role of the screening

We already saw in the previous section how the screening, particularly due to the 2D nature of a material, is a critical factor in determining the exciton physical and optical properties. We saw how, in the case of a monolayer TMDC, the field lines between

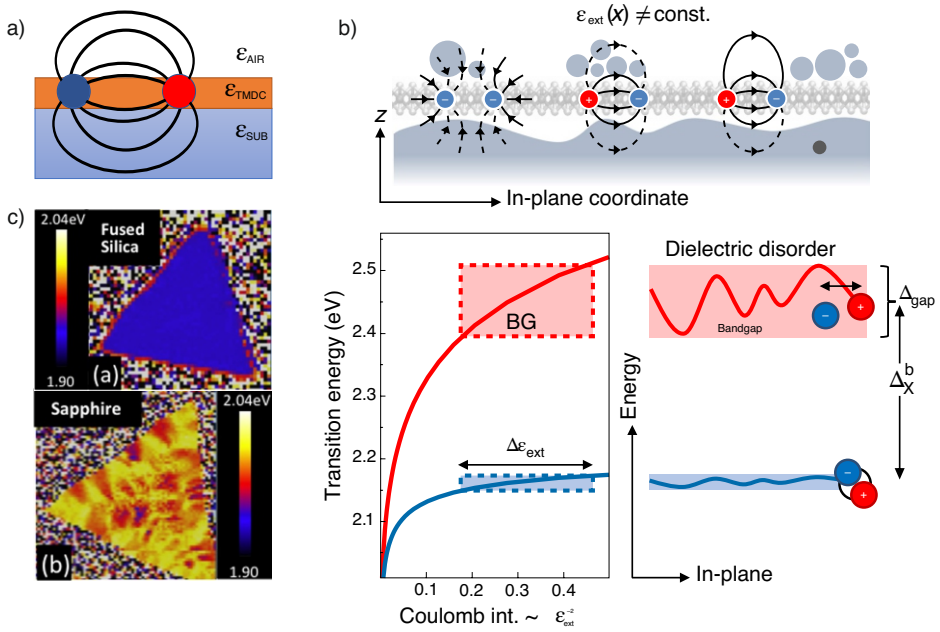

FIGURE 2.6: a) Sketch of exciton screened by a substrate with reladive dielectric constant $\varepsilon_s ub$. b) Top: sketch of dielectric disorder. Bottom: Transition energy for quasifree particle bandgap and optical bandgap as a function of Coulomb interaction strength, with corresponding inhomogeneous broadening. Figure taken from [76]. c) Photoluminescence map of two monolayer WS_2 placed on Fused silica and sapphire substrates. Figure taken from [77].

the electron and the hole constituting an exciton extend outside the material. This renders the TMDC particularly sensitive to their environment because, generally, such monolayers are supported on a substrate. The substrate, and more in general the dielectric surrounding, screens the Coulomb interaction of the exciton, therefore changing the excitonic properties of the TMDC. In particular, the screening of the Coulomb interaction can happen through static screening due to the environment, more precisely from the substrate, impurities, and absorbates, but can also originate from the presence of quasiparticles in a dynamic fashion.

This section aims to review and unravel the influence of both static and dynamic screening on the exciton properties of a monolayer TMDC. The first subsection will focus mainly on the static screening and how the environment influences the properties of the exciton. The second part deals with the dynamic screening that originates from the presence of quasiparticles in the system.

2.2.1 Dielectric environment

Generally, monolayers TMDC are placed on a substrate and the latter influences their physical properties [78]. Recalling the discussion of Section 2.1.2, we saw that the field lines between the hole and electron constituting the exciton permeate outside the monolayer. It then becomes apparent how a substrate can influence the

Coulomb interaction simply by screening the electric field lines between the particles constituting the exciton.

In this subsection, we discuss the influence of the dielectric surrounding on the excitonic properties of TMDCs. In particular, we discuss how the substrate and the local dielectric disorder influence the excitonic properties.

Fig. 2.6.a) shows the typical case of a monolayer of TMDC supported on a substrate of dielectric permittivity ε_{sub}. The field lines of the exciton permeate into the substrate, which screens the electric field, resulting in the reduction of the Coulomb interaction strength. The screening of the Coulomb interaction leads to the reduction of the binding energy, in analogy to the increase in the number of layers discussed in section 2.1.2. Furthermore, Reducing the Coulomb interactions strength between charge carriers induces the renormalization of the quasi-free particle bandgap. The interplay of binding energy reduction and bandgap renormalization results in a small shift of the absolute exciton energy, despite the substantial bandgap and binding energy changes.

The most simplistic scenario, assuming that the sample is in air and an infinitesimally thin monolayer, is that the Coulomb interaction strength will be inversely proportional to $(\varepsilon_{r_{sub}} + \varepsilon_{air})/2$. This assumption is a rough approximation but provides a general understanding of the trends. The specific influence of the Dielectric environment and, in particular, the choice of the substrate was carefully investigated in [79, 23, 80].

Another significant aspect that needs to be taken into account is the local variation of the dielectric environment. In their work, Raja et al. [76] demonstrated that the local variations of the environment have a finite effect on the excitonic optical properties of the material. In particular, impurities, absorbates, or slightly different distance between the monolayer and the substrate alters the energetic structure of the monolayer locally, as sketched in the top panel Fig. 2.6.b). In the bottom panel of Fig. 2.6.b) the bandgap and the absolute exciton energy of a monolayer WS_2 are reported as a function of the Coulomb interaction strength. When local variations due to impurities, for instance, or to a slightly different distance between the monolayer and substrate are present, the exciton absolute energy varies accordingly. When measuring the macroscopical exciton response, this contains inhomogeneous contributions due to the average over locally different responses. Local dielectric inhomogeneities result in a smaller variation of the absolute energy position of the exciton with respect to the change of the quasi-free particle bandgap. This is because the binding energy also reduces proportionally to the Coulomb interaction strength, and the later effect partially cancels out the bandgap renormalization.

The effect of the dielectric disorder can be seen in Fig. 2.6.c). This figure shows the result obtained by [77] et al. They performed Photoluminescence mapping of a WS_2 monolayer flake, placed on two different substrates: a fused silica substrate and a sapphire one. It is evident how in the fused silica substrate, the excitonic response is more homogeneous than in the case of the sapphire, where the local variation

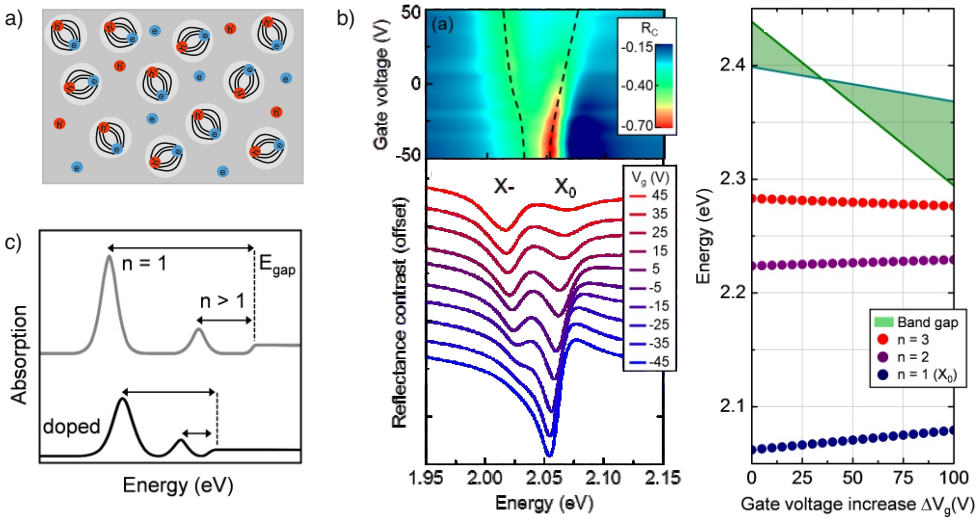

FIGURE 2.7: a) Sketch of photoexcited excitons and QFC in 2D semiconductors. b) Sketch of effect of bandgap renormalization and binding energy reduction on excitonic resonance. c) Gate dependent Reflectance contrast of a monolayer WS_2. Fig. taken from [26].

of the dielectric screening leads to different excitonic absolute energies in different areas on the sample.

Summarizing, we showed how the dielectric environment, through static screening, plays a fundamental role in determining the energetic structure of TMDC monolayers. We also evidenced the influence of dielectric disorder at the microscopic scale and its contribution to the macroscopic excitonic response. Another critical aspect to consider now is the dynamic screening of the exciton due to the presence of quasiparticles in the system.

2.2.2 Quasi-particle induced screening

In the previous section, we saw how the static screening from the environment influences the excitonic resonance in TMDC through screening of the Coulomb interaction leading to binding energy reduction and quasi-free particle bandgap renormalization. Another mechanism of screening of Coulomb interaction can originate from the presence of carriers or quasiparticles in the system. In fact, the presence of quasiparticles in the system, through dynamic screening, can alter the exciton properties of the TMDC.

This subsection aims exactly to introduce the effect of the dynamic screening originating from the presence of these quasiparticles on the excitonic response of

monolayer TMDCs. In particular, we will discuss the effects on the excitonic resonance originating from the static presence of carriers through the analysis of experiments performed by applying a gate voltage to the sample. I then move forward to discuss the mechanism through which the quasiparticle dynamic screening affects the Binding energy reduction and Quasi-free particle bandgap renormalization.

To start, Let us take an ideal semiconductor. Free carriers or quasiparticles can be injected into the system, either through a gate voltage or through photoexcitation. The free carriers are free to move in the semiconductor and can rearrange spatially to dynamically screen the exciton field lines, therefore inducing a reduction of binding energy and quasi-free particle bandgap renormalization. Furthermore, through optical excitation, it is possible to photoexcite excitons which, if they are close enough to each other, can screen themself, ultimately leading to the energy structure renormalization.

The main question of this section is which influence do excitons and quasi-free carriers have on the excitonic properties of a material. The question can be visualized in the sketch in Fig. 2.7.a). When quasiparticles are present in the system, and their average distance is in the same order of magnitude as the size of the exciton, the interparticle interaction can not be neglected. Let us consider a test exciton for instance, when other excitons are present in the close vicinity, they act as a dipole, screening the Coulomb interaction between the electron and the hole of the test exciton. Furthermore, quasi-free carriers can rearrange spatially and screen one or the other carriers. As we saw in the previous sections, this leads to a reduction of Quasi-free particle bandgap and binding energy reduction.

The easiest way to force carriers in a material is to apply a gate voltage to it. By gating a sample is then possible to control its electrical doping. This process forces a certain density of carriers into the system and induces charging. In their work [26] Chernikov et al. measure the reflectance contrast signal of a monolayer WS_2 as a function of photon energy for various gate voltages applied to it. This measurements are visible in Fig. 2.7.b). Upon increasing the gate voltage, they increase the electron density in the material, observing that the neutral exciton resonance undergoes a blueshift. In particular, for electrons doping, the neutral exciton shift can be interpolated with a linear function returning a linearity coefficient of 2.15 10^{-12} meV cm^2. Such shift is attributed to dynamic screening originating from the presence of free electrons in the system. The reduced Coulomb interaction strength induces quasi-free particle bandgap renormalization and binding energy reduction as sketched in 2.7.c). By taking the limit of the excitonic rydberg-like excited states series, Chernikov et al. determine the energy of the quasi-free particle bandgap as a function of gating voltage. From the right panel in 2.7.b), it is evident how the bandgap renormalization is higher in terms of absolute energy changes, with respect to the absolute exciton energy peak shift.

It is important to mention now that another way to bring quasiparticles into the system is by photoexcitation. Upon optical pumping, either quasi-free carriers or

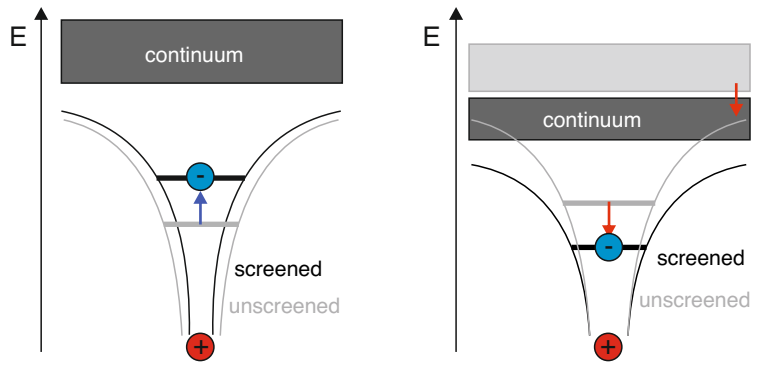

FIGURE 2.8: Sketches of exciton binding energy reduction (left) and bangap renormalization (right) due to screening.

exciton can be injected into the system. The particularity, in this case, is that charge neutrality is maintained. The drawback is that carriers are only transiently present in the system since they undergo dynamics and recombination that bring the system back to equilibrium. This means that time-resolved spectroscopy becomes a necessary tool to investigate the dynamic screening due to the presence of quasiparticles. With this technique, an intense optical pulse can generate a finite quasiparticle density and a delayed weak probe pulse can track the optical signature of the exciton.

Analogously to the case of electrical doping, quasiparticles presnet in the system, screen the Coulomb interaction, modifiing exciton binding energy and Quasi-free particle bandgap. The details of the competing effects of binding energy reduction (BER) and bangap renormalization (BGR) can be explained with the following.

To explain the BER we can turn to the comparison of the Rydberg bound states [81]. Fig. 2.8 shows the electronic bound state of en electron in presence of the Coulomb potential of a positive charge. The energy of the ground state of the system (depicted) and the excited states (not depicted, but analogous to the inset of Fig. 2.4.a)) is determined by the Coulomb potential. If now the screening is enhanced, for instance from the presence of quasiparticles, the Coulomb potential is modified, specifically it is narrowed, as shown in the same figure. The narrowing of the Coulomb potential leads to a blue-shift of the ground state towards higher energies. This effect is due to simple dielectric screening of the attractive Coulomb force and can thus be originating both by the presence of QFC or excitons in the system. In the first case QFC will re-dispose themselves in the vicinity of the constituent carriers of the exciton, screening their interaction. In the case of excitons transiently present in the system, instead, they act as dipoles reorienting to minimize the energy of the system.

In the case of the BGR the mechanism is more involved due to it being a multi-particle effect. In a simplistic picture. When a QFC density is present in the system,

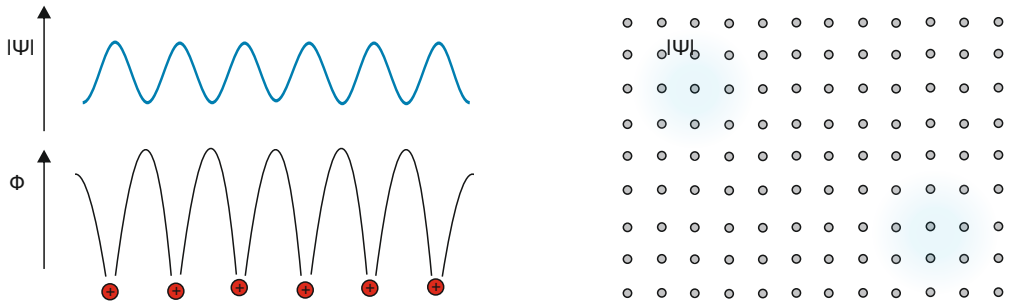

FIGURE 2.9: left) sketch of QFC wavefunction on a lattice potential. Charge carriers are delocalized. Right) rappresentation of the wavefunction of an excitons in a periodic lattice.

occupying the conduction band states, the excitation of an electron to the conduction band is less favorable due to electron-electron repulsive interaction. Such effect is particularly prominent in low dimensional semiconductor due to the reduced screening inherent to their nature [82] with respect to the 3D counterparts [83]. The BGR can be calculated by analyzing the screening contribution to the self-energy, requiring calculation of the band structure with GW approximation. This approach estimates the corrections to the quasi-free bangap that occurs in two dimensional system with reduced screening [83, 84], and TMDC in particular [85, 86]. Now, when QFC are present in the system, they screen the Coulomb repulsive interaction, thus leading to a lower contribution to the self-energy, inducing a reduction of the bandgap for enhanced screening. This is schematized also in Fig. 2.8 where the effect of the bandgap renormalization is a redshift of the continuum of states towards lower energies. The competition of this two effect can turn to either a blue or red-shift according to the relative ratio of the BER and BGR [87].

Excitons can also screen the Coulomb interaction therefore leading to band structure renormalization. The changes of the exciton resonance are also in this case due to the competition of exciton BER and BGR. In the case of the BER, this is easilly explained with dielectric screening of the attractive Coulomb interaction, analogously to the case reported in Fig. 2.8.a). Regarding the BGR this is more complicated. It was shown that exciton screening has an impact on the quasi-free particle bandgap [88] through the same mechanism of the QFC. This mechanism is the screening of the repulsive Coulomb interaction and therefore changes in the self-energy.

When analyzing the problem from a microscopical point of view, the changes to the self-energy depends on the polarizability of QFC or excitons. QFC are delocalized particles, meaning that are highly polarizable. Due to this a wavefunction of QFC can change the ionic potential landscape periodically [89], as shown in Fig. 2.9. Instead, excitons are localized quasiparticles, with a spatial extension in the order of the few nm in TMDC [6, 61], and are charge neutral. This means that excitons, by

being localized , as shown in Fig 2.9, are not as easilly polarizable with respect to the QFC. Therefore, their screening of the Coulomb interaction, assuming the same density of quasiparticle, with respect to the QFC equivalent, will be lower. This suggest a less efficient screening of the Coulomb interaction when excitons are present in the system, therefore a smaller BGR originating from the presence of excitons. Nevertheless the exciton contribution to the BGR is non negligible as already discussed, especially when excitons are prevalently present in the system [90, 30, 88, 83]. If we consider excitons as a dipole which is free to move around the lattice, they can rearrange spatially and screen a charge carrier. If we now want to photoexcite another quasi-free carrier in the system, the effective Coulomb repulsion strength from the already present carrier will be lower, meaning a lower contribution to the self-energy, thus smaller quasi-free particle bandgap. The different screening originating from the presence of excitons and QFC is still needed to be comprehensively understood. This is also one of the central question that this thesis aims to solve.

Before tackling this question, though, it is necessary to introduce the basics of light-matter interaction needed to derive a formalism that allows the extraction of quantitative information about the excitons and the basics of the pump and probe technique. The discussion about the dynamic screening will then be revisited in Chapter 5.

2.3 Summary and outlook

The purpose of this chapter was to introduce the fundamental physical and optical properties of the TMDC monolayer materials in order to establish a base ground upon which this thesis will build on. Firstly the main essence of the novel physical properties of TMDC, when they get thinned down to a monolayer, were introduced, unravelling a direct semiconductor with bandgap at the K-valley. Furthermore, the exciton, arising from the quantum confinement and reduced screening, specific to the 2D nature of these materials, were introduced and their main properties discussed.

Particular focus was then given to the optical properties of the TMDC, showing how excitons appear in the optical spectra, and to the optical selection rules that allow to distinguish between dark and bright excitons. Lastly, the main influence of external factors such as temperature or dielectric screening was shown. Particular attention was given to the screening with a dedicated section. The influence of the static screening and its fundamental impact on the energetic structure of the monolayers TMDC were discussed, showing that the exciton can shift and broaden simply by changing the effective screening of the surrounding ad through local dielectric disorder. Finally, also the dynamic screening originating from the presence of quasiparticles in the system was introduced as a mechanism to change the excitonic and energetic structure of these materials.

From this point, recalling the main question of this thesis that was introduced in the introduction chapter, we need to develop a formalism to investigate quantitatively and being able to compare between the different optical experiments and unravel the role of the different quasiparticles in the exciton response upon photoexcitation. It becomes necessary to introduce the theoretical fundaments of light-matter interaction that are necessary to investigate optically TMDC materials.

Chapter 3

Theory

The previous chapter reviewed the fundamental physical properties of monolayers TMDC, particularly focusing on the strong excitonic optical response originating from the reduced screening and quantum confinement inherent to the specific nature of these materials. We discussed the exciton optical properties and its optical signature in optical spectra. Now, it is already clear from the previous chapter that the resonance in the optical spectra provides information about the exciton properties. Thus, a proper formalism is necessary to extract any quantitative information from optical experiments. To provide such formalism, we now turn to the fundamentals of light-matter interaction.

The understanding of light-matter interaction led to the development of many tools that are fundamental for physics and even for tools used in everyday life. Let's take, for example, lasers or fiber optics, which allowed the development of the whole photonics or optoelectronics fields. From a more fundamental point of view, the correct interpretation of how light interacts with matter is crucial for the theoretical understanding of the results of optical experiments. In fact, given a general sample made of a particular material and with a certain geometry, it is not clear a priori how this interacts with the light incident upon it. Nevertheless, this interaction can be formalized, as we will see in this chapter, which aims to provide the basic theoretical background to investigate a material, and more specifically 2D materials, steady-state and dynamical optical response to electromagnetic radiation.

This chapter will start from the most general formulation of the problem of light-matter interaction in section 3.1. The fundamental optical constant describing the material optical properties are derived. Furthermore, the Lorentz model describing the frequency-dependent polarization and dielectric function for bound carriers in solids is reported. Section 3.2 deals with the geometrical aspect of the light-matter interaction, particularly important when dealing with two dimensional materials and the complex interference phenomena arising at the multiple interfaces characteristic of thin films and heterostructures. By employing a Fresnell formalism[91, 92] we derive the characteristic matrix of a stack of thin layers, retrieving its optical response. The derivation of the 2D linearized model [93], used to retrieve optical spectra in the case of a thin layer on a thick substrate for normal incidence, is also shown. Finally, section 3.3 moves on from the calculation of optical spectra at equilibrium and gives

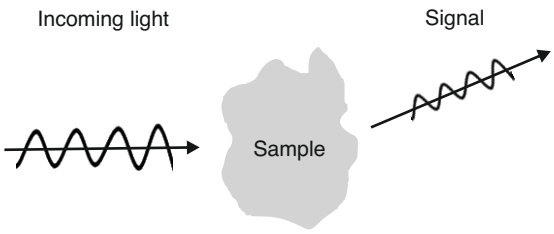

FIGURE 3.1: Sketch of signal originating from the light interacting with a sample

the theoretical background necessary to describe the time-dependent evolution of a system when it is subject to a perturbation. This is done by introducing the Einstein rate equation model and the optical Bloch equations, ultimately demonstrating that the two are equivalent when the coherences in the system are negligible.

This whole chapter develops on the most basic problem of light-matter interaction as a guideline. The main question that we try to answer is how the light gets modified by the interaction with a sample. New degrees of complexity are added in every section, but the fundamental problem is described in the following section, and the results are summarized in the last section 3.4.

Ultimately this appendix summarizes an accurate method to determine the absorbed photon density, thus the initial photoexcited quasiparticle density, for resonant and above-resonance pumping of a monolayer WS_2 placed on various substrates.

3.1 Light matter interaction

As we discussed in the introduction of this chapter, when a sample interacts with some sort of electromagnetic radiation, it is not clear a priori how the light is modified after the interaction. It is therefore necessary to formalize this interaction, as described in the following.

This section aims to provide the theoretical background to investigate quantitatively the optical response of a material. We first pose the problem of an electromagnetic wave interacting with a sample. We then introduce the quantities describing the material specific optical properties of the sample. We then derive these optical constants from consideration about bound carriers in a solid, namely the Lorentz model.

The most general problem is given by a generic sample to be investigated, without any assumption about it, as sketched in Fig. 3.1. Firstly, we can shine some sort of electromagnetic wave that interacts with the sample. The light that has interacted with the sample, the signal, will then have different properties. The specific way in which these properties of the light change provides us with information about the basic physical properties of the sample under investigation. In order to make this rigorous, we need a formalism that allows to unravel specific characteristics or

properties of the sample based on the signal that is acquired, or, in other words, formalizing how the light is modified after interacting with the sample.

To do that, let's consider the simple case of a monochromatic wave impinging on an arbitrary sample as already reported in Fig. 3.1. We can describe the incoming wave according to the following formula:

$$\mathbf{E} = \mathbf{E}_0 e^{-i(\omega t - \mathbf{kr})} \tag{3.1}$$

This equation describes a wave with the polarization given by the direction of $\mathbf{E_0}$, an amplitude (E_0) and direction of propagation $\mathbf{k}$.

In principle, any of these properties can change after interaction with the sample. The sample material and sample geometry are the main causes of modification of the light properties, and this means that, if we are interested only in the material specific properties, these must be isolated from the geometrical influences. In some cases, such as 2D materials like TMDCs, the material and geometrical specific properties are mixed in the signal that is detected in an experiment, requiring an adapt formalism to disentangle the two.

With the given premises, we discuss firstly the main optical properties and quantities that define a material macroscopic optical response. After, we will see how we can model the refractive index and dielectric function of a material from consideration about the microscopic bound carriers, thus introducing the Lorentz model.

Firstly we need to define the complex dielectric function and the complex refractive index, as introduced in the following. The following part is based on references [92, 91].

3.1.1 Linear optical properties

In this subsection, we discuss the mathematical derivation of the fundamental quantities that defines a material optical response. We saw how these are fundamental in order to understand and model optical signals.

Particularly, in the following subsection, we will deal with the mathematical derivation of the complex dielectric function and the refractive index of a material, ultimately showing how the optical response of a sample can be calculated in a forward search fashion starting from the previously derived quantities.

We use a semi-classical treatment, starting from Maxwell's equation for isotropic and non magnetic media. From this, it is straightforward to derive the relation between electric field and electric displacement as follow:

$$curlcurl\mathbf{E} = graddiv\mathbf{E} - \Delta\mathbf{E} = -\frac{\partial^2 \mathbf{D}}{\partial t^2} \tag{3.2}$$

This equation is called the wave equation, and it relates the electric field $\mathbf{E}$ and $\mathbf{D}$ the electric displacement field. It becomes necessary to relate these two quantities to be able to solve this equation. To do this, we can assume that, when an electromagnetic field interacts with matter, it induces a displacement of both negative and

positive charges, thereby generating a net polarization, thus a macroscopic dipole moment of the system. Due to the causality principle and neglecting the space dependence of the electric field and of the dipole moment per unit volume, we postulate that the polarization depends on the electric field at the precise time as well as the previous ones, as follows:

$$\mathbf{P}(t) = \varepsilon_0 \int_{-\infty}^{t} \kappa(t, t')\mathbf{E}(t')dt' \tag{3.3}$$

Where $\kappa(t, t')$ is generally a tensor. We restrict the derivation to isotropic materials, where the vector $\mathbf{P}$ is always parallel to $\mathbf{E}$, making κ a scalar function. Furthermore, due to homogeneity of time, Eq. 3.3 can be rewritten as a function of the time difference of $\xi = t - t'$ as:

$$\mathbf{P}(t) = \varepsilon_0 \int_{0}^{\infty} \kappa(\xi)\mathbf{E}(t - \xi)d\xi' \tag{3.4}$$

Supposing harmonic field we can rewrite Eq. 3.4 as:

$$\mathbf{P}(t) = \mathbf{E}(t)\varepsilon_0 \int_{0}^{\infty} \kappa(\xi)e^{i\omega\xi}d\xi' \tag{3.5}$$

Here we define the linear dielectric susceptibility χ as follows:

$$\chi(\omega) = \int_{0}^{\infty} \kappa(\xi)e^{i\omega\xi}d\xi' \tag{3.6}$$

χ is a complex quantity depending on the frequency, and it carries information about the specific optical properties of the material. We can now define a relationship between electric field and electric displacement from Eq. 3.5 and Eq. 3.6:

$$\mathbf{P} = \varepsilon_0\chi\mathbf{E} \tag{3.7}$$

$$\mathbf{D} = \varepsilon_0\mathbf{E} + \mathbf{P} = \varepsilon_0[1 + \chi(\omega)]\mathbf{E} = \varepsilon_0\varepsilon(\omega)\mathbf{E} \tag{3.8}$$

In the last equality, we defined the dielectric function $\varepsilon(\omega)$, which is the key quantity that we will talk about in this thesis. Such quantity defines the optical properties of a material and depends on the frequency. It is the analogous of the dielectric constant in electrostatic since it relates the electric field and the electric displacement vectors. From this quantity, it is possible to calculate the optical properties of a material, as we will see in the following.

Using Eq. 3.8 in Eq. 3.2 for harmonic oscillation of the field and for isotropic materials we obtain the scalar relationship:

$$\Delta E + \frac{\omega^2\varepsilon(\omega)}{c^2}E = 0 \tag{3.9}$$

From Eq. 3.9, in the approximation of homogeneous media and light propagating along the z-axis, we obtain a solution in the form of:

$$E = E_0 e^{-i\left(\omega t - \frac{\omega}{c}\sqrt{\varepsilon(\omega)}z\right)} \tag{3.10}$$

Where the term $k = \frac{\omega}{c}\sqrt{\varepsilon(\omega)}$ is the wavevector. Eq. 3.10 describes a damped wave, in fact it can be rewritten, by expressing the complex dielectric function in its real and imaginary part, as:

$$E = E_0 e^{-\frac{\omega}{c} Im\sqrt{\varepsilon(\omega)}z} e^{-i\left(\omega t - \frac{\omega}{c} Re\sqrt{\varepsilon(\omega)}z\right)} \tag{3.11}$$

where the first part correspond to a z-dependent amplitude and the argument of the second exponential is a phase. If we calculate the phase velocity by differentiating the phase as a function of time, we obtain:

$$\frac{z}{t} = v_{phase} = \frac{c}{Re\sqrt{\varepsilon(\omega)}} = \frac{c}{n(\omega)} \tag{3.12}$$

Where we defined the refractive index $n(\omega)$. The last equation means that the phase velocity of an electromagnetic wave in a material is given by the dispersion relation through the frequency-dependent refractive index. More in general the refractive index is defined as a complex quantity $\hat{n}(\omega)$:

$$\hat{n}(\omega) = n(\omega) + iK(\omega) = \sqrt{\varepsilon(\omega)} \tag{3.13}$$

The pair of quantities n and K constituting the complex refractive index are then called linear optical constant of a material and determine its optical response. The real part of the complex refractive index determines the dispersion of the light in a medium and the imaginary part accounts for the damping of a wave in a material through the so-called extinction coefficient $K(\omega)$.

In fact, from Eq. 3.11 we can calculate the intensity of the wave propagating in a lossy material, which is proportional to the square of the electric field, as follow:

$$I = I(z=0)e^{-2\frac{\omega}{c}Kz} = I(z=0)e^{-\alpha z} \tag{3.14}$$

The Eq. 3.14 is known as the Lambert law, in which we defined the absorbtion coefficient as:

$$\alpha = -2\frac{\omega}{c}K(\omega) = 4\pi\nu K(\nu) \tag{3.15}$$

The absorption coefficient determines the damping in the amplitude of a wave propagating through a lossy media.

In summary, we showed how the material specific response is contained in the dielectric constant or the refractive index. With the derivation of the Lambert law, we demonstrate how, by knowing the complex dielectric function, it is possible to calculate the modification to the light after interaction with a sample made of a specific material, in the approximation of isotropic homogeneous media and for normal

incidence. The calculation of the optical properties of a sample is then quite straightforward if the complex dielectric constant is known.

Unfortunately, more in general in optical spectroscopy, we have the opposite problem of retrieving the complex permittivity from the optical response of a sample. This is called reverse search and it is not trivial. In fact, other than solving the wave equation 3.2 for a particular geometry at which an experiment is performed, we need to find a suitable way to retrieve the real and imaginary part of the dielectric function due to the fact that we have two unknowns and one equation. This can be done in three different ways:

- Approximate the dielectric function with an appropriate model that contains all the information of a specific material and then proceed with the inverse search of the dielectric constant.
- Kramers-Kronig relationship, which relates the real and imaginary part of the refractive index, but requires measurements on a wide spectral range
- Angle dependent measurements of optical properties which, by changing the geometry, allow to have another wave equation, and therefore the extraction of n and K.

In the following part, we describe how we can model the dielectric function of bound carriers employing the Lorentz model.

3.1.2 The Lorentz oscillator

In the previous section we saw that when light interacts with matter, it induces a macroscopic polarization in the media, depending on the electric field through the linear susceptibility. This was described by Eq. 3.8, and we evidenced how the linear susceptibility includes all the information regarding the optical response of the material. As introduced in the ending of the previous subsection, it is possible to model the susceptibility of a material, thus the refractive index and the dielectric function.

In this section, we discuss how to model the linear susceptibility in the case of bound carriers in a solid, nominally the Lorentz model, and when it is possible to apply such model to the analysis of optical spectra.

We consider an electromagnetic wave interacting with a charge carrier that is bound to its equilibrium position, analogously to an electron which is free to move in the surrounding of an ion but still being attracted to it. This can be modelled, in a classical mechanical picture, with the second newton's law for a forced and damped harmonic oscillator with eigenfrequency ω_0 as:

$$m\frac{d^2x}{dt^2} + m\gamma\frac{dx}{dt} + m\omega_0^2 x = -qE \tag{3.16}$$

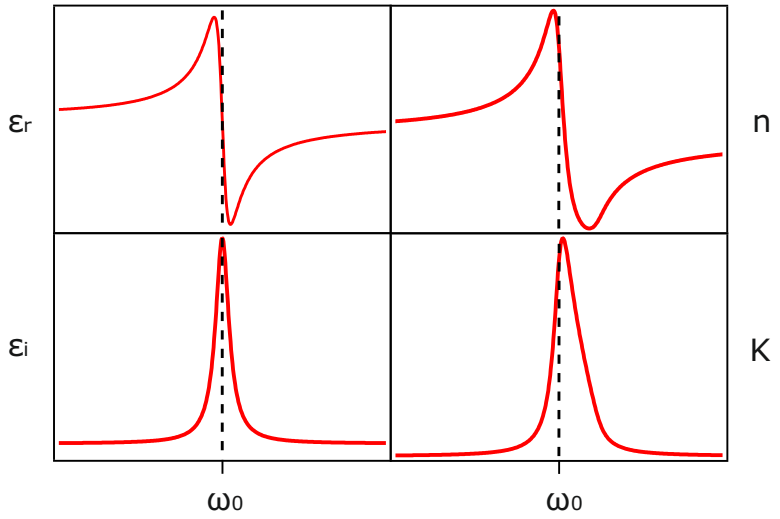

FIGURE 3.2: Frequency dependent real and imaginary part of complex dielectric function and refractive index

Here q and m are the charge and the mass of an electron, but it could also be an effective mass, depending on the system in analysis. γ is a damping parameter accounting for the damping of the electron motion. This is due for instance to scattering of the electron.

We assume: low intensity of the driving force (low intensity of the electromagnetic wave), E as an harmonic field, and oscillation of the electric field along the x axis. Assuming also that the solution of Eq. 3.16 are in the form $x(t) = x_0 e^{-i\omega t}$, we rewrite, from Eq. 3.16:

$$\frac{-qE}{m} = -\omega^2 x - 2i\omega\gamma x + \omega_0^2 x \tag{3.17}$$

We now consider that the oscillation of the electron around its equilibrium position induces a dipole moment. Assuming N number of electrons per unit volume, the total polarization is given by:

$$P = Np = \frac{-q^2 EN}{m} \frac{1}{\omega_0^2 - \omega^2 - 2i\omega\gamma} \tag{3.18}$$

Now, comparing this equation to Eq. 3.7, allows us to derive the expression of the complex linear susceptibility:

$$\chi = \frac{-q^2 N}{\varepsilon_0 m} \frac{1}{\omega_0^2 - \omega^2 - 2i\omega\gamma} \tag{3.19}$$

Using Equation 3.8 we can then retrieve the complex dielectric function given by:

$$\varepsilon(\omega) = 1 + \frac{-q^2 N}{\varepsilon_0 m} \frac{1}{\omega_0^2 - \omega^2 - 2i\omega\gamma} \tag{3.20}$$

The last equation is an analytical expression for the dielectric function derived only

from consideration about the microscopic bound carriers. Therefore, such relation defines the macroscopic properties of a material from the assumption made on the microscopic quantities.

We can now calculate the refractive index using Eq. 3.13. The real ε_r and imaginary part ε_i of the complex dielectric function and of the refractive index n and K are reported, for an arbitrary value of γ, in Fig. 3.2 as a function of the frequency. It is clear from the graphs that the imaginary part of the complex dielectric function corresponds to a symmetric Lorentzian profile. This is not necessarily the case for the extinction coefficient K, where an asymmetry is clearly evident, and it must be taken into account when analyzing optical spectra. Nevertheless, the absorption of the material is maximum in the proximity of ω_0. For frequencies far from ω_0 the absorption is almost negligible, but for the real part of the complex refractive index can change significantly, therefore changing the phase that the light acquires while passing through the medium and its dispersion.

Summarizing, in this section we performed the derivation of the Lorentz model for bound carriers in a solid that allows to derive analytically the dielectric constant. The validity of the Lorentz model is quite broad since it can be used to model bound electrons as well as intramolecular motion of cores [91]. In optical spectroscopy, the Lorentz model can approximate well isolated spectral lines and, more in general, isotropic media with strongly bound electrons.

We now have introduced the fundamental material specific optical properties. Starting from the dielectric function, we demonstrated how to calculate the optical spectra in the simple case of homogeneous media and normal incidence, and how the inverse procedure can be used for the inverse search of the dielectric function that best approximates the observed spectra. Before proceeding forward, it is necessary to spend some time regarding the influence of the sample geometry. In fact, the derivation of the optical properties for the case of thin films is not straightforward as we saw in this section and is discussed in the next section.

3.2 Fresnell optics

In section 3.1.1, we derived a framework to calculate optical spectra in the case of isotropic and homogeneous media. General, more realistic boundary conditions for solving the Maxwell equation for the experimental or sample geometry needs to be taken into account. Especially when dealing two dimensional material, these are often deposited on substrates, and the effects arising from the multiple interfaces between the layers must be taken into account. Recalling the problem shown in Fig. 3.1 of the light-matter interaction with a generic sample, we now deal with a specific layered geometry of the sample and incoming light, as sketched in Fig. 3.3.

The task is now to calculate the reflected and transmitted fraction of a layered sample of the impinging electromagnetic wave. This can be done by using Fresnel optics, which basically consists in solving the Maxwell equation for a specific set of

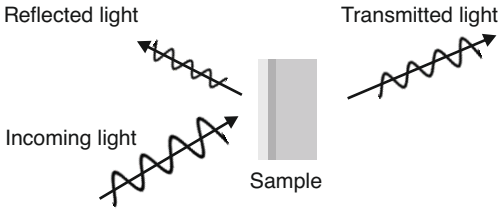

FIGURE 3.3: Sketch of Fresnel optical problem of retrieving reflected and transmitted fraction of light from a stack of thin films

geometrical boundary conditions, assuming that the dielectric constant of the constituent material is known.

In the following, we report the mathematical derivation of the optical observable for a thin layer placed on a substrate which can be either a simple thick glass substrate or a complex layered structure, by using either the 2D linearized model [93] or a characteristic matrix approach, respectively. Unintuitively, we start from the most complex case of a stack of layers and an arbitrary incidence of the incoming light, and then we describe the case of a thin layer on a thick substrate with normal incidence of the incoming electromagnetic wave. This because the second case can be derived as a subcase of the first one, and it is more convenient for the sake of the flow of this work. The mathematical derivation in the following is quite involved and it is based on the references [92, 91, 93].

3.2.1 Optical properties of a stack of thin layers: the characteristic matrix approach

As already mentioned in the previous sections, when an electromagnetic wave propagates through a lossy material, the wave can be absorbed and/or dispersed. When light interacts with one or multiple thin layers, with a thickness similar to the wavelength of the light, multiple interference effects may arise at the interfaces between the constituent layers. These interferences can alter the optical response of a material substantially and need to be taken into account when calculating or modeling the optical observables of an experiment.

To include the aforementioned effects, we can employ the Fresnell equations to model the boundary condition at every interface, and introduce a formalism that allows the calculation of the optical properties of a stack of layers as given in the following. The formulation of the problem is the following.

Let us suppose an electromagnetic beam E_{iI} impinging on a thin film, on top of a semi-infinite substrate, as depicted in Fig. 3.4. We assume that we are dealing only with harmonic electric and magnetic fields. Each wave E_{rI}, E'_{rII}, E_{tII}, represents the resultant of all waves travelling at that point in the medium in that direction. The boundary condition at the multiple interfaces requires the perpendicular components of both electric and magnetic fields to be continuous. This results at the first

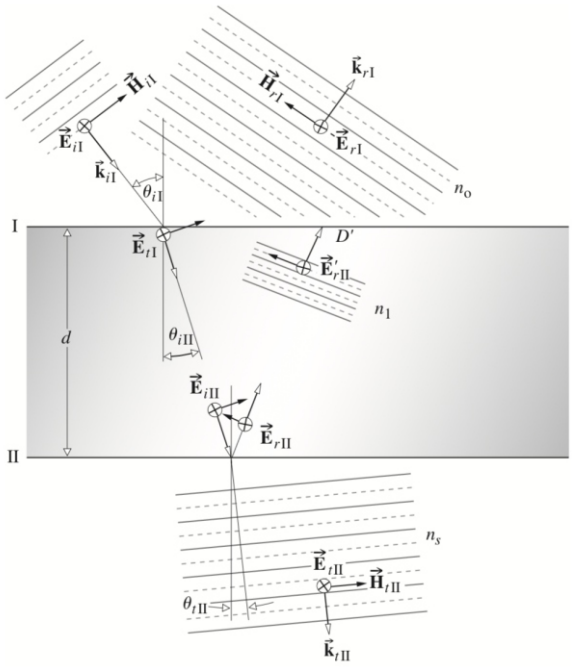

FIGURE 3.4: Sketch of propagation of light through a thin layer in between two semi infinite media. Figure taken from [92]

interface as:

$$E_I = E_{iI} + E_{rI} = E_{tI} + E'_{rII} \tag{3.21}$$

Considering that in non magnetic materials the electric and magnetic field are related through:

$$\overrightarrow{H} = \sqrt{\frac{\varepsilon_0}{\mu_0}} n\hat{k} \times \overrightarrow{E} \tag{3.22}$$

It follows from Eq. 3.21 that:

$$H_I = \sqrt{\frac{\varepsilon_0}{\mu_0}} \left(E_{iI} - E_{rI}\right) n_0 cos\theta_{iI} \tag{3.23}$$

$$H_I = \sqrt{\frac{\varepsilon_0}{\mu_0}} \left(E_{tI} - E_{rII}\right) n_1 cos\theta_{iII} \tag{3.24}$$

Analogously for the second interface it results

$$E_I I = E_{iII} + E_{rII} = E_{tII} \tag{3.25}$$

$$H_{II} = \sqrt{\frac{\varepsilon_0}{\mu_0}} \left(E_{iII} - E_{rII}\right) n_1 cos\theta_{iII} \tag{3.26}$$

$$H_{II} = \sqrt{\frac{\varepsilon_0}{\mu_0}} E_{tII} n_s cos\theta_{tII} \tag{3.27}$$

These sets of equations represent the boundary conditions of the problems. When we express the harmonic fields, we can rewrite Eq. 3.25 and Eq. 3.26 as:

$$E_I I = E_{tI} \exp -ik_0 h + E'_{rII} \exp +ik_0 h \tag{3.28}$$

$$H_I = (E_{tI} \exp -ik_0 h - E_{rII} \exp +ik_0 h) \sqrt{\frac{\varepsilon_0}{\mu_0}} n_1 cos\theta_{iII} \tag{3.29}$$

In the last two equations, h is given by $nzcos\theta_{iII}$ and take into account the shift in phase that a beam that traverse a dispersive layer undergoes to.

These last two equation can be solved for E'_{rII} and E_{tI} and substituted in Eq. 3.21 and Eq. 3.22. The resulting linear relations can be written in matrix notation as:

$$\begin{pmatrix} E_I \\ H_I \end{pmatrix} = \begin{pmatrix} \cos(k_0 \hat{n} z \cos\theta) & -\frac{i}{\hat{n}\cos\theta} \sin(k_0 \hat{n} z \cos\theta) \\ -i\hat{n}\cos\theta \sin(k_0 \hat{n} z \cos\theta) & \cos(k_0 \hat{n} z \cos\theta) \end{pmatrix} \begin{pmatrix} E_{II} \\ H_{II} \end{pmatrix} \tag{3.30}$$

Here the matrix, that we define $\mathbf{M_I}$, correspond to the characteristic matrix of the film and, itself, describes the propagation of a light beam through it.

Let's now suppose to have a different geometry with respect to Fig. 3.4 in which two thin layers are present and not only one. In this case there will be three boundaries conditions, resulting in:

$$\begin{pmatrix} E_{II} \\ H_{II} \end{pmatrix} = \mathbf{M_{II}} \begin{pmatrix} E_{III} \\ H_{III} \end{pmatrix} \tag{3.31}$$

It is easily seen now that if we multiply both sides of the last Eq. 3.31 by $\mathbf{M_I}$ we obtain:

$$\begin{pmatrix} E_I \\ H_I \end{pmatrix} = \mathbf{M_I M_{II}} \begin{pmatrix} E_{III} \\ H_{III} \end{pmatrix} \tag{3.32}$$

This means that the characteristic matrix of a stack is given by the multiplication of the characteristic matrices of the constituting layers So extending to an arbitrary number j of layers, we finally obtain the general expression:

$$\begin{pmatrix} E_I \\ H_I \end{pmatrix} = \hat{\mathbf{M}}_{stack} \begin{pmatrix} E_{j+1} \\ H_{j+1} \end{pmatrix} = \prod_j \hat{\mathbf{M}}_j(d_j,) \begin{pmatrix} E_{j+1} \\ H_{j+1} \end{pmatrix} \tag{3.33}$$

To calculate the reflection and transmission amplitude of a light beam propagating from the stack of layers, we can rewrite Eq. 3.30 by making use of the boundary conditions as follows:

$$\begin{pmatrix} E_{iI} + E_{rI} \\ (E_{iI} + E_{rI}) \sqrt{\frac{\varepsilon_0}{\mu_0}} n_0 cos\theta_{iI} \end{pmatrix} = \mathbf{M_I} \begin{pmatrix} E_{tII} \\ E_{tII} \sqrt{\frac{\varepsilon_0}{\mu_0}} n_s cos\theta_{tII} \end{pmatrix} \tag{3.34}$$

From here by expressing Eq. 3.34 in its linear form and by defining $r = E_{rI}/E_{iI}$ and $t = E_{tII}/E_{iI}$ we can derive the expression for the reflection and transmission

amplitude according to the following formulas:

$$R = |r|^2 = \left| \frac{(m_{11} + m_{12}\hat{n}_{sub}\cos\theta_{tII})\cos\theta_{tiI} - (m_{21} + m_{22}\hat{n}_{sub}\cos\theta_{tII})}{(m_{11} + m_{12}\hat{n}_{sub}\cos\theta_{tII})\cos\theta_{iI} + m_{21} + m_{22}\hat{n}_{sub}\cos\theta_{tII}} \right|^2 \tag{3.35}$$

$$T = n_{sub}|t|^2 = n_{sub} \left| \frac{2\cos\theta_{iI}}{(m_{11} + m_{12}\hat{n}_{sub}\cos\theta_{tII})\cos\theta_{iI} + m_{21} + m_{22}\hat{n}_{sub}\cos\theta_{tII}} \right|^2 \tag{3.36}$$

This treatment is valid for a general stack of layers with isotropic materials and for any arbitrary incidence angle. In fact, the complexity of the multilayer structure is all contained in the matrix elements. The case of anisotropic materials would imply a tensor instead of a matrix. This is a more general case that can be found in [94]. We now can calculate the reflected and transmitted fraction of a complex layered heterostructure given the dielectric function of its constituent layer and their thickness, and for an arbitrary incidence angle.

Concluding, the derivation of the reflected and transmitted fraction of a stack of thin layers in the most general approach was reported. The mathematics involved in such calculation is quite involved, and for some particular cases it can be simplified, as shown in the following subsection.

3.2.2 2D linearized model

The characteristic matrix approach is a complex formulation of the problem of calculating the reflected and transmitted fraction of a stack of layers. In some specific cases, it is useful to simplify such problem in order to obtain much slimmer functions that still describe the optical response of thin layers accurately, especially in the case of TMDC. In order to model the optical properties of monolayer TMDCs few different models were used extensively in literature, corresponding to 3D model of the thin layer, as shown in the previous section for instance, or 2D sheet models. The difference between them is in the treatment of the thin layer, which is considered finite in the first case, and infinitesimally thin in the second case. The use of different models was compared by Li et al. in [93]. Furthermore, in their work they derive a 2D sheet model (called 2D linearized model) for the thin film in which the optical response of a monolayer TMDC on a transparent substrate is described by the sheet optical conductivity of the TMDC. With this model, it is possible to calculate the observables of reflectance and transmittance contrast spectra as a function of the dielectric function of the sample's constituting materials.

In this subsection, we report the derivation of the 2D linearized model and show how the transmittance contrast of a monolayer TMDC, placed on a thick semi-infinite substrate, can be related to the complex dielectric function of the constituent materials. This treatment starts from the 3D model of a thin film with refractive index n placed on top of a semi-infinite substrate with refractive index n_s. We consider

the case of normal incidence of the incoming beam and that the incoming beam is propagating through air.

In their formulation, Li et. a.l [93] express the reflected fraction of a thin layer of thickness d as follows:

$$R = |r|^2 = \left| \frac{n(1-n_s)cos(k_0 n_1 d) - i(n_s - n^2)\sin(k_0 n_1 d)}{n(1+n_s)cos(k_0 n_1 d) - i(n_s + n^2)\sin(k_0 n_1 d)} e^{-2ik_0 d} \right|^2 \tag{3.37}$$

$$T = Re\,[n_s]\,|t|^2 = Re\,[n_s] \left| \frac{e^{-ik_0 d}}{n_1(1+n_s)cos(k_0 n_1 d) - i(n_s + n^2)\sin(k_0 n_1 d)} \right|^2 \tag{3.38}$$

It is possible to derive equivalent formulas starting from Eq. 3.35 and Eq. 3.36 assuming normal incidence and that the sample is in air. Both cases correspond to different expressions deriving from the formulation of the same problem of a thin film on top of a semi-infinite substrate and are therefore equivalent.

From Eq. 3.37 and Eq. 3.38, it is possible to retrieve the 2D limit by assuming $|k_0 nd| \ll 1$. In this approximation, the expression of the reflection and transmission amplitude becomes independent from the thin layer thickness. Eq. 3.37 and Eq. 3.38 in the limit of small optical phase shift, and also assuming that $|k_0 d| \ll 1$, in which the last approximation is evident from the previous approximation given the fact that n is a number greater than 1, can be linearized, obtain the following coefficients:

$$r = \frac{1 - n_s - Z_0\sigma^s}{1 + n_s + Z_0\sigma^s} \tag{3.39}$$

$$t = \frac{2}{1 + n_s + Z_0\sigma^s} \tag{3.40}$$

In the last two equations, the quantity $Z_0\sigma^s = -i\chi d\omega c$ is a dimensionless quantity describing the sheet response. With these two functions, it is possible to calculate the reflected and transmitted fraction of a beam incident on a thin layer. With respect to Eq. 3.37 and Eq. 3.38, the last two equations are much simpler and still accurate in describing the optical response of 2D material as reported in details in [93].

To even simplify further the problem, an important regime that must be taken into consideration is the regime of weak perturbation of the optical response of the system.

Assuming $Z_0|\sigma^s| = |n^2 - 1|k_0 d \sim |n^2|$ to be small, allows to expand Eq. 3.39 and Eq. 3.40 in linear order in σ^s:

$$r = r_0 \left(1 - \frac{2}{1 + n_s^2} Z_0\sigma^s\right) \tag{3.41}$$

$$t = t_0 \left(1 - \frac{1}{1 + n_s} Z_0\sigma^s\right) \tag{3.42}$$

In Eq. 3.41 and Eq. 3.42, r_0 and t_0 are the reflection and transmission amplitude coefficient in the absence of the thin film. Furthermore, $Z_0\sigma^s$ is given by the following expression:

$$Z_0\sigma^s = (\varepsilon - 1)k_0 d \tag{3.43}$$

From these formulas, we can then derive the expression of the typical observables of optical experiments: reflectance contrast $RC = (R_0 - R)/R_0$ and transmittance contrast $TC = (T_0 - T)/T_0$, where R_0 and T_0 are the transmittance or reflectance of the bare substrate, which are expressed as follows:

$$RC = -Re\left[\frac{4}{n_s^2 - 1} Z_0\sigma^s\right] \tag{3.44}$$

$$TC = -Re\left[\frac{2}{1 + n_s} Z_0\sigma^s\right] \tag{3.45}$$

We now have Eq. 3.44 and Eq. 3.45 which are two expressions that relate the observables of an optical experiment to the complex dielectric function of the sample through the sheet conductivity $Z_0\sigma^s$, which is ultimately related to the complex dielectric function through Eq. 3.43. This 2D linearized model can be employed to model the optical response of thin TMDC layers placed on a thick transparent substrate, with impinging light at normal incidence and approximation of low contrast (TC/RC$\ll$1). This model, despite the many simplifications, is still accurate in describing the optical response of monolayer TMDC, as shown in [93].

Summarizing, this section showed how the complex interplay of material and geometrical properties influences the optical response of a sample. With the Fresnell transfer matrix approach, we have a very capable method to model the reflected and transmitted fraction of light from a stack of layers, and with the 2D linearized model a much slimmer expression for the observable of TC/RC of a thin layer on a thick substrate. With these two models, we have completed the theoretical framework needed to derive the optical properties of a monolayer TMDC, as will be shown in section 6.1.

Ultimately, we solved the problem of calculating the observables of an optical experiments, including the geometrical effects of an arbitrarily complex stack of layers, starting from the dielectric function of the constituents. This solves the problem that was posed at the beginning of this section.

On a more general point of view, the combination of the Fresnel transfer matrix formalism or 2D linearized model with the Lorentz model allows to relate the complex dielectric function of a TMDC material to its reflectance contrast or transmittance contrast. This will be done in the result chapter and particularly in section 6.1. Turning back to the theoretical fundaments of light-matter interaction, we then move forward discussing the time-dependent evolution of a system when it is perturbed optically, described in the next section.

3.3 Light Matter interaction: a time dependent perspective

We saw in the previous sections how to calculate the optical properties of a material starting from the dielectric function. The opposite procedure of that derivation can be used to do reverse search, this meaning to retrieve the complex dielectric function starting from an optical spectra. In the previous sections in this chapter and also in chapter 2, the discussion of the optical properties of TMDC was always made in equilibrium condition, meaning that the state of the system is not varying over time. Generally, when performing time resolved experiments, we are interested in how a system evolves after a perturbation. The terms evolution indicates that the optical properties of the system can change upon photoexcitation. When perturbed, a system can alter its optical response, thus changing its dielectric function. Ultimately, it becomes then necessary to move forward from the steady-state picture and investigate the dynamic response of a system to light.

To do this, there are two possible ways to describe the time evolution of the system, corresponding to the use of rate equations based on Einstein rate equations or a full quantum approach based on optical Bloch equations. The two methods can be considered equivalent when the coherences in the system can be ignored. In this section, the first of the two following subsections discusses the details of the Einstein rate equation model describing the time-dependent interaction of light with a two-level system. The second part introduces the optical Bloch equations, which describes the time evolution of a system, after a perturbation, including the coherences between states. Finally, we derive the Einstein rate equations, from the Optical Bloch equations, in the case of fast dephasing of the coherences, thereby demonstrating the equivalence of the two models under the above mentioned conditions.

3.3.1 Rate equation and pump and probe experiments

When a two-level system interacts with light, it is not clear a priori how the system responds to the incident electromagnetic field. Different physical phenomena can occur, depending on the properties of both light and system themselves. The first and simplest proposed model to describe such interaction was proposed by Einstein when he postulated the existence of stimulated emission [95].

In this subsection, we introduce the Einstein rate equation formalism to model the time-dependent light-matter interaction and discuss its criteria of applicability.

Let's consider a two-energy level system in which we have a ground state and an excited state, separated by an energy E_0. When light perturbs the system, we have to consider three possible phenomena occurring, these corresponding to: absorption, spontaneous emission, and stimulated emission, and all are sketched in Fig. 3.5

When the interacting light frequency is close to the eigenfrequency of the system, the absorption of a photon promoting an electron to the excited state is likely to happen. This process is more likely to occur if the intensity of the light is higher and if the system is in state 1. When the system is in the excited state instead, there

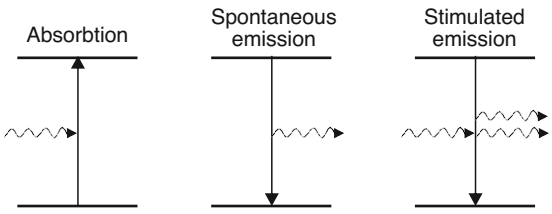

FIGURE 3.5: Sketch of absorbtion, spontaneous emission, and stimulated emission processes in a two energy level system

is the probability of a spontaneous decay to the ground state, this depending on the statistical probability of finding the system in the excited state. Lastly, the system can also do stimulated emission, which is the transition of the system from the excited state to the ground state, with the corresponding emission of a photon activated by the impinging light. This process is proportional to the intensity of the impinging electromagnetic field and to the probability of occupation of the excited state. To express matematically the last considerations, we introduce the Einstein coefficients:

- A_{21} for spontaneous emission
- B_{21} for stimulated emission emission
- B_{12} for absorption

Now supposing N two level system we have that the time evolution of the occupation in the two states is given by:

$$\frac{dN_2}{dt} = N_1 B_{12} u - N_2 B_{21} u - N_2 A_{21} = -\frac{dN_1}{dt} \tag{3.46}$$

Where $u = dE/Vd\omega$ is the so called spectral density of the radiation field, corresponding to the field energy per angular frequency and volume.

From Eq. 3.46 it is clear that when the field is switched off, and we have all the two-level system in the excited state, then the time evolution of the occupation is given by:

$$N_1(t) \propto 1 - e^{-A_{12}t} \tag{3.47}$$

This equation describes the time evolution of the occupation of the ground state and the excited state.

This formalism is rather simple but describes the time evolution of an electronic population when the coherences between states can be ignored. In the case of negligible coherences, the rate equation approach is analogous to the quantum mechanical treatment with optical Bloch equations, as demonstrated in the following subsection.

The assumption of negligible coherences is valid for well separated pump and probe frequencies and/or for lifetimes of the states longer than the typical dephasing time of the coherences. More details are shown in the following section.

3.3.2 Optical Bloch equations

In the previous section, we saw the light-matter interaction formalism based on rate equations introduced by Einstein. Another treatment of the light-matter interaction is using a quantum description provided by the optical Bloch equation. This formalism takes into account the coherence between the different states, as we will see in the following. In the case of fast decoherences between states, the optical Bloch equations reduce to the Einstein rate equations.

This subsection introduces and discusses the optical Bloch Equations. We then proceed to the demonstration of the equivalence of the Bloch equation with the Einstein rate equation model in the approximation of fast decoherence of the system.

Let's suppose a quantum mechanical two level system in which we have two states, a ground state ψ_g and an excited state ψ_e. The system state is then described by the wavefunction:

$$\psi = c_e\psi_e + c_b\psi_b \tag{3.48}$$

with the condition

$$|c_e|^2 + |c_b|^2 = 1 \tag{3.49}$$

This can be rewritten in a matrix form:

$$\rho = \begin{pmatrix} \rho_{ee} & \rho_{eg} \\ \rho_{ge} & \rho_{gg} \end{pmatrix} = \begin{pmatrix} c_e c_e^* & c_e c_g^* \\ c_e^* c_g & c_g c_g^* \end{pmatrix} \tag{3.50}$$

Here we define the density matrix ρ, which specifies the quantum state of a system without being limited only to pure states (diagonal terms) but including also mixed states (off-diagonal terms).

$$\rho = \begin{pmatrix} \rho_{ee} & \rho_{eg} \\ \rho_{ge} & \rho_{gg} \end{pmatrix} = \begin{pmatrix} c_e c_e^* & c_e c_g^* \\ c_e^* c_g & c_g c_g^* \end{pmatrix} \tag{3.51}$$

The time evolution of the system is obtained by calculating the evolution of the density operator. From this, it is possible to obtain the equation of motion for the elements of the density matrix, thereby describing the evolution of the system. The details of such calculation are quite involved and they are not reported for the sake of the flow of this work, but they can be found in [96, 97].

Before giving the expression of the time evolution of the matrix elements though, in order to accurately model the light-matter interaction, it is necessary to include a spontaneous emission term and a dephasing term. For the spontaneous emission, we include the term $-\Gamma\rho_{ee}$ which empties the excited state and fills the ground state. Regarding the coherences between the states of the system, we assume that they are instead dephased at a rate $\gamma_\perp$. This term is expressed as follows:

$$\gamma_\perp = \frac{\Gamma}{2} + \gamma_c \tag{3.52}$$

In general, in fact, $\gamma_\perp > \Gamma/2$, due to the extra dephasing mechanism beyond the limit of $\Gamma/2$ given by the spontaneous decay. The extra dephasing, with a rate γ_c, can be originating, for instance, from scattering events that do not perturb the populations. The time evolution of the matrix elements is then described by the optical Bloch equations as follows:

$$\begin{aligned}
\frac{d\rho_{gg}}{dt} &= \Gamma\rho_{ee} + \frac{i}{2}\left(\Omega\bar{\rho}_{eg} - \Omega\bar{\rho}_{ge}\right) \\
\frac{d\rho_{ee}}{dt} &= -\Gamma\rho_{ee} + \frac{i}{2}\left(\Omega\bar{\rho}_{ge} - \Omega\bar{\rho}_{eg}\right) \\
\frac{d\bar{\rho}_{ge}}{dt} &= -\left(\frac{\gamma_\perp}{2} + i\delta\right)\bar{\rho}_{ge} + \frac{i}{2}\Omega\left(\rho_{ee} - \rho_{gg}\right) \\
\frac{d\bar{\rho}_{eg}}{dt} &= -\left(\frac{\gamma_\perp}{2} - i\delta\right)\bar{\rho}_{eg} + \frac{i}{2}\Omega\left(\rho_{gg} - \rho_{ee}\right)
\end{aligned}$$

where we defined $\bar{\rho}_{eg} = \rho_{eg}e^{i\delta t}$ and $\bar{\rho}_{ge} = \rho_{ge}e^{-i\delta t}$, $\delta = \omega - \omega_0$, with ω_0 being the frequency corresponding to the transition between the two states and ω the one of the light. Lastly, Ω is the Rabi frequency, which is the frequency of the fluctuations of the populations in the levels, defined as:

$$\Omega = \frac{\vec{d_{g,e}} \cdot \vec{E_0}}{\hbar} \tag{3.53}$$

With $d_{g,e}$ being the transition dipole moment for the transition and $\vec{E_0}$ is the electric field amplitude including the direction of the polarization.

By solving these equations, it is possible to obtain the time evolution of the density matrix elements, thus the time evolution of the quantum two-level system. Now, under the particular assumption of fast decay, the optical Bloch equations simplify to the Einstein rate equation model, as shown in the following.

If we consider the limit of strong collisional damping, for which $\gamma_\perp \gg \Gamma, \Omega$, the system will lose coherence quickly, instead the population evolution will continue to evolve on longer timescales. We focus then only on the slow dynamics, supposing that the coherences are approximately at the equilibrium $\frac{d\bar{\rho}_{ge}}{dt} \approx 0$, making use of the so-called adiabatic approximation. From the optical Bloch equations we obtain:

$$\begin{aligned}
(\gamma_\perp - i\delta)\bar{\rho}_{eg} &= i\frac{\Omega}{2}(\rho_{ee} - \rho_{gg}) \\
(\gamma_\perp + i\delta)\bar{\rho}_{ge} &= -i\frac{\Omega}{2}(\rho_{ee} - \rho_{gg})
\end{aligned}$$

Taking the sum and the difference of the last two equations, we obtain the adiabatic difference of the coherences:

$$\gamma_\perp\left(1 + \frac{\delta^2}{\gamma_\perp^2}\right)(\bar{\rho}_{eg} - \bar{\rho}_{ge}) = i\Omega(\rho_{ee} - \rho_{gg}) \tag{3.54}$$

By substituting Eq. 3.54 in the second Bloch Equation, we finally obtain:

$$\frac{d\rho_{ee}}{dt} = -\Gamma\rho_{ee} - \frac{\Omega^2}{2\gamma_\perp(1+\delta^2/\gamma_\perp^2)}(\rho_{ee} - \rho_{gg}) \tag{3.55}$$

And it is now evident the similarity with the Einstein rate equation Eq. 3.46, where we can clearly identify:

$$\Gamma = A_{21}$$
$$\rho_{ee} = N_2/N$$
$$\rho_{gg} = N_1/N$$

This derivation proves that in the hypothesis of fast dephasing of the two states, the quantum treatment based on the optical Bloch equations is equivalent to the Einstein rate equations, described in section 3.3.1, to describe the time evolution of the system.

This implies that when the fast decoherence is a valid assumption, the rate equation model offers an accurate description of the system's time evolution after a perturbation.

The application of the rate equations to model a real system will be applied in the result chapter in section 6.2, but before that it is necessary to introduce the techniques and methods through which we can monitor the time evolution of a system on ultrashort timescales. The experimental methods and the details about the laser system employed for perturbing and probing the system under investigation are discussed in the following chapter.

3.4 Summary and outlook

This chapter revised the basic theoretical aspects of the light-matter interaction. We started with the problem of retrieving the changes of a light beam propagating through a generic sample. We derived the material specific properties, specifically defining the linear optical constants, the dielectric function and the complex refractive index of a material. We also showed how, if the dielectric function of a material is known, it is possible to derive the optical spectra of a typical spectroscopic experiment or the inverse process (i.e. inverse search) of retrieving the fundamental optical constants starting from the observables of an experiment.

The Lorentz model used to calculate the dielectric function of a material starting from the consideration about the microscopic bound carriers was then outlined, completed the picture about the material specific properties of the light-matter interaction.

We then moved forward to the understanding of the geometrical specific influence on the light-matter interaction, particularly focusing on the case of thin layers.

We derived a general formalism that allowed the calculation of the reflected and transmitted fraction of a stack of thin layers, starting from their dielectric function. We also provided the 2D linearized model as a simplified and slimmer version of the Fresnell transfer matrix approach for deriving the optical observables of a spectroscopic experiment.

It is therefore possible to combine the material and geometrical specific properties to be able to calculate the observable quantities of an optical experiments. Specifically, by modelling the dielectric function of excitons in TMDCs with the Lorentz model, it is possible to calculate the transmitted or reflected light on a monolayer TMDC placed on a substrate. Even more interesting is the inverse search of the dielectric function starting from the optical observable of the experiments, which will be performed in section 6.1

The last section of this chapter then moved forward from the static picture by discussing the time evolution of a system upon interaction with light. The Einstein rate equation and the full quantum optical Bloch equation formalisms were introduced to describe the time evolution of a simple two-level system. The equivalence of the two treatments was demonstrated in the case of negligible coherences.

By using the theoretical basis and framework introduced in this chapter, it is possible to, not only retrieve the state of a system and its properties in a steady-state scenario, but also to track its time evolution upon a perturbation. The main idea is then: if we can change the optical properties of a material by means of photoexcitation and track them as a function of time, supposing that we can also relate the optical observables to an arbitrarily complex energy level model, we can then ultimately understand the system in analysis. This will be treated in section 6.2.

Before proceeding with this, it is necessary to discuss the specific ultrafast optical spectroscopy techniques that are used to investigate the time-dependent response of a material to perturbations. This is reported in the following chapter.

Chapter 4

Experimental section

IIn the last section of the previous chapter, we formalized the time-dependent evolution of a two-level system after a perturbation. This was done by using the Einstein rate equation, or the optical Bloch equation, treatment with which we can describe the excited state population time-dependent evolution. In particular, we derived that, in case of negligible coherences between the states, the excited state population relaxes according to an exponential with a specific lifetime. The typical timescales of the relaxation processes of quasiparticles in semiconductors range from the few femtoseconds to the nanoseconds [28]. Then, when we consider the dynamic screening originating from the presence of quasiparticles in a system, it is essential to track the relaxation of the latter since, as we saw in section 2.2.2, the dynamic screening depends on the quasiparticle density, which varies over time upon photoexcitation. To complicate even more the situation, other physical processes, such as ultrafast thermalization or phase space-filling, for instance, can occur after a perturbation. A convenient way to disentangle the different phenomena governing the recovery of a system back to equilibrium is to separate them temporally. Therefore, it is necessary to employ ultrafast pump and probe spectroscopy to track the time evolution of the exciton dynamics in TMDCs.

This chapter discusses the fundaments of ultrafast time resolved optical spectroscopy in the first section, specifying the experimental techniques of time resolved transmittance contrast and reflectance contrast. We then introduce the basics of the laser system used to generate ultrashort laser pulses to both perturb and probe the ultrafast dynamical response of monolayer TMDC. Finally, the details about the samples investigated in this work, and their growth process, are outlined in the last section of this chapter.

4.1 Optical pump and probe

Fundamental physical processes on different energy scales can appear simultaneously, and it is complicated if not impossible to discriminate between them when investigating only the steady-state properties of a material. Time-resolved spectroscopies allow to disentangle the different phenomena which occur on different timescales temporally. Typical electrons and core ion dynamics happen on timescales

which ranges between a few fs to several ps. Conventional electronic instruments do not have enough bandwidth to investigate such quick phenomena.

To overcome this limitation, the concept of pump and probe experiment was developed. It relies on the concept of taking multiple instantaneous snapshots of a moving object. Thus, the measurements need to happen on timescales shorter than the timescale of the phenomena under investigation. A simple analogy is a photographer that needs to take a picture of a fast-moving object. If the camera's exposure time is too long, the object's contour will be smeared out, but if the camera's exposure is short enough, the moving object will appear sharply on the picture. The same concept applies to optical spectroscopies but on much quicker timescales.

This section outlines the basic concept of time resolved pump and probe spectroscopy in the first subsection. In the second part, we specify the time resolved reflectance and transmittance contrast techniques used to investigate 2D material, and TMDC in our particular case.

In a pump and probe experiment, a high-intensity optical pulse drives the system out of its equilibrium state and a second weak pulse probes it after a specific delay. When the delay between the pump and the probe is controlled, then the temporal evolution of the system can be tracked. In this case, the temporal resolution is given by the time duration of the pulses used in the experiment. The pump role is to perturb the system, and this can be either an excitation of electron or phonon, for example, either way inducing a change in the optical properties. The pump intensity is also fundamental. In fact, for fluences small enough not to perturb the potential landscape of the system under investigation, the recovery dynamics of the system are governed by the same interactions that govern the equilibrium state of the system. Instead, entirely different physics can govern the system when the fluence is high enough to change the potential landscape. The threshold fluence is determined by the physical properties of the system in analysis [98, 89]. Furthermore, the pump photon energy is a fundamental parameter when photoexciting the system. Different photoexcitation energies can lead to different excitation pathways and correspondingly different relaxation dynamics. The same considerations taken for the pump pulse, regarding fluence and photon energy, need to be considered for the probe pulse. Considering that this pulse's primary role is to monitor the pump induced changes in the optical properties of the material (i.e. reflection or transmission), the intensity of the probe needs to be considerably lower than the pump, not to induce further changes in the optical properties. Furthermore, the photon energy of the probe also allows investigating different physics in the response of the sample, for example, different optical transitions in the UV/VIS/NIR range or phononic properties in the Infrared range.

Typically in optical experiments, the measurements of the optical properties at a specific time delay are averaged over many pump and probe pairs. The actual number is determined by the acquisition time and the repetition rate of the laser. The later quantity determines the time interval between subsequent pump-probe

pairs, and it is simply the inverse of the repetition rate. One requirement for spectroscopy is that the system's relaxation happens before the next pump pulse reaches the sample, this meaning that the properties of the system at the negative pump and probe delay correspond to the steady-state properties. This guarantees reproducible measurements of the photo-induced dynamics.

This completes the basic general concept of pump and probe optical spectroscopy. In the following section, the particular pump and probe technique that allows the measurements of the exciton dynamics of a monolayer WS_2 placed on different substrates is described.

4.1.1 Time resolved RC and TC

After discussing the basic principles of ultrafast optical spectroscopy, we now dive into the specific measurements technique employed in this work. When working with 2D material, the main problem is that the propagation length of the light through the material, therefore the absorbed fraction, is limited by its thickness. As we saw in the theory chapter, section 3.1.1, the absorption of a material is proportional to its absorbance and the propagation length of the beam through the material itself. With TMDC materials, despite their high absorbance, the total absorbed fraction of light is weak due to their reduced thickness. Furthermore, the optical signature of the substrate, when this is not transparent, can be present in the optical spectra. Therefore, it is necessary to isolate the contribution to the signal originating from the monolayer TMDC and the substrate-specific response. On top of this, we know from the previous chapters that both the reflected or transmitted light, in/from a sample, carry information about the material and geometric specific properties. The choice of one measurements geometry or the other is mainly dictated by the sample. In the case of transparent or not highly absorbing materials, the transmission geometry is the most convenient choice, but when the sample or the substrate is opaque, reflection geometry is the only available possibility. Furthermore, having a broadband probe instead of a single colour allows the investigation of optical resonances simultaneously. In this fashion, peak shift, broadening, and intensity changes of a resonance in the spectra can be tracked at the same time, and the complete picture of the dynamical response of the system after photoexcitation is provided. The three main requirements for the experiments to be performed in this work are then:

- Measurement adapt for low contrast material
- Substrate insensitive technique
- Broadband probing of the optical spectra

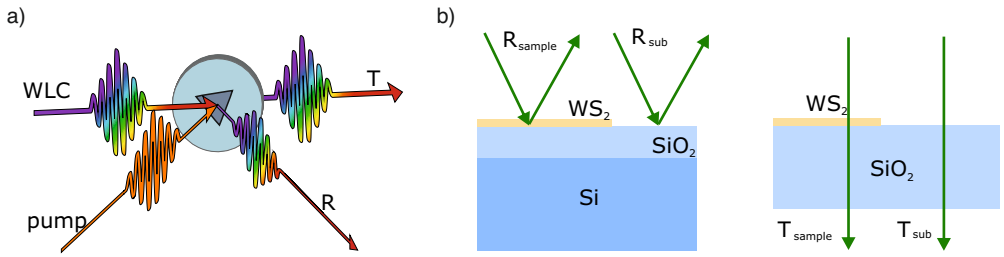

FIGURE 4.1: a) Sketch of the pump and probe beams impinging on the sample with respective transmitted and reflected fraction. b) Experimental geometry of reflectance contrast and transmittance contrast experiments.

To satisfy these requirements, we employ both reflection and transmission experimental geometries, and the measurement techniques used are broadband time-resolved transmittance contrast and reflectance contrast, respectively (tr-TC and tr-RC). In this subsection, we introduce the characteristic of the two methods, specifying how they can be used to investigate monolayer TMDC materials.

Reflectance or transmittance contrast techniques are particularly beneficial to investigate 2D materials, or in general, materials with low optical contrast. In fact, the transmittance (reflectance) contrast are calculated as $TC = (T_{sub} - Tsample)/T_{sub}$ ($RC = (R_{sub} - Rsample)/R_{sub}$), where the index sub is referred to the transmittance (reflectance) of the bare substrate and $sample$ to the complex of substrate and thin layer on top of it, as shown in Fig. 4.1.b). These observables are particularly sensitive to small signals due to the normalization over the transmission (reflection) of the substrate. Furthermore, thanks to this normalization, the thin film signal, or TMDC in our specific case, is isolated from the signal originating from the substrate in the case of the thick transparent substrate and assuming negligible interaction between the two. Such techniques satisfy the first two requirements mentioned above. The last requirement is satisfied by using a broadband white light pulse to probe the transmittance/reflectance of the sample. Details about the broadband white light probe are provided in subsection 4.2.1.

In a typical tr-TC/tr-RC experiment, an optical pump pulse, tunable in photon energy, perturbs the system out of its equilibrium. The probe broadband, covering a broad energy range, allows to monitor the signature of electronic transition in optical spectra. By varying the time delay between the pump and the broadband probe, it is possible to obtain the time-dependent evolution of the spectra upon photoexcitation. This is sketched in Fig. 4.1.a). We also remark that before the cross-correlation of the pump and the probe (defined as t_0), the sample's optical properties are the same as the equilibrium conditions. After photoexcitation, the RC/TC contrast spectra is changed, reflecting the changes in the energetic structure (energy levels shift) or interactions (broadening) contributing to the observed lineshape.

However, the mechanism governing the observed peak shift, broadening and

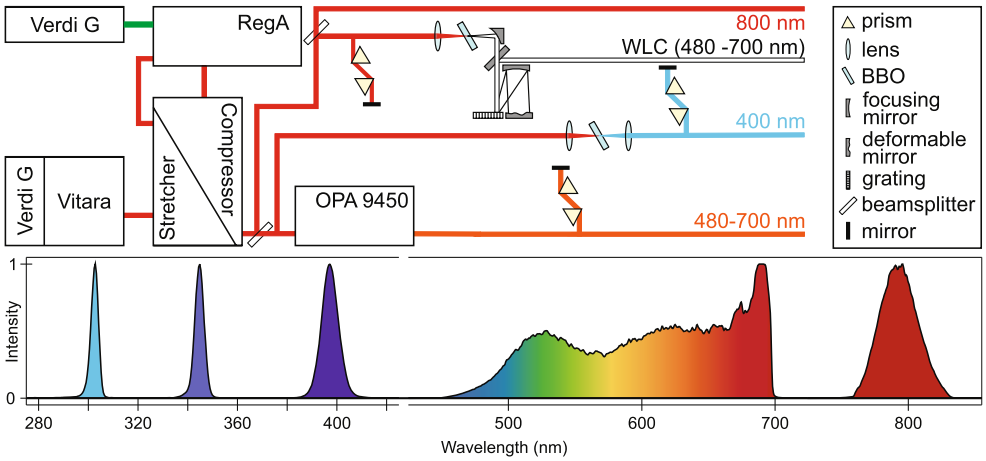

FIGURE 4.2: Sketch of the Coherent femtosecond laser system and experimental setup. A Ti:Sa oscillator (Vitara) seeds a regenerative amplifier (RegA) which is pumped by a CW-OPSL (Verdi G). The RegA output is compressed and then divided with a 50-50 beamsplitter (BS). One half is used to generate the optical pump either through a collinear optical parametric amplifier (OPA 9450) or by being doubled to 400 nm. 10% of the remaining half generates the WLC. Bottom: spectra of the pulses used in this work. Figure adapted from [99]

intensity changes of the resonance can be different according to the system in analysis. The interplay between different phenomena is not trivial and depends on the fundamental interactions and properties of the system. The explanation of this will be given in the next chapter. Before discussing that, the details of the laser system used for generating ultrashort pulses used for this experiment and the experimental details are presented in the following section.

[Fork84]

4.2 The Femtosecond laser system

As already mentioned in the introduction of this chapter, we know that typical electronic processes happen as fast as sub ps timescales. To investigate such ultrashort processes, at least equally short light pulses are needed. These pulses are provided by a commercial Coherent tunable amplified femtosecond laser system.

This section provides the details about the laser system and the components used to generate light of various photon energy through non-linear optical processes.

The laser system, and the relative spectra of the radiation that can be obtained with it, are depicted in Fig. 4.2. The system is based on the Vitara-T oscillator and the regenerative amplifier RegA 9040. Both these lasers are based on a Titanium doped sapphire crystal (Ti:Sa) which absorbs in the wavelength range from 400 to 600 nm. The emission from the crystal covers the wavelength range from 680 to 1100nm and with a maximum centered at 790 nm. The Vitara and RegA are pumped with two

continuous-wave optically pumped semiconducting lasers (CW-OPSL) emitting at 532 nm, Coherent Verdi-G5 and Verdi-G18, respectively.

The Vitara oscillator is a standalone sealed unit and emits 7.3 nJ pulses at 800 nm (1.55 eV) with 60 nm bandwidth and a repetition rate of 80 MHz. These pulses are obtained by exploiting the passive Kerr-lens modelocking [100], occurring when the refractive index of the gain medium is dependent on the field strength. The output of the Vitara is then compressed to less than 20 fs by an internal prism compressor. By propagating the different frequency components for different lengths in the prisms, a negative chirp is introduced to compensate for the positive chirp, originating from the propagation of the beam through dispersive media. The detailed working mechanism of the prism compressor is described in detail in [101].

The output pulse of the oscillator is not sufficiently powerful to drive non-linear optical processes. Instead, the latter is used as a seed for the regenerative amplifier RegA. To not damage the gain crystal, the output of the Vitara is sent into a stretcher which increases the temporal length of the pulse by multiple reflections on specifically arranged gratings [102]. Now the pulses are coupled into the RegA through the cavity-dumper, which is a Tellurium Dioxide (TeO_2) acusto-optic modulator. While the seed pulse is propagating through the cavity, it gets amplified at every propagation through the gain crystal. The amplification continues up to a level of saturation when the population inversion of the gain crystal is wholly depleted (20 roundtrips of the cavity). At this point, the pulse is ejected from the cavity through the cavity dumper. The cavity dumper works in conjunction with the Q-switch, a second opto-acoustic element that prevents simultaneous lasing and injection of the seed pulse. By degrading the cavity's quality, such a component guarantees that the gain crystal can restore population inversion before the next seed pulse is coupled into the cavity. The frequency of the injection/ejection determines the repetition rate of the laser, which is tunable from 4kHz to 250kHz. In typical operations, and in all the works presented in this thesis, the laser repetition rate is set at 200kHz.

The output of the RegA is then compressed to 40 fs by multiple reflections on a second set of dispersive gratings. The output pulse energy is 7 μJ, and the spectrum is visible in the bottom part of Fig. 4.2.

The compressed output is then divided with a 50/50 beamsplitter. One of the two beams generates the pump, either through second harmonic generation or an optical parametric amplifier (OPA model Coherent OPA 9450). in both cases, the pump is compressed using a specifically tuned prism compressor and then sent to the sample.

For the second harmonic generation, 20% of the 800 nm photons are focused into a BBO crystal (β-barium borate). Only 20% is used to avoid damage to the non-linear crystal. When the photon density is high enough, the same photons interact with the non-linear crystal, producing photons at double the incoming photons' energy (half wavelength). The details of such a process are described in [103]. The output consists of 400 nm pulses with preserved coherence.

The OPA is seeded with the 800 nm beam and returns an output beam with photon energy tunable within 700 to 500 nm range. These wavelengths are achieved by amplifying a selected spectral component of a white light, generated by focusing the seed in a sapphire crystal, through pumping with 400 nm photons, obtained from the second harmonic of the seed. These pulses are overlapped spatially and temporally in a non-linear crystal. Since the pump pulse is shorter in time than the white light, the amplified frequency is selected by varying the delay between the white light and the 400 nm pump. The phase-matching angle of the crystal is then optimized to guarantee maximum efficiency in the energy transfer from the pump pulse to the signal beam. In the OPA, this amplification process happens two times within the same crystal. The OPA output signal is set at 625 nm (1.98 eV) for the experiment in this thesis.

The 10% of the second half of the fundamental 1.55 eV is used to generate the white light continuum in a sapphire crystal, and it is described in detail in the following section, and the remaining is used as a pump to characterize the white light temporal dispersion.

Summarizing, a complete description of the experimental details and the laser system was outlined in this section. Further details about the broadband white light generation and compression are provided in the following subsection.

4.2.1 Broadband white light generation and compression

When performing linear optical experiments in general and on TMDCs in particular, the resonances in the optical spectra can be broad in energy. Furthermore, upon photoexcitation, such resonances can shift, broaden and vary in intensity. When performing two-colour pump and probe experiments, extracting all of the information regarding the temporal evolution of the spectra is hardly achievable, if not impossible. Employing a broadband white light pulse allows probing the system's response simultaneously at multiple frequencies. Furthermore, the wider spectral width of a broadband pulse allows for the compression of the latter to a very short time duration, therefore improving the temporal resolution of the experiments. As with the white light generation in the OPA previously described, the generation of broadband white pulses generally does not guarantee a short pulse duration. However, if the temporal dispersion of the pulse is known though and controllable, the broadband pulse can be compressed down to a few fs time duration.

This subsection describes the broadband white light pulse generation and compression details and methods used in this work.

The white-light continuum generation and compression setup was developed from Wegkamp et al. in [104, 89] and it is sketched in Fig. 4.3.a). As mentioned earlier, 5% of the total power of the RegA output is isolated with a beam splitter and focused in a sapphire crystal to generate white light (WL). Sapphire has been prefered to YAG crystal or others due to the wider bandwidth of the generated WL,

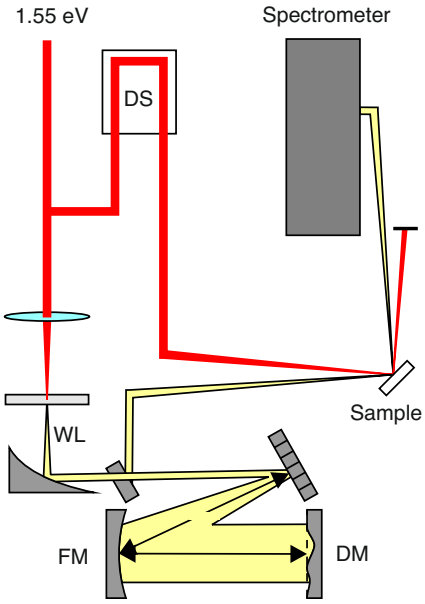

FIGURE 4.3: Sketch of the white-light generation and compression setup. 5% of the output of the RegA is focused on a sapphire crystal to generate WL. The WL compression is achieved through a deformable mirror compressor and then focused on the sample, in spatial overlap with 45% of the remaining 1.55 eV. The reflected/transmitted WL is then steered in a spectrometer.

despite a lower intensity. Third-order non-linear effects such as the Kerr-lens effect and self-phase-modulation induce filamentation and spectral broadening of the seed. Those effects and the plasma formation, as discussed in detail in [105, 106], leads to broadband white-light filaments with roughly 10 pJ/nm pulse energy densities.

The WL is then collimated with a parabolic mirror and steered to the compressor. Here the WL is initially dispersed by a grating (G - Richardson Gratings, 600g/mm, blazed at 500nm). The first order of diffraction is then focused from a spherical mirror (FM) onto a deformable mirror (DM). The compressor configuration is such that both the DM and the grating are at the same distance from the FM, in a so-called 4-f configuration.

The DM consists of an aluminium coated polymeric membrane which 30 electrostatic actuators can deflect. By deforming the membrane, the accumulated phase of a transmitted laser pulse can be changed. In such a way, the natural dispersion of the different wavelengths is compensated by changing the path length of the respective components.

The back-reflected WL from the DM follows the same optical path of the incoming beam, and it is separated by slightly tilting the DM in the vertical direction. The out-coming beam is then steered and focused to the sample, which can be either an LSMO ($La_{0.5}Sr_{1.5}MnO_4$) crystal (for reflectivity measurements) or VO_2 (for transmission measurements). The White light is then re-collimated and steered into a spectrometer which allows the measurement of the broadband reflected/transmitted

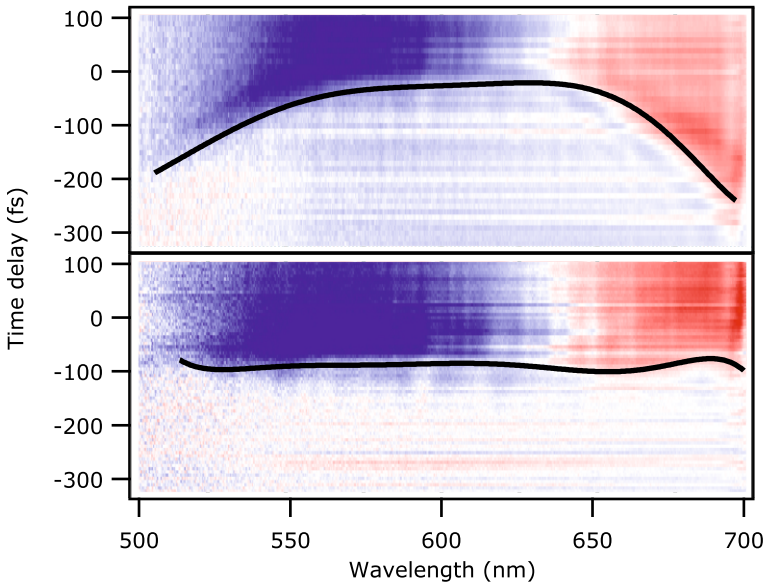

FIGURE 4.4: Differential reflectivity (false color plot) of LSMO as a function of time delay (y axis) and wavelength (x-axis) upon excitation by a 1.55 eV pump pulse, probed by uncompressed (top) and compressed(bottom) WLC pulses. The extracted dispersion of the WLC is reported with black lines in both graphs.

WL. The 45% of the RegA output after the first beam splitter is steered onto a delay stage and then focused to the sample in spatial overlap with the WL beam.

A pump-probe experiment is used to visualize the dispersion of the WL as reported in Fig. 4.4.b). In the top panel, the differential time-resolved differential reflected fraction of the LSMO sample is reported as a function of probe Wavelength (x-axis) and the time delay between the 1.55 eV pulse and the WL. The temporal dispersion of the WL is overlaid on the same axis. The LSMO [104](VO$_2$ [107]) have an instantaneous build-up of the signal, such that the dispersion of the WL can be obtained by fitting the rise of the signal with a step function, as described in details in [104, 89]. Different methods can be used to extract the WL dispersion: extraction of the half maximum of the rise, the calculation of the derivative of the data to find the maximum, and the fit of the rising edge with a normalized error function. All of these methods have been used recursively in this work, making sure to use the same procedure across different iteration. The temporal dispersion of the WL is then fitted with a polynomial function, and it is fed to an algorithm implemented in IGOR Pro. This algorithm allows the retrieval of the desired mirror deformation and converts it into the voltage needed by the actuators of the mirror. All the principles of this algorithm are described in [108]. Once the deformation is applied to the mirror, another time-resolved scan of the differential reflectance/transmittance is performed, and the corresponding WL dispersion is extracted. The WL's optimal compression is generally obtained after iterating this procedure 2/3 times. Fig. 4.3.b) bottom panel reports the tr-reflectance of the LSMO as a function of probe Wavelength (x-axis) and time delay. The extracted WL temporal dispersion is overlaid on the same axis. The

temporal duration in this measurement is 15 fs.

We have finally treated all the aspects of the laser system relevant for this work, including the white light generation and compression. We now move forward to the technical details of the sample in analysis before proceeding further to the results.

4.3 Samples

Monolayers TMDC can be synthesized in different ways [109], most commonly though exfoliation or chemical vapour deposition. Furthermore they can also be transferred placed on various substrates. Therefore, it is essential to know the complete details regarding the preparation process and properties of these samples because the different preparation techniques or substrates, where the monolayer are placed to, can alter the optical response of this material [110].

In this subsection, we describe the TMDC sample investigated in this work, providing details regarding their growth and properties.

The samples investigated in this work are pristine monolayers of WS_2 obtained by mechanical gold assisted exfoliation technique. Our collaborators performed the production of these samples at Columbia University. The details regarding the synthesis can be found in ref [111, 112]. With this method, a thin layer of gold is grown on top of a bulk CVD grown WS_2 crystal placed on adhesive tape. The layer of gold is peeled away with a thermal release tape, dragging the topmost layer of the WS_2 crystal. This occurs because the interaction strength between the gold and the first WS_2 layer is stronger than the WS_2 interlayer interaction strength. The thermal tape is placed on the substrate of choice and etched away. Finally, the sample is cleaned with acetone and isopropyl alcohol, leaving clean large area monolayers on the substrate.

The three substrates used in this work are a thick amorphous fused silica glass (FS) substrate, a layered Silicon/ Silicon oxide (Si/SiO_2) substrate, and a sapphire substrate. Both the FS and sapphire substrates are 1 mm thick glass and polished on both sides. The Si/SiO_2 is a 1 mm thick Silicon Wafer covered by a 285 nm ($\pm$ 5%) thick layer of silicon oxide. The large area WS_2 monolayers are visible in Fig. 4.5, placed respectively on the Si/SiO_2 and FS sustrates, respectively. The bare substrate corresponds to the lightest colour in both panels, and clean monolayers areas are the parts with the least colour contrast to the substrate. Pristine monolayers areas with size in the order of the 100's of micron are visible and marked in the figure. The darker areas correspond to multilayer flakes commonly obtained when using the exfoliation technique. The samples, when not measured, were stored in vacuum. All the experiments have been performed at room temperature and in atmosphere.

The details of the TMDC samples investigated in this work were outlined in this section. Their transient optical response is investigated in chapter 6, but before that, we summarize this chapter in the following.

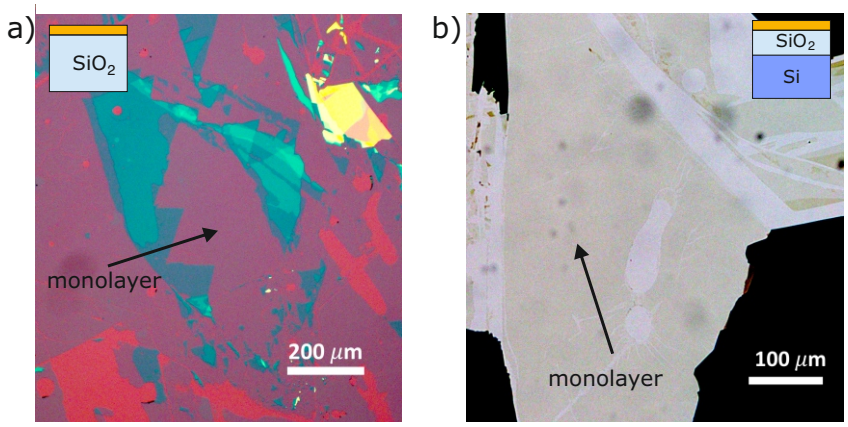

FIGURE 4.5: The optical microscope images are shown for WS_2 samples deposited on a) Si/SiO_2 and b) FS substrates, respectively. Areas of clean monolayer are indicated by the arrows. Areas with different colours are the substrates or multilayer areas. Insets: Sketches of the geometrical configuration of the samples.

4.4 Summary and outlook

We started this chapter by motivating the need for ultrafast time resolved experiments to investigate the quasiparticle dynamics upon photoexcitation in semiconductors. Due to the fast nature of the relaxation processes after an optical perturbation and the mixing of different effects, such as quasiparticle screening or ultrafast thermalization, a pump and probe experiment is the ideal choice to track and disentangle these effects temporally.

In this chapter, we have discussed how we drive the system out of the equilibrium and investigate it on ultrafast timescale, focusing on the experimental details of the methods employed in this work. The first part discussed the fundaments of ultrafast time resolved optical spectroscopy. In particular, the techniques of tr-RC/TC were identified as the ideal techniques to investigate low dimensional TMDC. From this point, the experimental detail of the laser system, and the working principle of the latter, were treated in the second section. Particular attention was reserved for the broadband white light probe, its generation and its compression to have an ideal light to map the optical response of TMDC on a wide spectral area and with sub 10 fs time resolution. Ultimately, the experimental details and the growth methods of the WS_2 samples were outlined in the last part.

We have now all the fundamentals to start discussing the result of this thesis. Before that, we recall the motivation and the scientific question of this work and, now that we introduced ultrafast optical spectroscopy, we review the literature available on ultrafast dynamics in monolayer WS_2.

Chapter 5

Contextualization and scientific questions

The first three chapters of this thesis introduced the fundamental properties of TMDC materials, reviewed the theory regarding the light-matter interaction to describe the optical response of these materials, statically and dynamically, and described the experimental details of time-resolved pump and probe spectroscopy. It is now convenient to review the available literature regarding the exciton dynamic response in monolayer TMDC to establish the context and the basic ground on which this work develops. In fact previous studies investigating the origin of the dynamic exciton response are already reported in literature. However, the knowledge about the phenomena concurring in the changes of the excitonic resonance is not complete yet, since a comprehensive and quantitative picture of the interplay of the various phenomena is not reported yet. Nonetheless, despite some difficult comparison between them, there are a few major studies which provide a pivotal contribution towards the understanding of the exciton non equilibrium properties of TMDC, as well as contributing to the base ground on which this work is developed.

n this context, this chapter reviews the primary studies on the TMDC's dynamical optical response upon photoexcitation. In particular, I discuss the main works dealing with the quasiparticle dynamic screening and its effect on the exciton dynamics in WS_2 monolayers. Furthermore, the other competing mechanisms that contribute to the exciton dynamic response, such as ultrafast thermalization or phase space-filling effect, and their role in the dynamics are discussed. The common observations between three major studies and the remaining open questions are highlited. Finally, from the literature review and the previous chapter, I recall and contextualize the questions that still need to be answered to understand the complex interplay of phenomena in the exciton dynamic response upon photoexcitation. These will be summarized in the second part of the chapter, where a list the scientific question that this work will try to answer in the next chapter is outlined.

5.1 Literature review on ultrafast dynamics

The investigation of the ultrafast exciton dynamics in TMDC material attracted considerable interest in recent years [30, 31, 32, 33, 27, 90, 113, 34, 114, 61, 115], since the understanding of the non-equilibrium physics of these material is necessary for the applicability in device physics. A multitude of studies employing different experimental techniques were published to unravel the main origins of the exciton dynamic response upon photoexcitation. Undoubtedly, time-resolved optical spectroscopies contributed fundamentally to the current knowledge regarding the non-equilibrium physics in monolayer TMDC materials. Exactly those remarkable insights must be taken into account when defining the scientific question that this work tries to answer.

This section summarizes the main studies, their contributions and findings, regarding the origin of the non-equilibrium exciton response in WS_2 monolayer upon photoexcitation.

When a semiconductor, in particular a TMDC, is photoexcited, a quasiparticle population is generated in the system. It is not clear a priori if these quasiparticles are excitons or QFC, and it depends on the excitation conditions [90]. Either way, their presence can significantly change the excitonic properties of the TMDC. The mechanisms through which this happens can be multiple and depends on the excitation density. The intermediate density regimes (i.e. that the average separation between photoexcited quasiparticles in 2D is larger than the Bohr radius of the excitons, but exciton-exciton can not be neglected) is taken into consideration, where photoexcited quasiparticles can be either excitons or QFC. For higher excitation densities, plasma effects are the dominant cause of the non-equilibrium response [33]. The main works dealing with intermediate excitation densities on WS_2 monolayers, investigated with optical pump and probe spectroscopy, showed that, upon photoexcitation, the excitonic resonance could shift, broaden and change its spectral weight. These behaviour were observed in the three main studies performed on WS_2 monolayers employing time-resolved optical spectroscopies, which are discussed in the following.

Starting from the work of Sie et al. [31], they measured the absorbance of a CVD grow monolayer WS_2 placed on a sapphire substrate, pumped with a 3.1 eV pump pulse. They observed a redshift ΔE of the resonance upon photoexcitation, accompanied by a broadening $\Delta\Gamma$ and reduction of the peak maximum intensity I, without changing the spectral weight ΔS. Those trend are shown in Fig. 5.1.a). Eventually, for higher excitation densities, the redshift diminishes in intensity. This was explained with plasma effects and an attraction-repulsion crossover in the exciton–exciton interaction that mimics a modified Lennard-Jones potential between atoms. Exactly this work proved how the exciton-exciton interaction is fundamental to explain the observed dynamic In their work they exclude the influence of thermal effects to the exciton dynamic response originating from the increase of the lattice

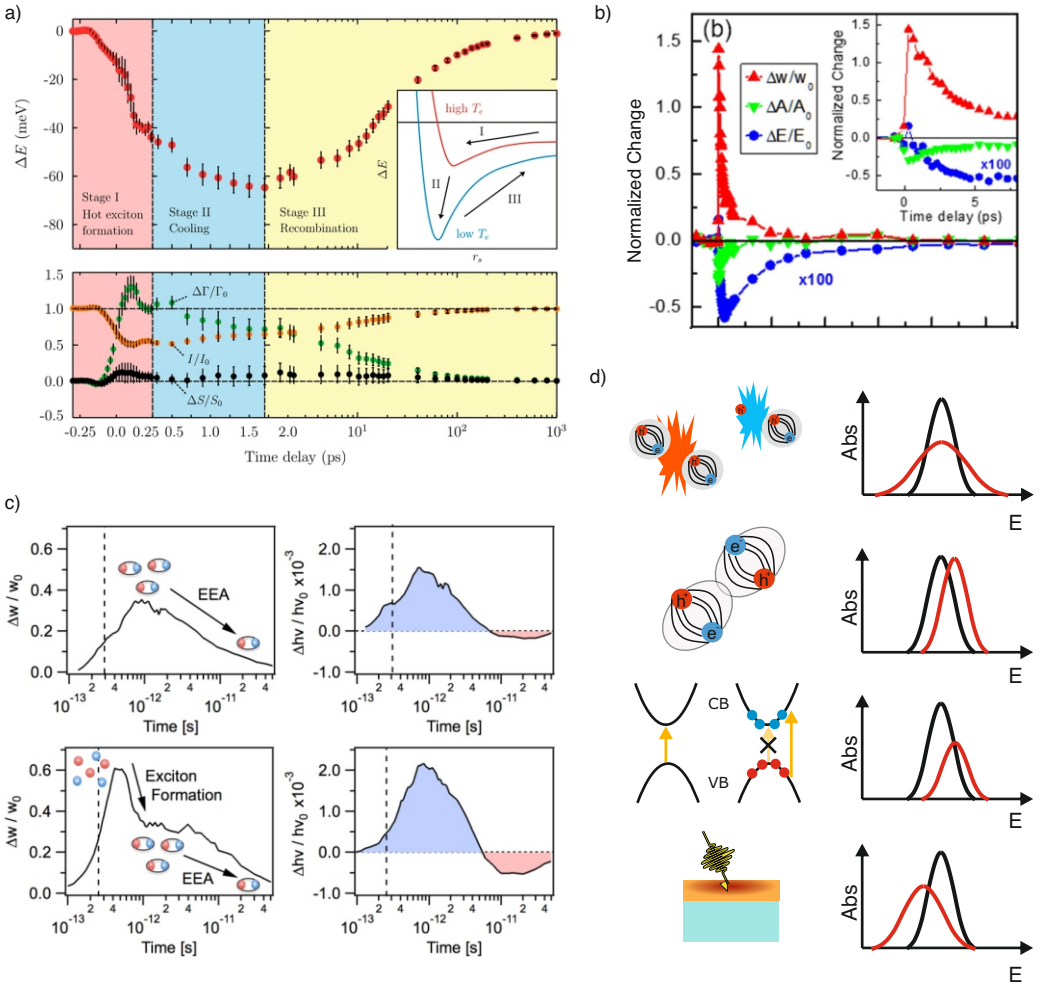

FIGURE 5.1: Exciton dynamic response upon photexcitation of monolayer WS_2a) Time-dependent Exciton peak shift, broadening, intensity, and spectral weight changes taken from [31]. b) Time-dependent normalized changes of exciton resonance energy, linewidth and intensity taken from [32] c) Time-dependent Exciton peak shift and broadening for resonant and above-resonance photoexcitation. data taken from [30] d) sketches of the effects on the exciton resonance from scattering, dynamic screening, phase-space-filling and temperature increase.

temperature.

Another study, performed by Cunningham et al. [30], resolves the time-dependent absorption coefficient of a monolayer WS_2 placed on a fused silica substrate. The photoexcitation process was changed with a tunable pump pulse from 2eV to 2.6 eV. In Fig 5.1.c) the exciton peak shift $\Delta h\nu$ and broadening Δw for resonant and above-resonance photoexcitation are reported as a function of time delay. They observe an initial blueshift of the resonance, which later turns in a redshift. This was qualitatively explained by binding energy reduction and quasi-free particle bandgap renormalization originating from a competition of different effects including Dynamic screening of the CIA, phase-space filling and scattering and the subsequent redshift is attributed to thermal effect. Furthermore, a stronger broadening is observed for above-resonance photexcitation, which was ascribed to the presence of quasi-free carriers. No quantitative details about the interplay of the mentioned phenomena were provided though since they focused on retrieving the time-dependent exciton binding energy. It is already clear that there is a mismatch of the observed peak shift between the two experiment discussed where an initial red/blue shift was observed, respectively. This could be tentatively accredited to the different nature of the sample and excitation conditions, but it is complicated to compare the two different experiment due to the separate method of tracking the time evolution of the excitonic resonance.

To try to shine some light on the differing observation of the two aforementioned study we now move to another study. Ruppert et al. [32] investigated the reflectance contrast of a mechanically exfoliated monolayer WS_2 placed on a fused silica substrate photoexcited with a 2.4 eV photon energy ump pulse. They extract the peak shift ΔE, broadening Δw and spectral weight changes ΔA of the exciton resonance finding a short lived initial blueshift turning rapidly in a redshift. After qualitatively attributing the initial blueshift to the dynamic screening of the Coulomb interaction and the phase space-filling effect, they report that the slower dynamics are ascribable to thermal-induced effects due to the prevalence of the Auger like mechanism of recombination, which transfers energy to the lattice.

Also this last work shows differing exciton dynamic response and, again, this can be tentatively attributed to the different excitation conditions or to the fact that the monolayer WS_2 was exfoliated and not CVD grown. The initial blueshift is consistent with the observations from the work of Cunningham et al. [30] but occours on dissimilar timescales. Once again here the analysis used to track the exciton dynamic response is not easily comparable to the other two works. To shine light on the various exciton dynamic response reported in the three experiments, a complete formalism that allows the reliable comparison between data form different experiments, samples, substrate and excitation conditions is needed.

Before summarizing the current knowledge regarding the causes of the observed non-equilibrium response of the TMDC it is necessary to highlight the problems and

relative open question arising from the analysis of the literature. First, all these studies measure or retrieve different observables, which are modelled in different ways, rendering the comparison between them difficult, if not impossible. This is clear since the observed exciton dynamics of peak shift in the three experiments are not matching between the different works. This does not mean that the experiments contradict each other, but the samples, measurements and excitation conditions were different in the three different experiments. Secondly, the description of the dynamics is mainly qualitative and not quantitative, and the contributions originating from the different phenomena contributing to the dynamics are not quantitatively determined.

Nevertheless those works give the first qualitative picture of the origin of the observed exciton non-equilibrium dynamics which are summarized in Fig. 5.1.d) and reported in the list below, following the same order as in the figure:

- Scattering between quasiparticles, thus leading to broadening of the excitonic resonance, formation of trion or biexciton, non-radiative recombination through Auger-like scattering.
- Dynamic screening of the Coulomb interaction, analogous to what was described in section 2.2.2, where the quasiparticles screening of the CIA leads to the shift of the exciton resonance energy. It is not clear if this results in a red- or blue-shift of the latter, since it depends on the respective ratio of binding energy reduction and band gap renormalization
- Phase-space-filling effect due to the presence of quasi-free carriers, due to Pauli exclusion principle. This phenomena occurs when photoexcited carriers occupy the conduction band states, thus not allowing the photogeneration of an excited carrier with same quantum number. This generally leads to a shift of the excitonic resonance towards higher energies, and to the reduction of the spectral weight as shown in the sketch.
- Ultrafast thermalization, due to efficient electron-phonon coupling, where non-radiative electronic transitions transfer energy to the phonon bath system, eventually increasing the lattice temperature and inducing shift or broadening of the resonance through the mechanisms expleained in section 2.1.4.

The competition of all these effects results in the observed exciton dynamic response but no quantitative comprehensive picture was reported yet in literature. This is why, to understand the non-equilibrium physics of TMDC material, it is fundamental to quantitatively unravel the mechanism, timescales and relative ratio of these phenomena.

Through the review of those three primary studies regarding exciton dynamics on WS_2, it is now clear how and why they set the foundation for the research on the subject matter. They all demonstrate the causes and phenomena behind the observed dynamics from a qualitative point of view. The two main complications were

also outlined, these being the difficult comparison between various experiments and the lack of a comprehensive and quantitative picture of the phenomena contributing to the dynamic exciton response. From these, the questions that this thesis will try to answer are formulated in the following section.

5.2 Open questions

In the previous section, I summarized the primary studies regarding the ultrafast exciton dynamics in monolayer WS_2. In particular, the phenomena that lead to the observed linewidth broadening, peak shift and spectral weight variation of the excitonic resonance upon photoexcitation were reviewed. The two main complications that arise from the studies reported in the literature so far was also evidenced. First, the difficulty in comparing different woks and experiments and secondly, the lack of a comprehensive quantitative picture of the different phenomena contributing to the exciton dynamics.

This section formulates the question that this thesis will try to answer in the following chapters, based on what is the current knowledge regarding the non-equilibrium physics of of TMDC materials.

Firstly, it is clear from the literature review that the comparison between different studies is not trivial. In fact different exciton dynamic response were observed in different studies. Particularly red/blueshift were observed with various magnitudes. This dissimilar trends were attributed to different samples or different excitation conditions.Nevertheless, to advance towards the understanding of the exciton dynamics in monolayer TMDC, it is fundamental to be able to compare different experiments when different techniques, samples, and substrates are used. Therefore, there is the need for a formalism that allows the retrieval of quantitative information about both the static and dynamic exciton response independently of the above-listed variables.

Secondly, all the studies reported in the previous section focus on some specific aspect of the exciton dynamic response upon photoexcitation. However, a comprehensive quantitative picture of the interplay of the different effects and phenomena contributing to the observed dynamics is still missing and it is a key step towards the ultimate understanding of the non-equilibrium phyiscs of those materials. The result of the interplay between scattering, phase-space filling, ultrafast thermalization and dynamic screening of the Coulomb interaction still needs to be discovered.

In particular, the last effect of screening of the Coulomb interaction between the electron and the hole constituting the exciton is interesting from a fundamental point of view since, in the intermediate density regimes and for W based TMDC, it is the dominant cause for the dynamics [27]. As known from the chapter 2, both the static and dynamic screening contribute to determine the exciton resonance energy. When quasiparticles are transiently present in the system, dynamic screening of the

Coulomb interaction induces a shift of the exciton resonance attributed to the competition of Quasi-free particle bandgap renormalization and exciton binding energy reduction, but the quantitative details of such a process are not determined yet. Particularly the different nature of QFC and exciton suggests that the corresponding dynamic screening might be different, as also seen in section 2.2.2. Thus, the question that arises from this is: how do different quasiparticles dynamically screen the Coulomb interaction? To answer this question is necessary to track the quasiparticle population and their relaxation mechanism at any given time after photoexcitation. Furthermore, does the static screening of the dielectric environment play a role in the exciton dynamics?

To conclude this chapter, in order to have a guideline to proceed through the result chapter, I list the questions that this work tries to answer:

- How to extract quantitative information about the exciton static and dynamic response that also allows the comparison between different experiments, measurements techniques, samples, and substrate of choice?
- Which are the different relaxation mechanism that governs the recovery of the system after photoexcitation?
- How do the static and dynamic screening of the Coulomb interaction play a role in the exciton dynamic response upon photoexcitation, and how it competes with the other phenomena?
- How do different quasiparticles (i.e. excitons and QFC) dynamically screen the Coulomb interaction, therefore contribute to the exciton dynamic response in TMDC?
- How do static and dynamic screening compete in the determination of the static and dynamic exciton response?

This concludes the first part of the this work and provides the set of questions that needs to be answered. From the previous chapters, all the necessary knowledge and tools that are pre-required to tackle them are also available. The next chapter will start with the first one of the list at the, progressively moving on to the others while discussing the results.

Chapter 6

Results

6.1 Ultrafast evolution of the complex dielectric function of monolayer WS_2 after photoexcitation

As mentioned in the theory chapter 3, electronic transitions contribute to the optical susceptibility and to the dielectric function, and assumptions are indispensable to retrieve these quantities from the optical spectra of the material under investigation. In addition, it was explained how the optical response of the TMDC is particularly sensitive to external factors such as temperature, doping, impurities and particularly screening effects from the environment. Therefore, being able to quantitatively compare the optical properties in such materials is crucial, and it is the basis for analyzing how different interactions lead to the steady-state and dynamical response of different samples, in different environments, and from various measurement techniques. It becomes clear that there is a need for a proper formalism to describe the steady-state and dynamic response of TMDC materials quantitatively. This is particularly relevant for the dynamic response of these materials, which can be different compared to their equilibrium counterpart.

This section derives and discusses a formalism that allows the quantitative comparison of the exciton dynamics in WS_2 monolayers from independent femtosecond time-resolved optical spectroscopy experiments on different samples and substrates. This is achieved by employing two different models for retrieving and tracking the complex dielectric function in the steady-state and dynamic response upon photoexcitation of monolayers WS_2 deposited on two different substrates and from two independent measurement techniques.

Section 6.1.1 presents the extraction of the exciton lineshape in the transmittance contrast spectrum of a monolayer WS_2 deposited on a thick transparent FS substrate. The excitonic contribution to the complex dielectric function is isolated by combining the 2D linearized model discussed in Chapter 3 and assuming that the exciton can be described by a Lorentz oscillator. The analogous modelling of the exciton lineshape from the reflectance contrast spectrum for a monolayer WS_2 placed on a layered Si/SiO_2 substrate is then presented and described in section 6.1.2 by using a more general Fresnel transfer matrix formalism. In section 6.1.3, by fitting these

two models to the tr-TC and tr-RC, I track the time evolution of the complex dielectric function of the excitonic resonance upon photoexcitation in both samples. Lastly, the static and dynamic exciton responses are retrieved from the two different measurements, and the analyses are compared and discussed in section 6.1.4.

The coincidence of the non-equilibrium exciton response is observed in the two independent measurements. This demonstrates that the methods used for the extraction of the time evolution of the complex dielectric function are stable for different samples, substrates and measurement techniques and can be compared quantitatively within the accuracy of the photoexcitation density determination. The photoinduced non-equilibrium dynamics are independent of the substrate of choice but are sensitive mainly to the excitation condition, therefore, to the excited quasiparticle population. The last dependency is discussed carefully and systematically in section 6.2.

This section is based on my work previously published during my PhD [116]

6.1.1 Monolayer WS_2 on fused silica substrate

The main target of this subsection is to isolate the exciton contribution to the complex dielectric function from the steady-state transmittance contrast (TC) spectrum of a monolayer WS_2 placed on a thick fused silica substrate. The theory chapter describes how different assumptions can be used to achieve this.

In this case, the main assumption is that the exciton contribution to the dielectric function of the WS_2 can be modelled with a Lorentzian oscillator. Using the 2D linearized model, the analytical formula of the lineshape of the exciton is derived, which is then fitted to the steady-state TC spectra to retrieve the exciton contribution to the dielectric function.

The steady-state TC spectrum of a monolayer WS_2 placed on a thick fused silica substrate is shown in Fig. 6.17 with the black markers. A resonance in the spectrum is observed at 2 eV, and a background absorption, more prominent on the higher energy side of the resonance, is also evident. The close vicinity of the resonance energy to the value reported in the literature allows us to conclude that the resonance corresponds to the A exciton absorption. The background signal is due to the tail of higher-lying electronic transition [117].

To quantify the excitonic signature in the TC optical spectra, I make use of the 2D linearized model introduced in section 3.2.2. The transmittance contrast in the assumption of low contrast (TC «1) is given by the equation:

$$TC = -Re\left[\frac{2}{1+n_{sub}} Z_0\sigma^s\right] \tag{6.1}$$

$$Z_0\sigma^s = -i2\pi(n_{WS_2}^2 - 1)(d/\lambda) \tag{6.2}$$

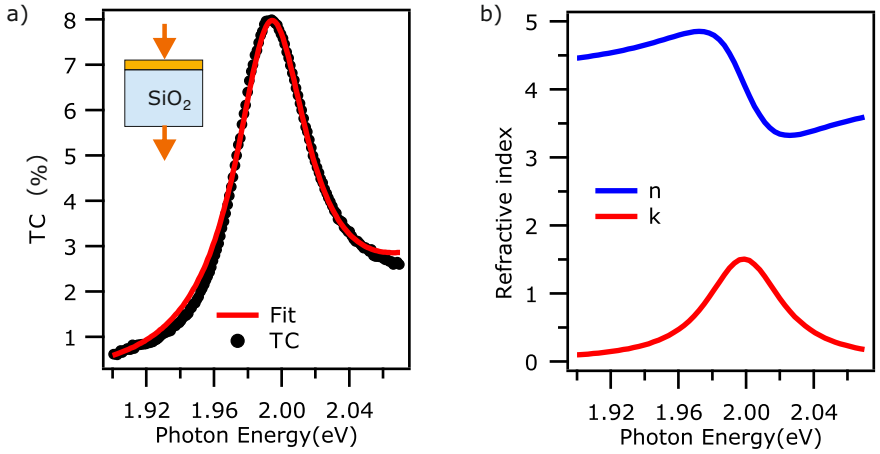

FIGURE 6.1: a) Steady-state TC contrast spectra of monolayer WS_2 deposited on a thick FS substrate and best fit using Eq. 6.4. b) Real and imaginary part of the exciton contribution to the complex refractive index, calculated from the parameters extracted from the best fit of the TC steady-state spectrum.

Where n_{WS_2} and n_{sub} are the refractive indices of the monolayer WS_2 and the substrate, respectively, $Z_0\sigma^s$ is the dimensionless sheet conductivity, d is the thickness of the monolayer, and λ is the wavelength.

The thickness of the WS_2 monolayer was measured with the AFM and found to be $d_{WS_2} = 0.7$ nm, whereas the refractive index of the substrate is taken from literature [118].

The main assumption now is that the exciton lineshape can be modelled with a Lorentzian oscillator. Such assumption was already reported in the literature by [117, 119]. The corresponding complex dielectric function is given by the following equation, as derived in the theory chapter in section 3.3.2

$$\varepsilon_{WS_2} = \varepsilon_{\text{inf}} + \frac{I}{x_0^2 - x^2 - igx} \tag{6.3}$$

Here, x_0 is the resonance's energy, g is the linewidth, and I is the spectral weight of the resonance. Eq. 6.3 can be substituted in the Eq. 6.2 through the fundamental relation $\varepsilon = n^2$, obtaining an analytical expression of the exciton lineshape in the TC spectrum.

Before proceeding to the fit of the steady-state spectra, a discussion about the background absorption must be made. Such absorption is due to higher-lying electronic transitions. The most general approach to include this in the model is to add further Lorentzian oscillators contribution to the dielectric constant, mimicking the absorption originating from higher-lying electronic transitions. Another method is to have a phenomenological polynomial background which renders the function less computationally expensive. In the following analysis, I choose the polynomial background because it is as accurate as the approach including an extra-Lorentzian term, but much more computationally convenient. An exhaustive explanation of

the choice of the background is given in the following subsection. The analytical formula of the steady-state TC spectra becomes then:

$$TC = -Re\left[\frac{2}{1+n_{sub}}\right] Z_0\sigma^s(\varepsilon_{WS_2}) + A + B(x-x_p) + C(x-x_p)^2 \tag{6.4}$$

The fit is restricted to the energy range between 1.9 eV and 2.07 eV because this energy region encloses the excitonic response and guarantees that the polynomial can reproduce the background absorption accurately. The fit to the experimental trace with Eq. 6.4 is reported in Fig 6.17.a) with the red trace. The fit function reproduces confidently the data and the extracted parameters are $x_0 = 1.994 \pm 0.001$ eV, $g = 50 \pm 3$ meV, and $I = 1.29 \pm 0.06$. The estimation of the errors is discussed and reported in the following subsubsection because it depends drastically on the choice of the background absorption.

The excellent fit result allows us to conclude that the assumption of a Lorentzian lineshape, instead of a Voigt or a Gaussian, is a valid approximation. The other two lineshapes can be more accurate in the presence of consistent inhomogeneous broadening of the excitonic resonance, as reported in [120]. In our measurements, the inhomogeneous broadening of the excitonic resonance is minimal since the samples are obtained by mechanical exfoliation and placed on a fused silica substrate, both guaranteeing minimal impurities and few defects that can lead to inhomogeneous broadening [121, 77]. Furthermore, one single Lorentzian is needed to reproduce the exciton contribution, meaning that the influence of the many-body excitonic state (trion) [122, 123], which is generally observed in low-temperature photoluminescence experiments [124], is negligible.

From the fit parameters, the real (blue trace) and imaginary (red trace) parts of the complex refractive index are calculated by making use of the Eq. 6.3. The last two quantities are reported in Fig. 6.17.b) as a function of photon energy. These correspond only to the A exciton contribution to the refractive index and are not affected by higher-lying electronic transitions.

To summarize, I have shown how to quantitatively isolate and extract the excitonic signature in the steady-state TC spectrum in terms of exciton contribution to the complex dielectric function. This was achieved by assuming that the exciton can be described with a Lorentzian oscillator, and the TC lineshape is derived using the 2D linearized model. The complex dielectric function (refractive index) is obtained by fitting the models to the experimental data. Before proceeding further, it is necessary to discuss the choice of background and the error estimation on the parameters of the exciton.

Background modelling and error estimation

In this subsection, the fit model used for the steady-state TC was discussed. The choice of the model is fundamental for accurately modelling the exciton lineshape

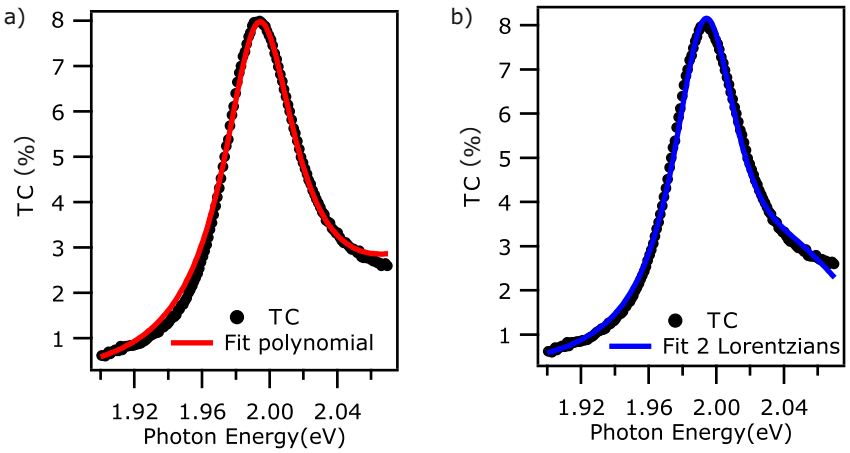

FIGURE 6.2: a) Steady state TC contrast spectra of monolayer WS_2 deposited on a thick FS substrate and best fit using Eq. 6.4. This figure is equal to Fig. 6.17.a). b) Steady state TC contrast spectra of monolayer WS_2 deposited on thick FS substrate and best fit using the two Lorentzians fit function: Eq. 6.6.

and disentangling it from the background absorption. Moreover, the comparison of the different models provides an estimation of the errors on the fit parameters.

In particular, the previous section showed how a polynomial function is used to model the background absorption. Another possible approach is to use one or more Lorentzians at higher energies to model the response of the higher-lying electronic transition. Furthermore, the choice of the background can change the parameters of the fit slightly, and this provides an estimation of the fit errors. The comparison of the two different models that can be used for the background is shown in the following, along with the discussion on their accuracy and the resulting errors on the fit parameters.

Fig. 6.2 reports the comparison between two different fits of the background absorption. The left panel shows the same figure as in Fig. 6.17 with the steady-state TC (black markers) as a function of probe photon energy and the best fit obtained with the Eq. 6.4.

In the right panel the same steady state TC (black markers) spectrum is reported. The fit function used in this case is obtained by assuming a dielectric permittivity given by the sum of two Lorentzians, given by the following equation:

$$\varepsilon'_{WS_2} = \varepsilon_{\text{inf}} + \frac{I}{x_0^2 - x^2 - igx} + \frac{I_1}{x_1^2 - x^2 - ig_1 x} \tag{6.5}$$

It is important to notice that the second Lorentzian does not have a precise physical meaning in this case, and it is simply used to model the background absorption. The resulting fit function for the steady-state TC is:

$$TC = -Re\left[\frac{2}{1+n_{sub}}\right] Z_0 \sigma^s(\varepsilon'_{WS_2}) \tag{6.6}$$

The best fit to the experimental trace is reported in Fig. 6.2 right panel, with the

solid blue trace. The fit was restricted to the same energy range, between 1.9 eV and 2.07 eV, as in the polynomial background case.

Both fit functions reproduce the measured spectrum accurately. Table 6.1 reports the parameters that best approximate the data. Despite using a polynomial to model the background is a simplification, the slight relative difference in the fit parameters with respect to the 2 Lorentzian approach justifies this model's use due to the much more convenient computational cost. The fit results are comparatively similar in terms of accuracy, and they differ relative to each other by a minimal amount, with a maximum relative error of 4% between the two cases. Thereby, the reliability of the simplified polynomial modelling of the background absorption is demonstrated.

Parameters	Polynomial fit	Two Lorentzian fit
x_0	1.9942±0.0002 eV	1.9937±0.0003 eV
g_0	50±1 meV	48±1 meV
I_0	1.29±0.02	1.23±0.04

TABLE 6.1: Fit parameters. Statistical errors corresponding to 4σ confidence interval of the fit.

The errors reported in table 6.1 correspond to the confidence interval at four sigmas from the fit. The statistical errors from the respective fits are one order of magnitude smaller than the difference between the parameters extracted from the two fits. Such error values are an underestimation, and the difference between the fit parameters due to the choice of background in the two different fits seems like a better approximation for the experimental error. The extracted parameters of the fit using the polynomial background, with the respective errors, are then: x_0=1.994±0.001 eV, g_0=50±3 meV and I_0=1.29±0.06.

After explaining why the polynomial background is a suitable approximation for reproducing the experimental data, and after having estimated the errors on the fit parameters, we now have the basis to proceed further in the discussion. The next step consists in unravelling the excitonic signature in the optical spectrum of a monolayer WS_2 placed on a more complex layered substrate.

6.1.2 Monolayer WS_2 on layered Si/SiO_2 substrate

The previous section showed how to retrieve the excitonic contribution to the complex dielectric function from the steady-state TC spectrum of a monolayer WS_2 placed on a transparent substrate and normal transmission of the probe beam. In general, the choice of the substrate can be different, with an opaque substrate or even a layered one. In the same way, the incoming probe beam can be at an arbitrary angle. All of this renders the excitonic signature in the optical spectra less trivial to analyze.

This section reports the isolation of the excitonic contribution to the complex dielectric function from the steady-state reflectance contrast (RC) spectrum of a monolayer WS_2 placed on a layered silicon/silicon oxide substrate (Si/SiO_2). In total analogy with the FS case, the exciton contribution to the dielectric function is modelled

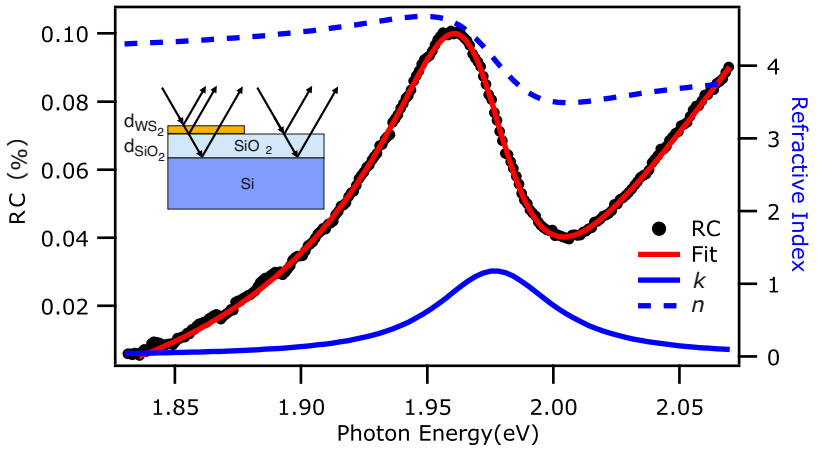

FIGURE 6.3: a) Steady-state RC spectra of monolayer WS_2 deposited on a Si/SiO_2 substrate with the best fit using Eq. 6.8. The sketch of the geometry of the sample is reported in the inset with the schematics of the multiple reflections across the interfaces of the sample and the bare substrate. Real (n) and imaginary (k) part of the refractive index calculated from best-fit parameters using Eq. 6.3.

with a Lorentz oscillator, and the corresponding lineshape is derived by using the Fresnell transfer matrix formalism. By fitting this model to the steady-state RC spectrum, the excitonic signature in the optical spectra is unveiled.

The substrate of the sample in analysis consists of a silicon wafer covered by a nominally 285 nm thick layer of SiO_2. The RC spectrum is acquired in reflection geometry due to the opacity of the Silicon substrate. The probe beam is incident at a 45° angle, guaranteeing a clear separation of the incoming and outcoming beam.

The steady-state RC spectrum is reported in Fig 6.3 with black markers. A resonant contribution is evident in the energy region between 1.95 eV and 2eV. The lineshape presents a strong asymmetry and a background absorption is also observed. From these results, it can be tempting to qualitatively interpret the peak of the resonant contribution as the absolute energy of the exciton. These data must be interpreted with caution because the observed features are characteristic of the layered nature of the substrate and require careful analysis. In particular, multiple reflections across the different interfaces can occur in such a system, as sketched in the inset of Figure 6.3. The quantitative modelling of the optical spectra requires then particular care.

To extract the analytical expression of the excitonic lineshape, it is necessary to use the Fresnel transfer matrix formalism, more specifically employing the characteristic matrix approach described in the theory chapter (section 3.2.1). For s-polarization and for an arbitrary incidence angle φ of the probe beam the characteristic matrix of a stack of different layer is given by the multiplication of the characteristic matrices of all the constituent layers :

$$\hat{\mathbf{M}}_{stack}(z) = \prod_j \hat{\mathbf{M}}_j(d_j, n_j, \psi, k_0) \tag{6.7}$$

The complete analytical formula of the characteristic matrix of a single layer constituting a stack is given by Eq. in the theory chapter. The matrix depends on the thickness of the layer d_j, ψ the angle of propagation through the media, n the complex refractive index of the material, and k_0 the wavenumber.

It is possible to calculate the reflected and transmitted fraction of the stack of layers from the characteristic matrix. The derivation of the reflected fraction from these equations can be found in the theory chapter in section (3.2.1) given by Eq. 3.35. The analytical formula of the reflectance contrast for our specific case is then obtained by calculating the reflected fraction of the WS_2 on the substrate and the reflected fraction of the bare substrate, and it is given by the following expression:

$$RC = \frac{R_{sub}(d_{SiO_2}, \varepsilon_{SiO_2}, \varepsilon_{Si}, \varphi) - R_{WS_2}(\varepsilon_{WS_2}(x_0, g, I, \varepsilon_{\text{inf}}), \varepsilon_{SiO_2}, \varepsilon_{Si}, \varphi, d_{SiO_2}, d_{WS_2})}{R_{sub}} + \\ + A + B(x - x_p) + C(x - x_p)^2 \tag{6.8}$$

The central assumption for the WS_2 is that the dielectric constant can be modelled using a Lorenz oscillator, in analogy to the case of the FS substrate, according to Eq. 6.3. Once again, a polynomial function is used to reproduce the background in the RC data to include higher-lying electronic transitions.

The analytic expression of the RC is a complicated function that depends on the thickness of the layers, d_{SiO_2}, d_{WS_2}, the incidence angle of the probe beam φ, and the complex dielectric function of the Si [118], SiO_2, and WS_2 respectively.

In total, the expression of the RC depends on nine parameters plus the four of the polynomial. To reduce the number of free parameters in the fit, the thickness of the monolayer was measured with AFM and found to be $d_{WS_2} = 0.7$ nm, and the value of ε_{inf} was fixed to the same value extracted from the FS data. The SiO_2 and Si refractive indices have been taken from literature [118, 125]. Lastly, the thickness of the SiO_2 layer and the incidence angle were independently determined by performing a global fit of multiple static spectra, returning values of $\varphi = 0.77 \pm 0.01$ rad and $d_{SiO_2} = 305 \pm 20$ nm. The only free parameters are then the parameters of the excitonic resonance (x_0, g, I) and the four of the polynomial. Once again, the fit is restricted to the energy range between 1.9 eV and 2.07 eV because this energy region encloses the excitonic response and guarantees that the polynomial can reproduce the background absorption accurately.

The best fit to the steady-state RC spectrum is reported in Fig. 6.3 with the red line. It is clear that the fit reproduces the experimental curve accurately. The extracted parameters for the exciton resonance are $x_0 = 1.973 \pm 0.001$ eV, $g = 54 \pm 2$ meV and $I = 1.05 \pm 0.06$. The errors are estimated using the same considerations and discussion reported in section 6.1.1 in the FS case.

As in the case of the transparent substrate, one single Lorentzian accurately reproduces the spectrum, confirming that the Lorentz model is a good approximation for the excitonic resonance. The background is due partially to the higher-lying

electronic transitions and mainly to the interference effects arising from the layered nature of the sample. Furthermore, the asymmetry of the excitonic resonance is primarily due to the interference of the multiple reflections. The reflections across the interfaces, in fact, provoke the mixing of the real and imaginary parts of the refractive index of the WS_2. This mixing is apparent when superimposing the real (solid blue line) and imaginary part (blue dashed line) of the refractive index, calculated using Eq. 6.3, to the experimental data, as shown in Fig. 6.3. It is evident that the peak in the imaginary part of the refractive index is not at the same energy at which the peak of the RC spectrum is. The RC lineshape derives from the mixing of the real and imaginary parts of the refractive index. Therefore, the tempting interpretation of considering the RC peak energy as the exciton resonance energy is misleading, and this discrepancy must be considered when analyzing optical spectra of WS_2 placed on layered substrates.

With this formalism, it is possible to accurately extract the excitonic contribution to the complex dielectric function from the steady-state RC spectrum of a monolayer WS_2 placed on a layered Si/SiO_2 substrate. Turning now to the comparison of the exciton parameters between the two different samples analyzed in the previous sections. Before making the comparison, the extraction of the exciton dynamic response upon photoexcitation is presented in the following section, and the comparison is postponed to the discussion section 6.1.4.

6.1.3 Evolution of complex dielectric function after photoexcitation

In the previous section, it was shown how to analytically describe the exciton lineshape in the steady-state optical spectra of different samples, substrates and from two different measurement techniques. In particular, by assuming that the exciton can be described with a Lorentzian oscillator, it is possible to extract the exciton contribution to the complex dielectric function by using either the 2D linearized model or the Fresnel transfer matrix formalism. As already mentioned in the theory chapter 2.2.2, the exciton response can generally change upon optical excitation due to different phenomena. Peak shift, broadening, or intensity changes can occur, and it is therefore fundamental to quantitatively track the time evolution of the exciton at every time stage after photoexcitation. It becomes therefore fundamental to track the dielectric function dynamics upon photoexcitation to provide a quantitative description of the time-dependent excitonic response.

To do that, I extend the 2D linearized model and the Fresnel transfer matrix model to describe the time-dependent exciton response upon photoexcitation. By fitting the two aforementioned models to the tr-TC and tr-RC spectra of the monolayer WS_2 on the respective substrates, the exciton resonance energy, linewidth and spectral weight as a function of time are extracted.

The accurate determination of the excitation conditions is fundamental for a proper understanding of the exciton dynamics. In the following experiments, the

WS_2 is photoexcited with a pump pulse tuned to 1.99 eV, in resonance with the excitonic absorption peak. The initial photoexcited particle density is 3.1 10^{+12} cm^{-2}. This quantity is essential for a proper interpretation of the observed dynamics. Such quantity, with respect to the fluence, offers a more exact determination of the initial excitation condition because it is retrieved from the actual effective absorbance of the sample, which is known to change quite drastically depending on the sample or substrate, as described in the theory chapter in section 2.2.1. The effective absorbance can be calculated starting from the exciton complex dielectric function retrieved from the fit of the steady-state spectra, and it is then compared to the pump lineshape to obtain the photoexcited quasi-particle density. The details of these calculations are quite involved. Therefore, for the flow of this work, the details of such calculation are reported in appendix B.

The time-dependent TC of the monolayer WS_2 is reported in Fig. 6.4.a) in false colour plot as a function of the probe photon energy (x-axis) and pump-probe delay (y-axis). The measurement shows explicit dynamics after time zero in the energy range of the exciton. Peak shift and broadening occur, accompanied by a reduction of the maximum intensity of the resonance. These dynamics are evident in Fig. 6.4.b) where spectra for three selected time delays are reported as a function of probe photon energy. In particular, a blueshift of the resonance is observed for early time delays. Photoinduced broadening is also present, and a reduction of the intensity maximum is also evident. Notably, these last two effects are complicated to disentangle qualitatively, so a quantitative analysis is necessary.

To precisely quantify the time evolution of the excitonic resonance, a fit to the time-resolved spectra with Eq. 6.4 is performed. The assumption of low contrast TC$\ll$ 1 is satisfied across the whole delay range. Here, I assume that the background absorption does not change upon photoexcitation. Therefore the parameters of the polynomial background are kept fixed to the value retrieved from the fit of the steady-state spectrum. The best fits of three selected delays are reported in Fig. 6.4.b). It is evident that the fits reproduce the exciton lineshape accurately for the different delays. The exact fit was performed for every spectrum at every time delay, extracting the exciton peak position, linewidth, and spectral weight of the excitonic resonance. The extracted peak position (red trace) and linewidth (distance between black traces) are reported in Fig. 6.4.a) overlaid on the same axis as the tr-TC. The spectral weight of the resonance does not change within the noise level of our measurements, as shown in Fig. 6.5.b).

To confirm the quality of the model employed, the χ^2 of the fit as a function of time delay is shown in blue in Fig. 6.4.c). The absolute value of the χ^2 on the order of 10^{-4} confirms the fit quality across the whole range of delays.

This analysis method allows the extraction and quantification of the time evolution of the complex dielectric function of the exciton in the case of a monolayer WS_2 placed on a thick FS substrate. Having extracted the exciton dynamics upon photoexcitation from the tr-TC experiment, It is now possible to proceed to the more

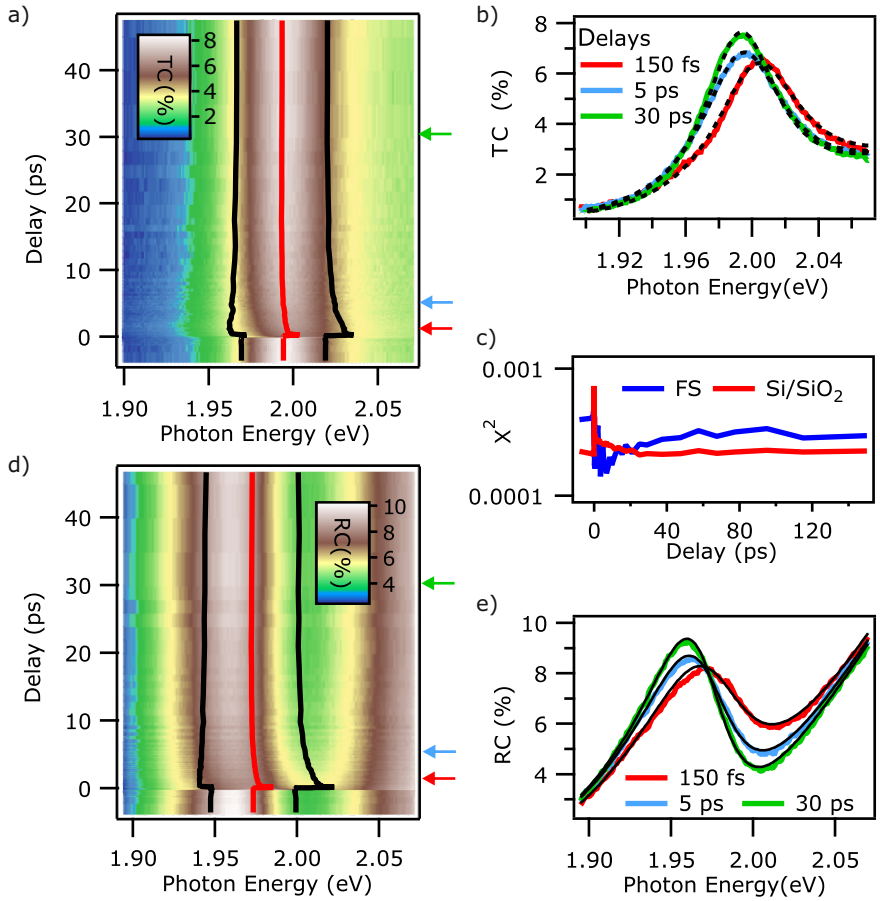

FIGURE 6.4: a) False color plot of the tr-TC as a function of probe photon energy (x-axis) and the pump-probe delay (y-axis). Exciton peak position (red trace) and linewidth (distance between black traces) from fitting the time-dependent TC with Eq. 6.4 overlaid on the same axis. b) TC spectra for three selected delays and respective fits with Eq. 6.4. c) Time-dependent χ^2 of the fits of tr-TC and tr-RC data, respectively, as a function of time delay. d) False color plot of the tr-RC as a function of probe photon energy (x-axis) and the pump-probe delay (y-axis). Exciton peak position (red trace) and linewidth (distance between black traces) from fitting the time-dependent RC with Eq. 6.8 overlaid on the same axis. e) RC spectra for three selected delays and respective fits with Eq. 6.8.

complicated case of the tr-RC of the monolayer placed on the Si/SiO_2 substrate.

For the case of the tr-RC, the procedure is analogous to the approach just described. The tr-RC (false colour) as a function of probe photon energy (x-axis) and time delay (y-axis) is shown in Fig. 6.4.d). Clear dynamics are present in the proximity of the exciton energy. As already seen in the previous section 6.1.2, the exciton lineshape in the RC spectra is more complex with respect to the steady-state TC spectrum of the monolayer placed on a FS substrate. The more complex lineshape also remains in the dynamical response of the system upon photoexcitation. In Fig 6.4.e), the RC spectra for a few selected delays (legend) are shown as a function of probe photon energy. Blueshift of the exciton is observed upon photoexcitation, and it is accompanied by a broadening of the resonance, but the distinction between the two effects is not trivial. To overcome this, to quantitatively extract the parameters of the excitonic resonance, the transfer matrix approach used for the steady-state RC spectrum is employed. Analogous to the FS case, I assume that the polynomial background absorption does not change upon photoexcitation.

The fit using Eq. 6.8 to the time-dependent RC spectra upon photoexcitation is reported in Fig. 6.4.e) with the black traces. Once again, the fit quality is evident, supporting the appropriateness of the model employed to reproduce the excitonic lineshape also for its dynamic response. By performing the fit to every spectrum for each time delay, the time-dependent peak position (red trace) and linewidth (distance between black traces) are extracted and displayed as a function of time delay in Fig. 6.4.d), overlaid on the same axis as the tr-RC.

The reliability and accuracy of this model are comparable to the one employed for the tr-TC experiment on the FS sample. In fact, the χ^2 of the fit as a function of time delay, shown with the red trace in Fig. 6.4.c), is on the same order of magnitude as for the FS case, and it does not vary drastically as a function of time delay. This analysis method guarantees the accurate extraction of the dynamics of the exciton contribution to the complex dielectric function dynamics in the tr-RC measurements of a monolayer placed on the Si/SiO_2 substrate.

In summary, these methods allow the extraction of the time-dependent evolution of the exciton quantitatively for two different experiments, samples and substrate. The dynamics of the complex dielectric function upon photoexcitation are unravelled by combining the Lorenz model to trace the exciton contribution to the dielectric function with either the 2D linearized model or the transfer matrix method. The exciton evolution upon photoexcitation is then described by the exciton peak position, the linewidth and the spectral weight as a function of pump-probe delay. Having unravelled the exact same physical quantities from the two measurements, it is now possible to compare the extracted dynamics.

The analysis of the exciton static and dynamic response, extracted from the two independent experiments, is made in the following section, where the two samples' steady-state and dynamic responses are compared and discussed.

6.1.4 Discussion and conclusion

The static and dynamic response of TMDCs monolayer can vary quite drastically, depending on sample, substrate, and excitation condition. On top of the intrinsic differences in the materials under study, the comparison between different experiments is challenging due to the various analysis methods that can be employed to extract and analyze the exciton contribution to the optical spectra. In the previous sections, two formalisms to extract the exciton dynamics from two different measurements techniques, different samples and different substrates. It is now possible to compare the steady-state and dynamic exciton response obtained in the two cases.

This section summarises the results of the analysis methods used to extract the photoinduced dynamics of the complex dielectric function of a monolayer WS_2 deposited on two different substrates, fused silica and a layered Si/SiO_2 substrate, respectively. By comparing the static and dynamic exciton responses from the two analysis methods employed, it is possible to prove the quality and reliability of the models. Furthermore, the physical insights that originate from comparing the two independent measurements are discussed in the following. In particular, a coincident dynamical response of the exciton in the two independent time-resolved measurements upon the same excitation conditions was observed, thereby confirming the robustness of the analysis methods employed and demonstrating that results from different studies can be compared within the accuracy of the excitation density determination. Furthermore, these results suggest that the exciton dynamic response is independent of the dielectric environment but depends only on the excitation conditions, therefore, the initial excitation density.

Fig. 6.5.a) reports the imaginary part of the refractive index as a function of the photon energy, computed for the sample deposited on the FS substrate (blue) and Si/SiO_2 (red trace) from the parameters extracted from the fit of the steady-state spectra of section 6.1.1 and 6.1.2. The imaginary part of the refractive index is proportional to the absorbance of the sample, and the mismatch between the two excitonic resonances is evident. When confronting the extracted parameters from the fit of the steady-state TC (RC) spectra of the monolayer deposited on FS (Si/SiO_2) substrate is evident that these are not the same, as reported in Table 6.2. It is clear that

Parameters	**Fused silica**	**Si/SiO$_2$**
x_0	1.994±0.001 eV	1.973±0.001 eV
g_0	50±2 meV	54±2 meV
I_0	1.29±0.06	1.05±0.06

TABLE 6.2: Parameters of excitonic resonance of a monolayer WS_2 placed on FS and Si/SiO_2 substrates
Fit parameters for excitonic resonance from steady state TC and RC experiments on FS and Si/SiO_2 substrate, respectively.

the absolute exciton energy x_0 is different in the two cases, the linewidth is confident in the two experiments but at the limit of the confidence interval, and the spectral

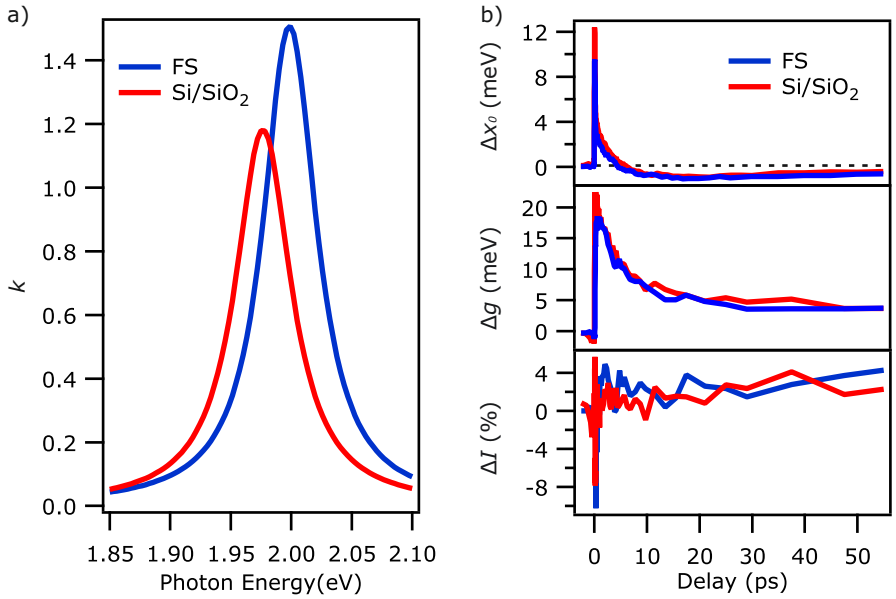

FIGURE 6.5: a) Calculated imaginary part of the refractive index from best-fit parameters of steady state spectra of WS_2 on FS and Si/SiO_2 substrates, respectively. b) Time-dependent peak shift (Δx), photoinduced broadening (Δg), and spectral weight variation (ΔI) extracted from the fit of the tr-TC of a monolayer WS_2 on the FS substrate and on from tr-RC of the monolayer on the Si/SiO_2 substrate.

weight are again different in the two experiments. This mismatch comes quite unexpectedly. In fact, in our two measurements, the dielectric environment, therefore the screening, is similar because the monolayer is in both samples in contact only with the SiO_2 substrate. This is obvious for the case of FS since SiO_2 is the only material constituting the substrate, but it is not trivial for the Si/SiO_2 substrate. In the second case, It is now natural to assume that the dielectric screening originates only from the thin layer of SiO_2 because its thickness is much larger than the typical Bohr radius of an exciton (1nm [6]). Therefore, the electric field lines between the electron and the hole constituting the exciton penetrate only the SiO_2 layer. Such observation would imply that the dielectric environment is equal in the two samples, thus suggesting the same steady-state excitonic resonance.

There are now two possible scenarios, the first one which implies that the analysis method used is wrong or that the excitonic response in the two samples is actually different. To prove this, the dynamic response of the two experiments is compared directly. At this point, if the analysis method used to extract the exciton dielectric function is not accurate, likely the dynamical response would not be the same in the two experiments

Fig. 6.5.b) compares the time-dependent relative exciton peak shift $\Delta x = x_0(t) - x_0(eq)$ (top), Fig. 6.5.c) the photoinduced broadening $\Delta g = g(t) - g(eq)$ (bottom), and Fig. 6.5.d) the spectral weight variation $\Delta I = I(t) - I(eq)$ for the monolayer on the FS substrate (blue) and Si/SiO_2 substrate (red). $x_0(eq)$, $g(eq)$, and $I(eq)$ are the

exciton energy, linewidth and spectral weight at equilibrium. In the case of the photoinduced dynamics, surprisingly, the three graphs show that the respective traces remarkably coincide across the whole delay range. Upon photoexcitation, the exciton resonance blueshifts and broadens with respect to the steady-state spectrum. Both effects then relax within a few ps, and the peak shift turns into a red-shift with a decay time on the order of tens of ps. The spectral weight does not show clear dynamics within the noise level of our experiments.

The perfect agreement of the dynamics in the case of the two samples is surprising. As seen previously, no explicit agreement in the case of steady-state excitonic absorption was observed. This suggests that the models employed to extract the exciton contribution to the dielectric function are accurate. This assumption originates from the fact that, despite both the tr-TC and the tr-RC experiment probing the non-equilibrium dynamics of the exciton in WS_2, the two extracted dynamics are retrieved from different measurement techniques, analysis methods, samples, and substrates. Therefore, I assume that the coincidence of the non-equilibrium dynamics is not accidental, but the same photoexcitation conditions cause the same photoinduced dynamics.

The discrepancy in the absolute energy of the steady-state exciton absorption is not due then to an inaccurate analysis method, but it arises from local variations of the dielectric environment due to slightly different distances between the monolayer WS_2 from the substrate or to the presence of absorbates and impurities [76] and their resulting impact on the dielectric screening from the substrate [78], as described in the theory chapter 3.2.1. This suggests that both the 2D linearized model and the Fresnel transfer matrix formalism are accurate analysis methods to track the exciton time evolution upon photoexcitation.

After having established the accuracy of the formalism to extract the dynamic of the complex dielectric function upon photoexcitation, It is possible to conclude that local differences in the dielectric environment induce bandgap and binding energy variations, thus leading to slightly different steady-state absolute exciton energy, broadening, and spectral weight. It is therefore not correct to assume the same dielectric environment between the two different samples. Slight differences in the dielectric environment substantially impact the steady-state absorption but do not contribute to the dynamic response. The latter seems to depend on the excitation conditions and, in particular, on the excited quasi-particle density. Therefore, the overlapping extracted exciton dynamics upon photoexcitation in the two experiments confirm that the two formalisms employed guarantee the basis to compare quantitatively the excitonic response of monolayer WS_2 from different samples, placed on different substrates and optical measurements techniques. Slight differences in the static screening of the Coulomb interaction lead to the mismatching exciton steady-state absorption, but this does not influence its dynamic response, mainly depending on the excitation conditions.

The results presented in this section pave the way for the reliable comparison

between independent studies of excitonic properties of monolayer TMDC within the accuracy of the photoexcitation density determination.

6.1.5 Summary and outlook

This section presented the investigation of the steady-state and time-resolved TC and RC of monolayers WS_2 placed on two different substrates (FS and Si/SiO_2). The exciton contribution to the dielectric function was isolated from the steady-state optical spectra. The central assumption was assuming that the exciton response could be modelled with a Lorentz oscillator. I then derived the analytical expression for the exciton lineshape in the optical spectra by combining the Lorentz model with the 2D linearized model or the Fresnel transfer matrix formalism. These functions were used to fit the experimental data, thus accessing the steady-state exciton contribution to the complex dielectric function of the monolayer WS_2. By fitting the models previously introduced to the time-resolved TC and RC spectra, the time evolution of the exciton upon photoexcitation was extracted, revealing the time-dependent change of the complex dielectric function upon photoexcitation. By comparing the extracted time-dependent response of the exciton upon photoexcitation for the two different samples, a remarkable agreement between the extracted dynamics for the same excitation conditions was found, therefore proving the reliability of the analysis methods used independently of the sample, measurements technique, and substrate. These findings serve as the foundation for the following experiments reported in this thesis and, more generally, for the reliable comparison between time-resolved experiments addressing exciton dynamics in TMDCs.

The results and the discussion presented in the subsection 6.1.4 indicate that the dielectric environment influences the steady-state excitonic properties. Instead, the photoinduced non-equilibrium dynamics are independent of the substrate of choice but are sensitive mainly to the excitation condition, therefore, to the excited quasiparticle population. The implication of the latter conclusion is analyzed and discussed systematically in the next section.

6.2 Quasi-particle dynamic screening

The previous section provided a formalism that allows the quantitative analysis of the steady-state and dynamical exciton response in a WS_2 monolayer independently of the measurement technique, sample, and substrate of choice. The main conclusion was that the dielectric environment influences the steady-state absorption spectra but not the time-dependent exciton dynamics upon photoexcitation. The latter seems to depend mainly on the excitation conditions, particularly on the initial photoexcited particle density. This last conclusion suggests that the dynamic screening due to the presence of quasiparticles could be the main responsible for the observed dynamics. However, confirming this hypothesis is not trivial and opens an entirely new set of questions that are discussed in this section. The main questions that this section aims to answer are: is the dynamic screening the main phenomenon that contributes to the exciton dynamic response? How does it compete with other eventual phenomena? How do different photo-excited quasiparticles influence the exciton dynamics, and which relaxation mechanisms are involved after photoexcitation? This question will be answered by investigating the pump energy and fluence dependent tr-RC of a monolayer WS_2 placed on a Si/SiO_2 substrate.

Firstly, I perform a qualitative experiment that I will carry on for the whole section as a guideline. In particular, the experiment compares the time-dependent exciton response for resonant and above-resonance optical pumping with the same initial photo-excited particle density. Excitons or quasi-free carriers (QFC) are selectively generated in the system by photo-exciting resonantly and above the WS_2 monolayer excitonic resonance, finding a similar response in the two cases other than in the first picosecond after photoexcitation. The different responses are attributed to the screening due to the transient presence of QFC in the above-resonance pumping with respect to the resonant pumping, where only photoexcited excitons are present.

In order to quantify the contribution to the time-dependent exciton response originating from the dynamic screening due to the presence of excitons in the system upon resonant photoexcitation, I use the following approach. Subsection 6.2.2 develops a phenomenological model describing the microscopic time evolution of the photo-excited quasiparticle populations, which are then related to the optical observables in analysis. I show that this simplified phenomenological model describes the pump fluence dependent dynamics of the exciton resonance for resonant pumping. From this, the effects arising from the dynamic screening of the excitons transiently present in the system and the thermal contributions to the exciton dynamics are isolated. In particular, the dynamic screening of the exciton is the main responsible for the observed blue-shift, which can be modelled with an effective binding energy reduction. This blueshift competes with thermal effects which become the dominant contribution to the red-shift at later time delays. Furthermore, the exc-exc scattering is the primary source of broadening.

After that, subsection 6.2.3 discusses the effects due to the presence of QFC in the above-resonance pumping case, described by extending the phenomenological model used for the resonant pumping case. The different screening of the Coulomb interaction from the presence of QFC explains the different exciton peak shifts,modelled with an effective bandgap renormalization, and the QFC-exc scattering is the main responsible for the extra linewidth broadening mechanism. Ultimately, this section elucidates the complex phenomena and recovery pathways that govern the system's recovery back to the equilibrium, providing the timescales of the multiple relaxation channels of the different photo-excited quasiparticle species. The proposed model unravels the interplay between electronic and thermal processes contributing to the exciton non-equilibrium response. In particular, the influence of exciton and quasi-free carriers (QFC) screening on the non-equilibrium dynamics of the exciton resonance are isolated. The main finding is that QFC induce broadening of the exciton through QFC-exc scattering and, through dynamic screening, induce a red-shift of the resonance modelled with an effective bandgap renormalization. Excitons, instead, induce a blue-shift which can be reproduced with an effective binding energy reduction. The broadening of the exciton resonance, when excitons are present in the system, originates mainly from exc-exc scattering. Finally, the different dynamic screening originating from QFC or exciton is discussed, finding that, per unit of quasiparticle, exciton induce a stronger blue-shift of the resonance with respect to the QFC induced red-shift.

This section is mainly based on my work reported on arxiv [126]

6.2.1 Exciton vs quasi free carriers dynamic screening

Quasiparticle-induced dynamic screening can change the excitonic properties of monolayers TMDC, as discussed in the first chapter, section 2.2.2, and in the chapter 5. Generally, when a monolayer WS_2 is pumped with an optical pulse, a specific density of quasiparticles is generated in the system. However, it is not clear if these quasiparticles are excitons or quasi-free carriers, and it mainly depends on the excitation condition. Furthermore, the effects due to the presence of one or either quasiparticle are not quantitatively understood yet.

In this subsection, I report a qualitative experiment in which i compare the above-resonance and resonant pumping exciton dynamic response, extracted using the formalism presented in section 6.1.2, of a monolayer WS_2 placed on a Si/SiO_2 substrate. A pump energy-dependent red/blue-shift of the excitonic resonance for early time delays upon photoexcitation is observed. Furthermore, a stronger linewidth broadening is present in the case of above-resonance pumping. After discussing it, the dissimilar dynamics are qualitatively attributed to the presence of excitons or quasi-free carriers in the resonant above-resonance experiments, respectively.

The sample in analysis is a monolayer WS_2 placed on a Si/SiO_2 substrate investigated in the previous section. A resonant pumping tr-RC experiment is performed by tuning the pump photon energy resonantly with the A exciton at 1.99

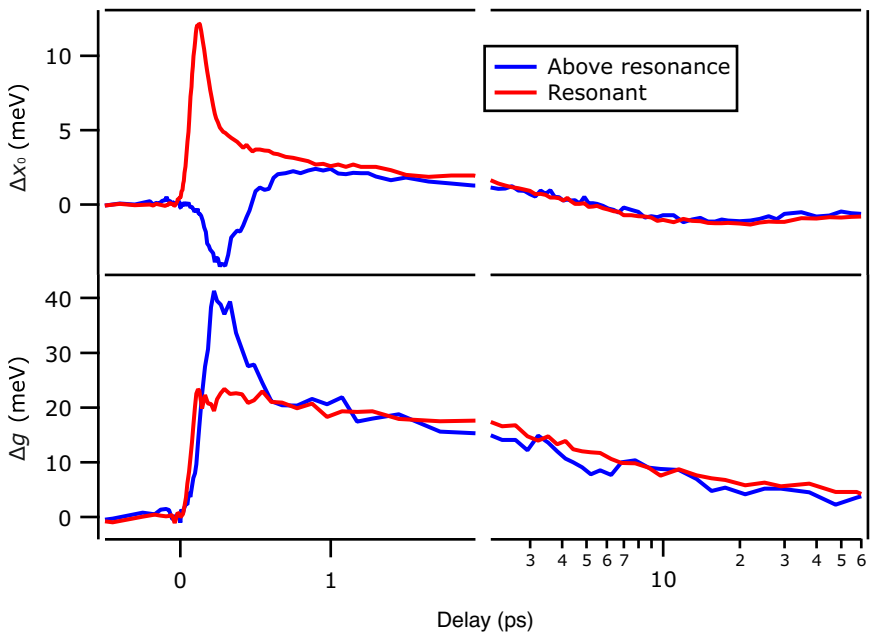

FIGURE 6.6: Exciton peak shift and broadening as a function of time delay for resonant (red) and above-resonance (blue) pumping.

eV. The same experiment is then carried out, but tuning the pump photon energy at 3.1 eV, well above the quasi-free particle bandgap. The initial photoexcitation density in the two experiments is the same, with a value of n_0=3.1 10^{12} cm^{-}2. The details of the calculation of the last quantity are reported in Appendix B. The time-dependent exciton peak shift and linewidth broadening as a function of the delay are extracted using the approach described in sections 6.1.3. Fig. 6.6 compares the time-dependent exciton peak shift $\Delta x = x_0(t) - x_0(eq)$ (top) and the photoinduced broadening $\Delta g = g(t) - g(eq)$ (bottom), extracted from a resonant /above resonant pumping tr-RC experiments on a monolayer WS_2 placed on a Si/SiO_2 substrate. Here, $x_0(eq)$, $g(eq)$, and are the exciton energy and linewidth at equilibrium, extracted by the fit of the negative time delay spectra.

The exciton dynamics are similar in the two experiments except for the early time delays. Upon photoexcitation, the exciton resonance displays a selective blue/red-shift for resonant/above-resonance excitation conditions. In the case of the above-resonance pumping, the red-shift turns into a blue-shift within the first picosecond roughly. From this stage, the exciton peak shift evolves similarly in the two cases. In particular, the blue-shift reduces, eventually turning into a red-shift for later time delays. The slight red-shift then recovers within a hundred picoseconds. The linewidth broadening is stronger in the case of the above-resonance pumping, persisting only for a few hundred femtoseconds. After the early stage different dynamics, the broadening seems to be equal in the two experiments, eventually recovering on the timescale of a few tenths of picoseconds. Finally, no spectral weight changes were observed upon photoexcitation.

I discuss now a qualitative interpretation of this experiment. The quantitative details of this experiment will be added bit by bit throughout the section. In order to explain the observed dynamics, It is first necessary to consider the difference between the two experiments. In the case of resonant pumping, the pump photon energy can photoexcite electrons only to the excitonic state because the pump photon energy is well below the quasi-free particle bandgap. In the case of the above-resonance, the photon energy is substantially higher than the quasi-free particle bandgap. Therefore QFC can be injected into the system. Qualitatively, the most viable hypothesis is that only excitons are photoexcited in the system in the case of resonant pumping. Instead, in the case of the above-resonance pumping, QFC are optically injected through the absorption of the pump, consistently with [90].

The difference in the dynamics observed in Fig. 6.6 persists only for a few hundreds of fs, suggesting the electronic origin of this difference. In fact, hot QFC undergo fast relaxation, in the order of the hundreds of fs in conventional semiconductors [127], forming excitons. Once the QFC thermalize into excitons, the above resonant and resonant pumping case would behave similarly in the first approximation. Therefore, it is possible to conclude that the different dynamics originate from the presence of QFC in the above resonant pumping case and, in particular, from the different dynamic screening of QFC or excitons. It is known from the theory chapter that the quasiparticle-induced dynamic screening induces binding energy reduction and bandgap renormalization, as discussed in section 2.2.2. From this experiment, it is evinced that when QFC are present in the system, the bandgap renormalization dominates the binding energy reduction. Vice versa, binding energy reduction is the stronger effect when excitons are transiently present in the system.

It is possible, therefore, to conclude that the different exciton dynamic response observed in the above-resonance/resonant pumping is due to the presence of QFC or exciton, respectively. This is a qualitative argument that needs to be tested and made quantitative. To do that, the process is quite involved, and it will be treated in the following. I first isolate the role of the exciton in the dynamic response by investigating the fluence dependent resonant pumping tr-RC experiment on a monolayer WS_2.

6.2.2 Exciton dynamic screening

In the conclusion of the previous section, it was hypothesized that the exciton dynamic response is governed by the dynamic screening of the quasiparticle transiently present in the system. In order to test this hypothesis and unravel how these quasiparticles influence the peak shift and broadening, I ask the question: what is the role of the exciton-induced dynamic screening?

This subsection investigates the role of the exciton-induced dynamic screening by investigating the fluence dependence of the exciton peak shift and linewidth

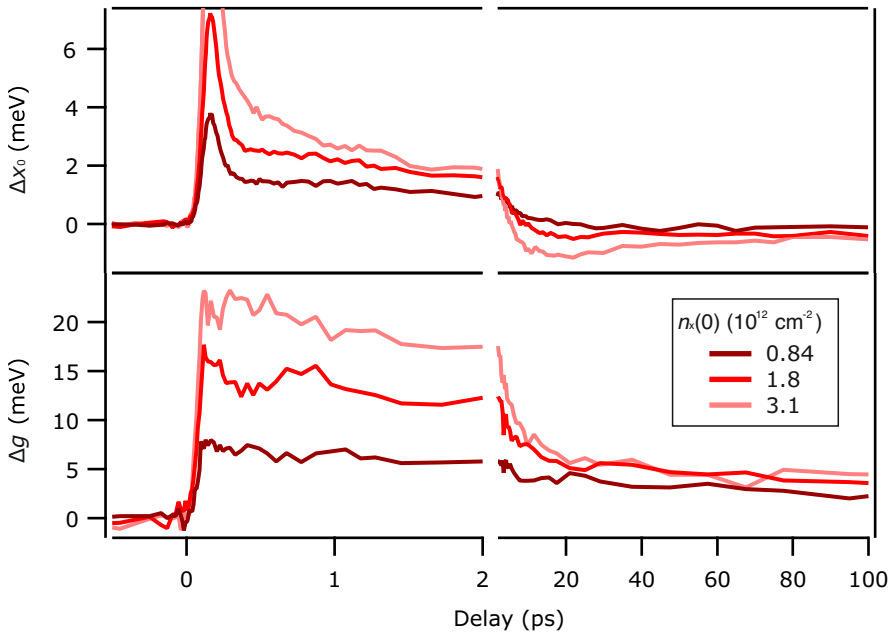

FIGURE 6.7: Exciton peak shift and linewidth broadening as a function of time delay for different fluence of resonant pumping.

broadening extracted from the resonant pumping tr-RC experiments on a WS_2 sample. I then propose a microscopic phenomenological model to describe the time evolution of the exciton population density transiently present in the system and the lattice temperature, finally relating these quantities to the optical observable. By fitting this model to the fluence dependence of the exciton peak shift and linewidth broadening, an excellent agreement of the model with the experimental traces is found. The agreement of the data and the model, supported by extracted parameters confident with previously reported literature values, proves that the founding assumptions of the two-level model are accurate.Thus, it is concluded that the dynamic screening due to the presence of excitons is the main cause of peak shift. In particular, the blue-shift is modelled with an effective binding energy reduction, and the linewidth broadening originates from exciton-exciton scattering. After this, the reliability of this phenomenological model to describe the basic phenomena governing the photo-response of the exciton in monolayer WS_2 is confirmed for a monolayer WS_2 placed on a FS substrate and form tr-TC measurement. Finally, the interplay of electronic and thermal processes governing the exciton response upon resonant pumping are isolated and discussed.

Fig. 6.7 shows the extracted exciton peak shift Δx_0 and linewidth broadening Δg as a function of time delay for different fluences for the resonant pumping experiment on a Si/SiO_2 substrate. The excitation conditions are analogous to the resonant pumping experiment described in the previous section, and the initial photoexcitation density is calculated as described in Appendix B. The exciton resonance

shows an instantaneous strong blue-shift, which partially recovers within the cross-correlation of the pump and the probe pulses. After the cross-correlation of the two pulses, the blue-shift is still present and gradually diminishes, eventually turning into a red-shift for the data with higher excitation density. The crossover to the red-shift happens the sooner, the higher the fluence. The red-shift then recovers on the order of the tenths of picosecond timescale. The linewidth of the resonance instead shows an instantaneous broadening after the pump pulse, and it recovers gradually after a few tenths of ps. The recovery appears to be quicker for higher initial photoexcitation density. The spectral weight does not change within the noise level of our experiment, confidently to the experiment reported in the previous section 6.1. All these trends are stable upon different fluence.

In the attempt to describe the observed dynamics of the excitonic resonance, I proceed as follows. The initial short-lived blue-shift is attributed to resonant effects. It was shown in the literature that when the pump and probe are resonant with each other, coherent effects, such as Stark shift [128, 129], can occur. Due to the complexity of the phenomena occurring within the cross-correlation of the pump and the probe, our analysis excludes this specific time range. It is now convenient to assume that, upon resonant photoexcitation, only excitons are photogenerated in the system because the photon energy of the pump is smaller than the quasi-free particle bandgap, thus can not photoexcite QFC [90]. After the cross-correlation, when the coherences between quasiparticles are dephased, an incoherent exciton population $n_x(o)$ is present after 150 fs upon photoexcitation [130, 131, 34]. The quantitative analysis of the dynamics from this point is quite involved. The blue-shift generally is attributed to a more pronounced binding energy reduction with respect to the bandgap renormalization or to phase-space filling effects, as seen in [32, 30] and in Chapter 5. Phase-space filling (PSF) effects can be excluded as a blue-shift mechanism due to the resonant photoexcitation of only excitons and because this would imply a reduction of the spectral weight of the resonance. This effect was commonly observed in MoS_2 samples [34, 132], and not in W based TMDC [133, 26], as the origin of the blueshift. Neglecting PSF is further confirmed valid because phase-space filling effects, due to the Pauli exclusion principle, would imply a reduction of the oscillator strength of the excitonic resonance, which is not observed. The only mechanism remaining available for the blue-shift corresponds to the dynamic screening of the exciton, which could induce BER and BGR, with the first effect being the dominant one. The other remaining cause of the observed dynamic, corresponding to thermal effects, needs to be also included in the analysis as shown in the following.

So far, I qualitatively investigated the time-dependent exciton evolution upon photoexcitation by investigating the exciton peak shift and linewidth broadening as a function of time. The coherent phenomena happening during the cross-correlation were excluded from our analysis, concluding that an incoherent initial photoexcited exciton density n_0 is present in the system 150fs after time zero. Phase-space filling effects were also excluded as a cause of dynamics. Therefore, the time-dependent

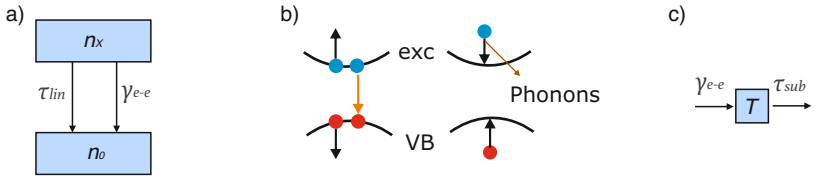

FIGURE 6.8: a). Sketch of phenomenological 2-level model. b) Sketch of Auger recombination-induced thermalization. c) Sketch of temperature model

evolution of the exciton peak shift seems to be originating from the competition of exciton dynamic screening and thermal effects. A quantitative modelling of this is presented in detail in the following sections. From this point, I now investigate the time evolution of the exciton density in the system, eventually proposing a phenomenological model for it.

Microscopic two-level model and thermal dynamics

Generally, when a non-equilibrium population of carriers is photoexcited in semiconductors, they undergo recombinations, driving the system back to equilibrium. The recombination of these carriers can be described with rate equations analogously to the case of the Einstein coefficient for the two-energy level system described in section 3.3. The rate equations governing the system's recovery might not be as simple as the case described in the theory chapter, as different recombination channels might be present and can compete with each other.

In the attempt to model the complex exciton dynamic response upon photoexcitation, this section proposes an essential microscopic phenomenological two-level model to reproduce the time evolution of the exciton density in a resonant pumping case. Two recombination channels, a linear and a quadratic one, are included, and the excited exciton density's time evolution is retrieved. The inclusion of a quadratic Auger recombination channel implies an energy transfer from the electronic system to thermal energy. The mechanisms and the modelling of the two are then reported, ultimately deriving an analytical formula for the time-dependent exciton density and local lattice temperature of the WS_2 monolayer.

It is now convenient to introduce a model for the time-dependent exciton density consisting of a simplified two-level system as sketched in the inset of Fig. 6.8.a). The lower state n_0 corresponds to the ground state, and the higher level n_x corresponds to the exciton level. As discussed in the previous section, the pump pulse generates an initial photoexcited exciton density $n_x(0)$ in the higher level.

The relaxation of these excitons to the ground state n_0 occurs through two channels. The first one is a linear recombination channel (with rate $1/\tau_{lin}$), analogously to the derivation of section 3.3.1. The second term is attributed to Auger recombination, corresponding to the non-radiative recombination of one exciton following

a scattering event, which transfers energy to other excitons, as sketched in Fig. 6.8. Such recombination channel was already reported in literature [134, 32, 135] and is described by a quadratic term in the exciton density, multiplied by the rate γ_{e-e}. Writing the rate equation governing time evolution of the exciton population density in the n_x state leads to the following expression:

$$\frac{dn_x}{dt} = -\frac{1}{\tau_{lin}} n_x - \gamma_{e-e} n_x^2 \tag{6.9}$$

Solving this differential equation for the given initial photo-excited particle density n_0 provides an analytical formula for the time evolution of the excitonic population. For the sake of the flow of this work, i report the analytical expression of the time-dependent exciton density $n_x(t)$ in appendix A. Other important aspects to consider when non-radiative transitions are observed in the system are the thermal effects arising from the energy conservation principle. In fact, when Auger recombination occurs in a material, it is crucial to evaluate the energy transfer from the electronic system to thermal energy. In fact, In their work, Ruppert et al. [32] reported that the non-radiative recombination of exciton through Auger scattering leads to the energy transfer from the electronic system to the phonon system and ultimately increases the lattice temperature. This temperature increase is fundamental to model the exciton dynamic response since it was shown in the theory chapter (c.f section 2.1.4) that the excitonic resonance shifts and broadens with varying temperatures.

This mechanism of energy transfer from the electronic system to thermal energy is sketched in Fig. 6.8.b). When an exciton recombines non radiatively, the energy is transferred to other excitons, bringing them to an excited state. The excited exciton then relaxes through the emission of phonons, which ultimately increases the lattice's temperature. To calculate the temperature increase due to exciton Auger recombination, it is assumed, in first approximation, that the rate of increase of the WS_2 lattice temperature corresponds to the rate of exciton Auger recombination γ_{e-e}. The monolayer, which becomes hotter than the surrounding, will then transfer thermal energy to the substrate with a rate $1/\tau_{sub}$. This is summarized in the sketch in Fig 6.8. The lattice temperature variation $T(t)$ can be described by the following rate equation:

$$\frac{dT(t)}{dt} = +\gamma_{e-e} n_x^2 \frac{h\nu_x}{\rho c_p d} - \frac{1}{\tau_{sub}} T \tag{6.10}$$

Where $h\nu_x$ is the photon energy of the exciton, $c_p = 0.25$ J/gK the specific heat [32], $\rho = 7.5$ g/cm^3 is the density of the bulk WS_2, and $d = 0.7$ nm the thickness of the monolayer. Solving the rate equation provides an analytical expression of the lattice temperature dynamics of the monolayer WS_2. The analytical expression of $T(t)$ is given in the appendix A.

I now have derived a simplified two-level model that provides the analytical expression of the microscopic quantities of photo-excited exciton density $n_x(t)$ and the

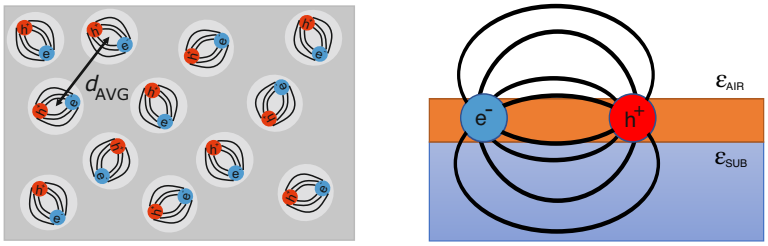

FIGURE 6.9: a) Sketch of top view of monolayer WS_2 in presence of photoexcited exciton density. b) Sketch of field lines between hole and electron constituting exciton in dielectric environment.

lattice temperature $T(t)$ of the WS_2 as a function of time. Unfortunately, it is not possible to directly measure these quantities with optical spectroscopy, and they must be related, in some way, to the observables of exciton peak shift Δx_0 and linewidth broadening Δg. This is done in the following subsection.

Optical observables

After having derived the microscopic photoexcited exciton density and the local lattice temperature as a function of time, it becomes necessary to relate such quantities to the optical observables of our experiments. The exciton peak shift and the linewidth broadening can depend non-trivially on the previously derived quantities. In general, a careful analysis of the fundamental processes and effects occurring in the TMDC is necessary when modelling the observables of an experiment. In particular, the theory chapter discussed how the presence of quasiparticles, through dynamic screening, induces a renormalization of the binding energy and quasi-free particle bandgap of TMDC materials, resulting in a shift of the excitonic resonance. Furthermore, section 2.1.4 shows how the temperature variation induces peak shift and broadening of the excitonic resonance. The way all these effects compete after photoexcitation, as also mentioned in chapter 5, and contribute to the time evolution upon photoexcitation of the excitonic resonance needs to be carefully modelled.

In this subsection, the optical observables of exciton resonance peak shift and linewidth broadening are described as a function of the microscopic quantities of exciton density and local lattice temperature. The peak shift is modelled with an effective dynamic screening-induced binding energy reduction, and the linewidth broadening is attributed to exciton-exciton scattering.

Fig. 6.9.a) shows the sketch of the top view of a monolayer WS_2 with the presence of a specific exciton density in the plane. The excitons are free to move in-plane, and they undergo scattering events between themselves. This suggests, therefore, the assumption that the linewidth broadening is proportional to the probability of a scattering event in a collisional scattering scenario. In the 2D case, the scattering rate scales proportional to the inverse of the square root of the average distance between particles, i.e. linearly with the exciton density [75]. The linewidth broadening is then

modelled with the following function:

$$\Delta g(t) = n_x * D \tag{6.11}$$

Where D is an excitation-induced broadening parameter for exciton-exciton scattering. It is known from the theory chapter that also the linewidth increases with increasing temperature. This contribution is not included in the fit function because, later in the section, we demonstrate that such contribution is negligible in the excitation densities treated in this work.

Regarding the exciton peak shift Δx_0, from Fig. 6.9.a), when excitons are densely packed together, they dynamically screen each other, in analogy to the quasi-free carrier dynamic screening described in section 2.2.2. In order to model the exciton energy, it is recalled from section 6.2.1 that the binding energy reduction is the dominant mechanism when a blue-shift of the resonance is observed. Moreover, phase-space filling effects were already excluded because of the bosonic nature of the exciton and since no spectral weight reduction upon photoexcitation in our experiments was observed. I also assume not varying quasi-free particle bandgap. The exciton binding energy can therefore be modelled assuming that it is proportional to the work needed to bring the electron at an infinite distance from the hole forming the exciton in a screened environment as sketched in Fig. 6.9.b).

The binding energy is then given by the formula:

$$E_B = \frac{e^2}{4\pi r_0 \varepsilon_0 (\varepsilon_{r_{static}} + \varepsilon_{r_{dyn}})} \tag{6.12}$$

where ε_0 is the vacuum dielectric constant, e is the charge of an electron, and r_0 is the distance between the electron and the hole forming the exciton. This value correspond in first approximation to the Bohr radius and it is arbitrarily fixed at 1 nm [33]. The relative permittivity consists of a static and a dynamic term. The firt one is $\varepsilon_{r_{static}}$, which is attributed to the screening of the dielectric environment. This parameter is fixed to the average of the permittivity of the substrate and air, which are the media in the immediate surrounding of the monolayer. This results in a value of $\varepsilon_{r_{static}} = (\varepsilon_{air} + \varepsilon_{SiO_2})/2 = 2.5$, analogously to the expression given in section 2.2.1. The relative permittivity of the fused silica substrate is taken from [118] The second dynamic term $\varepsilon_{r_{dyn}} = \alpha n_x$, assumed to be proportional to the exciton density through the coefficient α, and it is due to the dynamic screening of other excitons in the vicinity.

The exciton peak shift $\Delta x_0(t)$ as a function of time is then written as:

$$\Delta x_0(t) = E_{B_0} - E_B(t, n_x) + \beta * \Delta T \tag{6.13}$$

In which E_{B_0} is the equilibrium binding energy, $E_B(t, n_x)$ is given by Eq. 6.12 and the last term is a temperature-induced red-shift, as described in detail in section 2.1.4 of the theory chapter. The coefficient β=2.5-5 meV/K was estimated by Ruppert et al.

and can vary from sample to sample [32]. Eq. 6.13 and Eq. 6.11 relate the optical observables Δx_0 and Δg to the microscopic quantities described with the simplified phenomenological model.

To summarize, the time evolution of the exciton energy upon photoexcitation is described by an effective dynamic screening-induced binding energy reduction, in the approximation that the Bandgap does not vary. Instead, the photoinduced broadening of the excitonic resonance is mainly due to exciton-exciton scattering.

It is now possible to use Eq. 6.13 and Eq. 6.11 to fit the fluence dependent time evolution of Δx_0 and Δg shown in Fig. 6.7, eventually evaluating if and how accurate this model is in tracking the exciton dynamic response. This is performed in the next section.

Exciton role in dynamics

Which influence do excitons have on the exciton response upon photoexcitation is the central question of this section. The answer to such a question is now closer. In fact, in the previous sections, I derived a phenomenological two-level model describing the time evolution for the microscopic quantities of exciton density and local lattice temperature as a function of time. I then related these quantities to the optical observables of exciton peak shift and linewidth broadening, obtaining Equation Eq. 6.13 and Eq. 6.11. The equations above were used to fit the experimental traces initially shown in Fig. 6.7 to evaluate if this model reproduces the experiments, how accurately and with which parameters. From an eventual agreement of the model with the data, I can therefore estimate the validity of the assumptions used to derive the model itself and draw a conclusion on the origins of the exciton dynamics upon photoexcitation.

This subsection focuses on the isolation of the mechanism through which the density of photoexcited exciton governs the dynamical response of the excitonic resonance upon photoexcitation. By fitting the two-level model to the fluence dependent exciton peak shift and linewidth broadening as a function of time, it was found that the model accurately and quantitatively describes the observed trends. The best-fit parameters and the timescales of the relaxation processes are then discussed and found to be in agreement with previously reported literature values. This agreement justifies the assumption made in the derivation of the model, thus implying the accuracy of the model itself in describing the exciton dynamic response upon photoexcitation. Finally, the contributions of the dynamic screening and thermal effects to the total dynamics are isolated and discussed. Particularly, the competition between a blue-shift, modelled with an effective exciton binding energy reduction, and thermal-induced red-shift is unravelled. Furthermore, exciton-exciton scattering dominates the linewidth broadening. Ultimately, this section shines light on the complex interplay of electronic and thermal processes contributing to the dynamical response of the exciton upon photoexcitation.

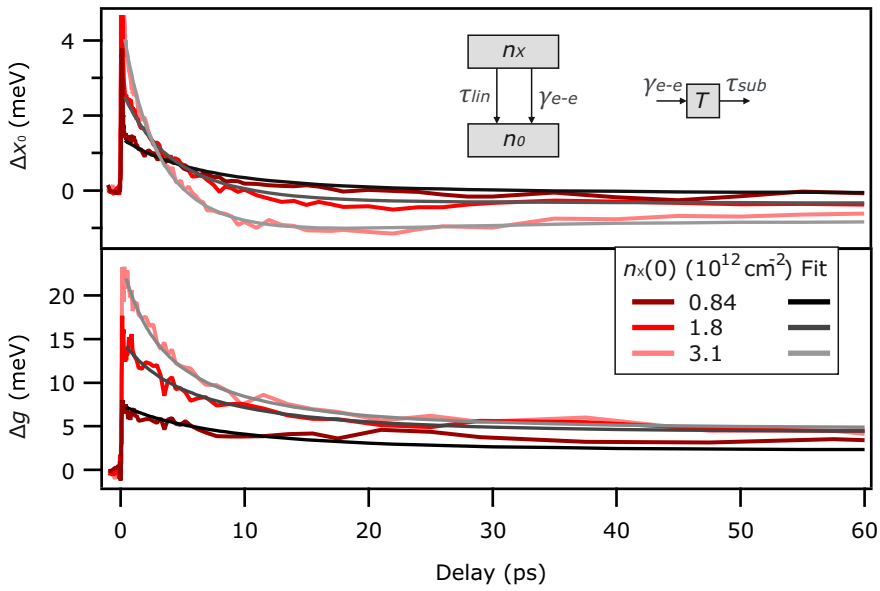

FIGURE 6.10: Exciton peak shift and linewidth broadening as a function of time delay for different fluence of resonant pumping from Fig. 6.7 and respective fits with Eq. 6.13 and Eq. 6.11

τ_{lin}	γ_{e-e}	τ_{sub}	α	D	β
18±5	0.06±0.01	14±8	(6.6±0.6) 10^{-15}	(5.6±0.2) 10^{-12}	0.4±0.1
10ths	0.05-0.1	10ths		5.4 E-12	0.25-0.5
ps	cm^2/s	ps-μs	cm^2	meV cm^2	meV/K

TABLE 6.3: Best-fit parameters for two-level model

Fig. 6.10 reports the exciton peak shift and linewidth broadening as a function of time delay for various fluences of resonant pumping. The data are the same as the one reported in Fig. 6.7 but plotted on a different time axis. I then perform a global fit to the time-dependent exciton peak shift and linewidth broadening with Eq. 6.13 and Eq. 6.11, respectively. The dynamics during the cross-correlation of the pump and the probe are not investigated in this work, as already mentioned in section 6.1.2. The fittings to the experimental curves are restricted from 150 fs after time zero, where an incoherent exciton population can be supposed. The best fits are reported in Fig. 6.10. It is immediately apparent that the fits reproduce the data accurately. The excellent agreement between the fit and the extracted dynamics of the exciton peak shift and linewidth broadening confirms that the essential two-level model, with its relative assumptions, can qualitatively reproduce the exciton dynamics accurately for excitation densities below the Mott transition.

In order to evaluate the quantitive detail, the first mention is that the global fit

with the phenomenological model to the data provides an estimation of the equilibrium binding energy, calculated with Eq. 6.12 for $n_x = 0$, for a monolayer of WS_2 deposited on a SiO_2 substrate, returning a value of 0.58 eV. This value is well within the range of 0.3 to 0.7 eV, which has been reported in different experiments compared in [6].

Proceeding now to the extracted best-fit parameters, these are reported in table 6.3. Focusing on the timescale of the exciton relaxation processes, which are recalled in the inset of Fig. 6.10. The excitons can recombine through two competing recombination channels. The first one is the exciton-exciton Auger recombination with an estimated rate of 0.06 cm^2/s. Although the exciton Auger recombination rate can vary depending on defect density and substrate of choice [65], the value extracted in our measurement is comparable to the rate previously reported ranging between 0.05 and 0.1 cm^2/s [136, 135, 137, 138].

The second recombination channel scales linearly with the exciton density and has a lifetime of 18 ps. According to our phenomenological model, this relaxation pathway does not transfer energy to the lattice, thus not contributing to the increase of the lattice temperature, thus suggesting such a channel as a possible radiative recombination process. The timescales for such radiative recombination process are reported to be in the order of the hundreds of ps or longer at room temperature [139]. It is more likely that the linear recombination channel used in our model combines radiative and non-radiative processes. Previous studies attributed this recombination channel to a defect trapping of the exciton with similar timescales of few ps, measured in [35] and theoretically predicted in [140], or to dark exciton formation [141]. More experiments will be required to confirm one or the other hypothesis, but this goes beyond the scope of this work. Lastly, the timescale of the thermal energy transfer to the substrate in the order of the tenths of ps is confident with the values already reported in the literature, which ranges between a few ps to ns [32]. The same last true also for the coefficient β. The best fit for the excitation-induced broadening returns a value D= 5.6 10^{-12} meV cm^2, which is confident with the value previously reported from Moody et al of D= 5.4 10^{-12} [75] and also comparable to, despite not confident, the value of 6.3 10^{-12} meV cm^2 extracted from Ruppert et al. in their work [32].

The consistency of the parameters extracted from the fit with literature values supports this simplified model of the dynamic response of the exciton resonance, thereby suggesting that the assumptions made are accurate. This allows concluding that, despite being a simplification, the simplified two-level model is accurate in describing the dominant exciton dynamics of monolayer WS_2 upon resonant photoexcitation. From this, it is discerned that the scattering events between photo-excited excitons are the primary source of the photoinduced broadening. Instead, the exciton peak position can be modelled with an effective binding energy reduction due to the exciton dynamic screening, causing the blue shift in the early stage after the pump pulse. At later time delays, the Auger recombination leads to an increase in

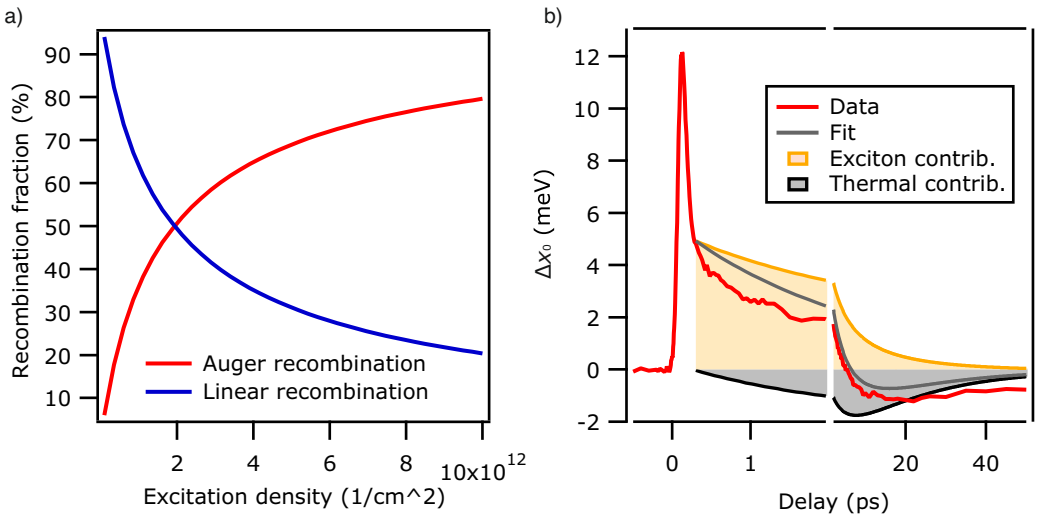

FIGURE 6.11: a) percentage of excitons that recombines through the linear channel or through the Auger channel, as a function of excitation density. b) Exciton peak shift as a function of time delay for initial photoexcitation density of 3.1 10^{12} cm^{-2}, same trace as in Fig. 6.2. Contribution to peak shift arising from screening-induced binding energy renormalization and temperature-induced shift.

the temperature inducing the observed red-shift at later time delays. The system then recovers within a few tenths of picoseconds.

Few other considerations are possible from this model, as shown in the following. Firstly, with the competition of the two exciton relaxation channels, one crucial aspect to consider is the relative ratio of one to another. Fig. 6.11.a) shows the ratio of excitons that recombines through the linear and Auger channels as a function of the excitation density, determined with the simplified model. This is achieved by calculating the number of excitons that recombines through the linear channel and through the quadratic Auger channel, for various initial excitation densities. At low excitation densities, the recombinations occur mainly rough the linear channel. Instead, at higher excitation densities, the Auger recombination becomes the dominant recombination channel. Remembering now that the Auger recombination transfers energy from the electronic system to thermal energy, it becomes apparent how, for higher photoexcitation densities, the dissipation in thermal energy becomes more pronounced. This has a significant impact on any application of TMDCs in optoelectronic devices, where thermal dissipation is a fundamental factor to be considered in the design.

Finally, the two parameters D and α quantify the effects due to the presence of excitons on the time-dependent exciton dynamics upon photoexcitation. To show that, I recall the resonant pumping experiment introduced in section 6.1.1. It is now possible to explain the origin of the observed peak shift and linewidth broadening. The broadening originates from scattering events between excitons which are more frequent the higher the density of exciton present in the system at any given time. This means that for resonant optical pumping, or when only excitons are present, the

broadening is directly proportional to the exciton density present in the system at any given time. The Eq. 6.11 shows that the broadening is linear with the excitation density through the excitation-induced broadening parameter D. The previously reported temperature-induced shift (section 2.1.4) is negligible in our experiment with these initial excitation densities.

The contributions of the single effects on the peak shift due to the transient presence of photoexcited excitons in the system are less recognizable than in the broadening case. The peak shift Δx_0 as a function of time delay for the resonant pumping experiment with a initial excitation density of 3.1 10^{12} cm^{-2} is shown in Fig. 6.11.b). The exciton density present in the system dynamically screens the Coulomb interaction with an effective permittivity $\varepsilon_{dyn} = \alpha n_x$, which induces a blue-shift that can be modelled with an effective binding energy reduction. This contribution to the shift is reported in Fig. 6.11.b) with the solid orange trace. This contribution dominates the shift in the early stages after photoexcitation. After, when excitons recombine through Auger scattering, they transfer energy to phonons, ultimately increasing the temperature of the lattice. Thus thermal-induced shift becomes the dominant phenomenon. This contribution is reported with the solid black trace in the same graph. The relative ratio of dynamic screening and thermal-induced shift provokes the blue-shift to red-shift crossover observed in the exciton peak shift. The higher is the initial excitation density, the higher is the thermal-induced shift with respect to the binding energy reduction, thus resulting in a blue to red-shift crossover at earlier time delays.

Summarizing, this subsection discussed the isolation of the mechanisms through which the density of the photoexcited exciton governs the excitonic resonance dynamic response upon photoexcitation. This was achieved by demonstrating that the basic phenomenological two-level model accurately reproduces the non-equilibrium response of the exciton peak shift and the linewidth broadening. From the fit, the timescales of the relaxation processes involved after photoexcitation are obtained and found to be in excellent agreement with previously reported values in the literature. This justified the assumption made in the model, allowing us to conclude that the scattering events between photo-excited exciton are the primary source of the photoinduced broadening. The peak shift instead is governed by the dynamic screening due to the photo-excited exciton population, which induced a blue-shift modelled whit binding energy. Furthermore, the temperature increase due to the Auger recombination is revealed to be the main mechanism leading to the observed red-shift at later time delays.

After describing the role of excitons in the non-equilibrium dynamics of the exciton peak shift and broadening for the resonant pumping, it is now natural to investigate the role of the quasi-free carriers. This is then performed in the next section.

Up to this point, in this section, I investigated the resonant pumping exciton dynamics of a monolayer WS_2 placed on a Si/SiO_2 substrate. The straightforward question that arises now is: what is the role of QFC in the exciton dynamic response.

Before dealing with this question though, I want to confirm the validity of the simplified two-level model for the resonant pumping in another sample, substrate and measurement technique. In order to do this, in the following subsection, I investigate the exciton dynamic response from a tr-TC experiment performed with another monolayer WS_2 placed on a fused silica substrate.

Confirming the model: transparent substrate

The model introduced in the previous subsections returned an accurate reproduction of the exciton dynamical response upon photoexcitation of a monolayer WS_2 placed on a Si/SiO_2 substrate. The global fit used in that case to retrieve the parameters describing the exciton response was performed on a limited amount of experimental traces of one experiment. In order to confirm the robustness of this model, it becomes necessary to evaluate its universality and accuracy ideally on the exciton dynamic response extracted from another sample, substrate and possibly with another measurement technique.

This section reports the global fit using the simplified two-level model to the non-equilibrium fluence dependence of exciton peak shift and linewidth broadening, extracted from the resonant pumping tr-TC experiment performed on a monolayer WS_2 placed on a fused silica substrate. A good agreement between the fit with the two-level model and the extracted peak shift and linewidth broadening is reported, supported by confident parameters with the tr-RC experiment with the Si/SiO_2 substrate of the previous subsection. This allows confirming the robustness of the model in tracking the exciton dynamic response upon resonant photoexcitation, independently of the sample, measurement technique and substrate of choice.

The sample investigated in this section is the same sample used and described in section 6.1.1. Fig. 6.12 displays the exciton peak shift and linewidth broadening as a function of time delay for different fluences, extracted from the tr-TC data of the monolayer WS_2 placed on a fused silica substrate, using the formalism described in section 6.1.3. It is immediately seen that the data show the same qualitative trends observed for the tr-RC experiments. This confidence was also expected from the conclusion of section 6.1, stating that the exciton dynamic response is independent of the static screening from the dielectric environment. The resonance initially displays blue-shift, which eventually turns into a red-shift for later time delays, sooner the higher the excitation density. The broadening increases with excitation density and seems to have a shorter lifetime the higher the initial photoexcitation density.

I then again perform a global fit of Δx_0 and Δg using the two-level model, particularly Eq. 6.13 and Eq. 6.11, respectively. The best fits are reported in Fig. 6.12, displaying an excellent agreement with the data. This agreement already confirms qualitatively the reliability and robustness of the model in reproducing the observed dynamics also in this independent experiment.

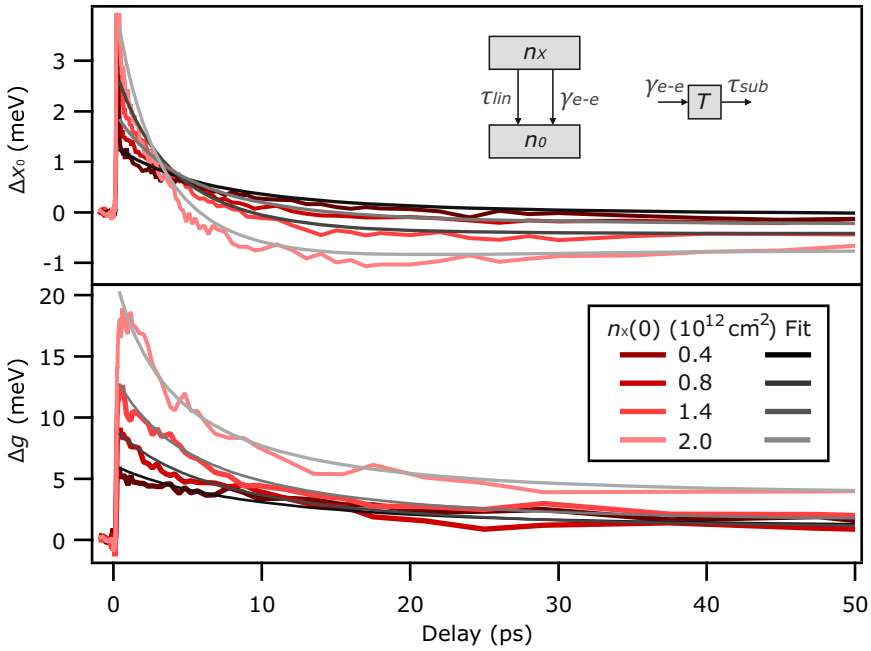

FIGURE 6.12: Exciton Peak shift and linewidth broadening as a function of time delay for different fluence of resonant pumping of a monolayer WS_2 deposited on a fused silica substrate, and respective fits with Eq. 6.13 and Eq. 6.11

	τ_{lin}	γ_{e-e}	τ_{sub}	α	D	β
Si/SiO_2	18±5	0.07±0.01	14±8	(6.6±0.6) 10^{-12}	(5.6±0.2) 10^{-12}	0.4±0.1
FS	18±5	0.07±0.01	14±8	(6.0±0.4) 10^{-12}	(5.3±0.3) 10^{-12}	0.4±0.1
	ps	cm^2/s	ps	cm^2	meV cm^2	meV/K

TABLE 6.4: Best global fit parameters obtained from the fit with the two-level model from experiment on layered Si/SiO_2 substrate and FS substrate.

To make this quantitative, a comparison of the extracted parameters with the parameters extracted for the Si/SiO_2 sample is necessary. The comparison is reported in the table 6.4.

The parameters extracted from the two different experiments show a remarkable agreement since all the parameters are equal or confident with each other. This allows to conclude then that the photoinduced non-equilibrium dynamics are independent of the local dielectric disorder that can be present in two substrates with nominally equal relative permittivity. Instead, the exciton dynamic response is mainly sensitive to the excitation condition, therefore, to the excited quasiparticle population. Actually, the complete influence of the static dielectric environment on the exciton dynamic response will be subject to discussion in the next section 6.3, where a substrate-dependent analysis will be performed.

Overall, It is now concluded that the simplified two-level model introduced in this section is accurate in describing the exciton dynamic response upon resonant

pumping. This model allows to identify the role of the dynamic screening and scattering of excitons, which are transiently present in the system, as the main responsible for the peak shift and linewidth broadening. Most importantly, the robustness of this model in reproducing the exciton dynamics upon photoexcitation is confirmed, not only in one experiment but independently of the sample, measurement technique, and substrate of choice.

6.2.3 Quasi-free carriers dynamic screening

After having described the effects arising from the presence of the excitons in the photoinduced peak shift and broadening of the excitonic resonance upon photoexcitation, I now focus on the influence of the quasi-free carriers (QFC). Recalling the experiment performed at the beginning of this chapter, in section 6.1.1 it was concluded qualitatively that, for the above-resonance pumping, the different dynamics of the excitonic resonance were attributed to the presence of QFC in the early stage after photoexcitation. Furthermore, from the discussion of the previous section 6.1, the conclusion was that, when excitons are transiently present in the system, the dynamic screening governs the exciton peak shift and the exciton-exciton scattering is the primary source of the broadening. From this, the question that arises is: what is the role of the QFC in the peak shift and broadening?

To answer this question, analogously to the resonant pumping experiment performed in the previous section, I investigate the above-resonance fluence dependent exciton dynamic response upon photoexcitation. I then extend the microscopic two-level model, introduced in section 6.2.2, to a three-level model to include the presence of QFC photogenerated upon above-resonance pumping. I further proceed to relate the quasiparticle population to the optical observables of exciton peak shift and linewidth broadening. By fitting the fluence-dependence of the last two quantities with the three-level model, the isolation of the role of QFC in the dynamics is achieved. The agreement of the model with the experimental traces allows concluding that the dynamic screening originating from the presence of QFC in the system induces a red-shift that can be modelled with an effective bandgap renormalization. The linewidth instead has an extra broadening mechanism corresponding to QFC-exciton scattering. Ultimately, I isolate the contributions of QFC and exciton to the dynamic exciton response in the case of above-resonance pumping. This section shines light on the complex interplay of electronic and thermal processes governing the exciton response upon above-resonance pumping.

Fig. 6.13 shows the exciton peak shift Δx_0 and linewidth broadening Δg as a function of time delay for different fluences of the above-resonance pumping. The excitation conditions are analogous to the above-resonance pumping experiment described in section 6.2.1, with the pump tuned at 3.1 eV and the initial absorbed photon density $n_{h\nu}$ is calculated as described in B.

The exciton energy as a function of time shows an instantaneous red-shift, which quickly recovers, eventually turning into a blueshift. After, the blueshift diminishes,

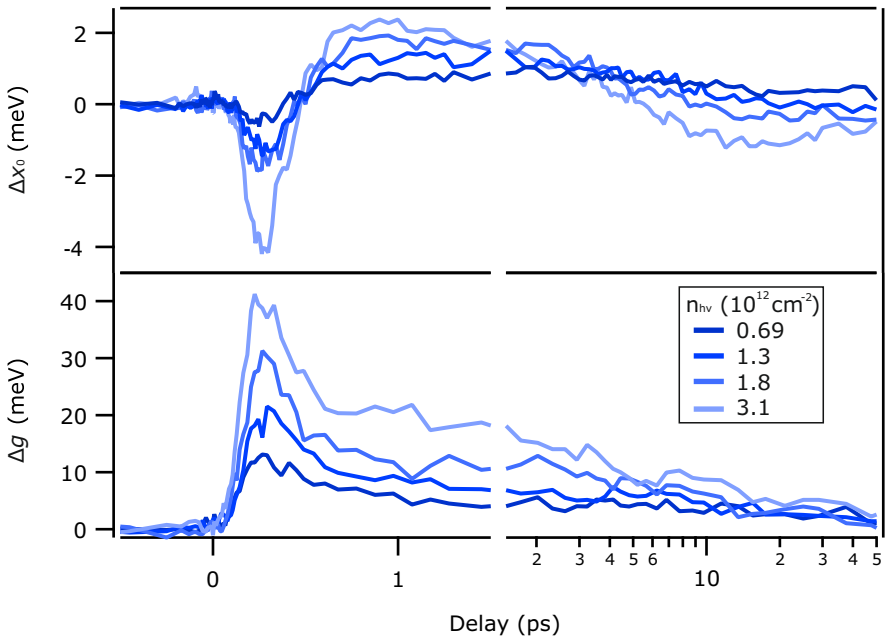

FIGURE 6.13: Exciton peak shift and linewidth broadening as a function of time delay for different fluence of above-resonance pumping.

eventually turning again in a slight red-shift, in total analogy with the resonant pumping experiment. The crossover to the red-shift happens, once again, sooner the higher the fluence. The slower dynamics seem to be similar to the resonant pumping case. The linewidth instead shows a stronger broadening with respect to the resonant pumping case, which lasts only a few hundred femtoseconds, relaxing on a similar timescale as the first red-to-blueshift crossover in the exciton peak shift. The broadening recovery is analogous to the resonant pumping case and occurs in a few tenths of picoseconds. The recovery is quicker the higher the fluence. The spectral weight, also in this experiment, does not change significantly upon photoexcitation. All these trends are stable upon different fluence.

Section 6.1 already qualitatively attributed the different early-stage dynamics of the above-resonance pumping, with respect to the resonant pumping case, to the presence of QFC. In fact, the pump photon energy is well above the quasi-free particle bandgap of the monolayer WS_2, thus it can photoexcite electrons high in the conduction band. The main difference between the resonant pumping and above-resonance pumping is that QFC are photoexcited instead of excitons [90]. The QFC will then relax, forming excitons, typically on hundreds of femtosecond timescales [142]. Once all the QFC relaxed, forming excitons, then the time evolution of the excitonic resonance should intuitively be similar to the resonant pumping case.

From this experiment, it is qualitatively confirmed the hypothesis that the different peak shift and broadening of the excitonic resonance in the above pumping scenario originate from the presence of QFC in the system. The quantitative description of the effects that the QFC have on the exciton energy and linewidth dynamics

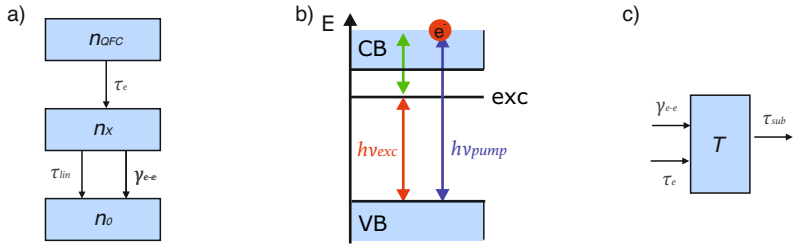

FIGURE 6.14: a). Sketch of phenomenological 3-level model. b) Sketch of QFC thermalization and excess energy (green arrow). c) Sketch of the model for local lattice temperature increase

is quite involved, and it is treated in the following subsection.

Three-level model and thermal dynamics

Section 6.2.2 proposed a phenomenological two-level model to describe the microscopic quantity of photoexcited exciton density and local lattice temperature. By using this model to fit the fluence dependence of the exciton dynamics upon resonant pumping, the mechanisms governing the observed dynamics were unveiled. Knowing the effect that the presence of an exciton density has on the exciton's dynamical response, it now would be crucial to understand what changes when QFC are transiently present in the system.

To unravel the role of the QFC in the peak shift and broadening of the excitonic resonance upon photoexcitation, the simplified two-level model, introduced in section 6.2.2, is extended to include the presence of QFC. This is achieved by a three-level model and an appropriate modification of the modelling of the observables of the experiments, introduced in section 6.2.2.

A three-level system for the above-resonance pumping scenario is assumed as depicted in Fig. 6.14.a). The excitonic level and the ground state are the same as in the resonant case, and the QFC state is given by a level above the excitonic one. An initial photo-excited QFC density is generated in the system with the pump pulse. The initial photoexcited QFC density is given by $n_{QFC}(0) = 2n_{h\nu}$, with $n_{h\nu}$ being the absorbed photon density. This is to account that for every absorbed photon, a quasi-free electron and a hole are excited in the system. These quasi-free carriers will then thermalize, ultimately forming excitons at a rate of $1/\tau_e$, described by the following equation

$$\frac{dn_{QFC}(t)}{dt} = -\frac{1}{\tau_e} n_{QFC} \tag{6.14}$$

Solving this rate equation, for the initial condition of $n_{QFC}(0) = 2n_{h\nu}$, returns a simple exponential decay. Due to the quick nature of the electron relaxation in the conduction band, it is not possible to assume an instantaneous creation of the QFC

density. Therefore the expression of $n_{QFC}(t)$ is convoluted with a Gaussian mimicking the pump pulse, thus providing the QFC density at any given time after photoexcitation.

The exciton density $n_x(t)$ created from the relaxation of QFC then relaxes through exciton-exciton Auger recombination and a linear channel, analogously to the resonant pumping case. The rate equation governing the and exciton density n_x is then given by:

$$\frac{dn_x(t)}{dt} = +\frac{1}{2\tau_e} n_{QFC} - \frac{1}{\tau_{lin}} n_x - \gamma_{e-e} n_x^2 \tag{6.15}$$

In Eq. 6.15, the first term is a filling term due to the QFC relaxation resulting in the formation of the excitons. The second and third terms correspond to the linear recombination channel, with lifetime τ_{lin}, and the exciton Auger recombination, with rate γ_{e-e}. The last two terms are analogous to the two-level system used for the resonant pumping case. By numerically solving the last equation for the initial conditions and $n_x(0) = 0$, the time-dependent exciton density $n_x(t)$ as a function of time is obtained.

With this, the three-level model extends the two-level model to include the presence of QFC to model the excited particle populations transiently present in the system. Regarding the temperature increase, when hot QFC are present in the system, another channel for the energy transfer from the electronic system to the increase of lattice temperature other than the Auger scattering must be included. Indeed, the relaxation of the hot quasi-free carriers forming excitons occurs through phonons emission, ultimately increasing the local lattice temperature. The subject of hot QFC thermalization in monolayer TMDC is complex and has been investigated carefully in the case of MoS_2 in [143]. In this case, the subject topic is simplified by considering the following. The excess energy that every single QFC have with respect to an exciton, considering the same excitation density between the resonant and above resonant case, is given by $h(\nu_{pump} - \nu_x)$. Here, ν_{pump} and ν_x are the frequencies of pump and the excitonic resonance, respectively, as sketched in Fig. 6.14.b). To obtain the total excess energy, it is sufficient to multiply the excess energy of a single QFC by the total number of QFC divided by two $n_{QFC}(0)/2$. In a first approximation, it is possible to assume that this excess energy is transferred to the lattice at the same rate of the exciton formation, as depicted in Fig. 6.14.c). Analytically the rate equation for the temperature increase can be written as:

$$\frac{dT(t)}{dt} = \frac{1}{2\tau_e} n_{QFC} \frac{h(\nu_{pump} - \nu_x)}{\rho c_p} + \gamma_{e-e} n_x^2 \frac{h\nu_x}{\rho c_p} - \frac{1}{\tau_{sub}} T \tag{6.16}$$

The first term corresponds to the QFC relaxation contribution, the second to the Auger recombination contribution, and the third is the thermal energy transfer to the substrate. c_p, ρ, and d are the specific heat, density and thickness of the monolayer WS_2 with the same value reported in section 6.2.3.

By numerically solving Eq. 6.16, the time-dependent local lattice temperature increase is obtained. The equation is solved numerically due to the lack of an analytical solution.

I now have extended the phenomenological model of the quasiparticle population to include the presence of QFC and exciton that are present when the system is photoexcited above-resonance. I also included the QFC relaxation in the mechanism through which the energy is transferred from the electronic system to thermal energy. Finally, the expression of the exciton density, QFC density and temperature at any given instant of time after the photoexcitation are available.

It is important to notice that the two-level model introduced in section 6.2.2 is a subcase of the three-level model. In fact, it can be derived from the same set of equations of the three-level model, but with the different initial condition of $n_x(0) = n_{h\nu}$. It becomes then necessary to relate these quantities to the optical observables, which will be the subject of the next subsection.

Optical observables

After having derived the microscopic time-dependent exciton and QFC density and the local lattice temperature for the above resonant pumping, it is fundamental to relate such quantities to the optical observables of our experiments. From section 6.2.2 it is known how the presence of excitons influences the excitonic resonance. In particular, the peak shift was modelled with an screening-induced effective binding energy reduction, and the linewidth broadening was attributed to exciton-exciton scattering. It remains to understand what is the role of the QFC.

In this subsection, the optical observables of exciton peak shift and linewidth broadening are described as a function of the microscopic quantities of exciton density, QFC density, and the local lattice temperature from the three-level model. The derivation of the analytical expression of the two observables is an extension of the analogous modelling made in section 6.2.2 where the role of the QFC is also included. In particular, the presence of QFC induces a red-shift that can be modelled with bandgap renormalization due to screening and adds an extra collisional broadening mechanism corresponding to QFC-exc scattering.

Considering the linewidth of the excitonic resonance firstly. The presence of free carriers in the system allows an extra collisional broadening channel, corresponding to the QFC-exciton scattering. The equation governing the photoinduced broadening, in a collisional scattering scenario, is described by the following equation:

$$\Delta g(t) = n_x * D + n_{QFC} * K \tag{6.17}$$

where D is the excitation-induced broadening parameter due to exciton-exciton scattering, analogously to the resonant pumping case. K is the excitation-induced broadening parameter due to QFC-exciton scattering.

In order to model the QFC induced peak shift, when QFC are present in the system, the bandgap renormalization cannot be neglected. Analogously to the binding energy reduction induced by the dynamic screening due to the presence of excitons, the different screening from the QFC induces an effective red-shift. In the attempt to describe such an effect, an effective bandgap renormalization is assumed as the primary mechanism of the effective red-shift of the excitonic resonance. The fluence dependence of the photoinduced bandgap renormalization is not trivial, and it is discussed by Liu et al. in their work for MoS_2 [115]. In this work, I just phenomenologically assume a linear dependency in the quasi-free carrier density. Such assumption consists of a first rough approximation that lasts valid for a small fluence range.

The fit function for the peak shift can be obtained by extending the equivalent Eq. 6.13 for the resonant pumping case.

$$\Delta E_x(t) = E_B(eq) - E_B(n_x(t)) + \beta * \Delta T(t) - E_{QFC} * n_{QFC}(t) \tag{6.18}$$

Where $E_B(eq)$ is again the equilibrium binding energy, E_B is given by the Eq. 6.12, $\Delta T = T(t) - T_0$, and the last term includes the effective redshift due to the presence of quasi-free carriers, linear with the QFC density through the coefficient E_{QFC}.

I now have related the microscopic quantities of QFC and exciton densities and local lattice temperature to the optical observables, thus providing the analytical expression for the peak shift and linewidth broadening in the case of above-resonance pumping. It is now possible to evaluate the model's accuracy and its relative assumption by fitting it to the experimental data, as done in the following subsection.

QFC vs exciton role in the exciton dynamic response

In the previous two sections, I developed a phenomenological three-level model of the quasiparticle dynamics, with corresponding local lattice temperature increase, for the above-resonance photoexcitation. I then related this phenomenological model to the optical observables of exciton peak shift and linewidth broadening. It is now possible to evaluate the accuracy of this model, and relative assumptions, by fitting the phenomenological model to fluence dependent peak shift and broadening of the exciton upon above-resonance photoexcitation. By fitting the model to the data is eventually possible to unravel the role of the QFC in the exciton dynamical response.

This subsection unravels the mechanism through which the photoexcited QFC governs the dynamical response of the excitonic resonance upon above-resonance photoexcitation. Moreover the interplay of the effects originating from the presence of QFC and excitons is unravelled, ultimately discussing the different dynamic screening of the two different quasiparticle species. By fitting the three-level model

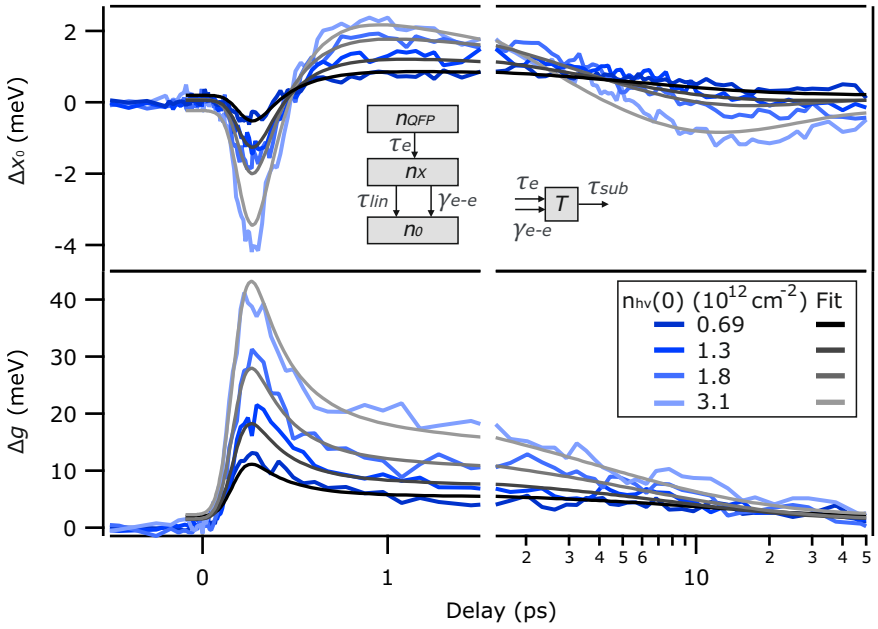

FIGURE 6.15: Exciton peak shift and linewidth broadening as a function of time delay for different fluence for above-resonance pumping from Fig. 6.13 and respective fits with Eq. 6.18 and Eq. 6.17

to the fluence dependence of exciton peak shift and linewidth broadening as a function of time, in the case of the above resonant pumping, it is found that the model accurately reproduces the observed trends. The best-fit parameters and the timescales of the relaxation processes of QFC are then discussed. Once again, the good agreement of the data and the model, supported by fit parameters shared with the resonant pumping case and in agreement with previously reported literature values, supports such a basic but comprehensive view on the exciton dynamic response. This confirms the validity of the assumptions made in the derivation of the model itself. The contribution of the QFC dynamic screening to the total exciton dynamics is isolated from the exciton dynamic screening and thermal contributions. The conclusion is that the QFC, through dynamic screening, induce a redshift which can be described with an effective bandgap renormalization, and through QFC-scattering, they add an extra linewidth broadening channel. From this, the quantitative detail of the effective peak shift originating from the presence of the two quasiparticle species are compared, finding that per unit of photoexcited quasiparticle, excitons effectively induce a stronger blueshift that the QFC induced red-shift. The physical meaning of this effective screening is finally related to the real binding energy reduction and quasi-free particle bandgap occurring when both quasiparticles are present. Ultimately, this section shines light on the complex interplay of electronic and thermal processes contributing to the dynamical response of the exciton upon photoexcitation.

Fig. 6.15 shows the exciton peak shift and linewidth broadening as a function of

τ_e (fs)	200± 10	$\leq$ 1000 [144]
τ_{lin} (ps)	18 ± 5	10ths [32]
γ_{e-e} (cm^2/s)	0.06 ± 0.01	0.05-0.1 [136, 145, 137, 146]
τ_{sub} (ps)	14 ± 8	ps-μs [32, 69, 71]
β (meV/K)	0.4 ± 0.1	0.25-0.5 [32]
α (cm^2)	(6.6 ± 0.6) 10^{-15}	
E_{QFC} (meV cm^2)	(1.2± 0.1) 10^{-12}	
D (meV cm^2)	(5.6 ± 0.2) 10^{-12}	5.4 10^{-12} [75]
K (meV cm^2)	(9.8 10 ± 0.2) 10^{-12}	

TABLE 6.5: Best-fit parameters of the two/three-level model.

time delay for different fluence for the case of above-resonance pumping. The data are the same as the one reported in Fig. 6.13. I then perform a global fit of the three-level model to the time-dependent exciton peak shift and linewidth broadening with Eq. 6.18 and Eq. 6.17, respectively. The parameters which are in common with the resonant pumping case are fixed at the same values extracted previously for the resonant pumping, and they are listed in section 6.2.2. The fitting includes points before time zero because, for above-resonance pumping, no resonant phenomena are occurring at the excitonic resonance. Furthermore, the photoexcitation process was included in the model in the derivation of the three-level model. The best fits are reported in Fig. 6.15, and they confidently reproduce the data.

To provide the quantitative details, the evaluation of the best-fit parameters extracted from the aforementioned fitting is reported in the following. The best-fit parameters are reported in the table 6.5, together with the parameters extracted from the resonant pumping case of section 6.2.2.

As mentioned before, the common parameters between the resonant and above-resonance pumping cases are fixed to the same value. The other parameters used only for the above-resonance pumping are then discussed in the following. The extracted exciton formation time of τ_e=200 fs that resulted from the fit is in the same order of magnitude as the previously reported sub-ps timescales [144, 142], eventually specifying it.

The two remaining parameters are K and E_{QFC} which are not reported before in literature. Those parameters determine the effect on the excitonic resonance due to the presence of a QFC density in the system. Before discussing this other parameters, it is convenient to discuss the implication of the excellent agreement between the fit and the extracted dynamics of the exciton peak shift and linewidth broadening. This excellent agreement of the fit and the data, supported by parameters in agreement with previously reported values in literature, confirms that such a basic model restricted to the dominant mechanisms, with its relative assumption, is accurate in reproducing the exciton dynamic response for the above-resonance pumping for excitation densities below the Mott transition. This strongly suggest that the three-level

model, derived from the two-level model used to picture the exciton effect on the dynamic exciton response, is accurate in reproducing the competing effect of QFC and exciton induced dynamics. It is possible to conclude that the QFC role in the dynamics consists of a linewidth broadening due to QFC-exciton scattering and a red-shift of the excitonic resonance that can be modelled with an effective bandgap renormalization due to the QFC dynamic screening. These two phenomena are quantitatively described by the parameters E_{QFC} and K, which were not reported in the literature before.

The QFC-exciton scattering is linear in the QFC density n_{QFC} through the excitation-induced broadening parameter F= 9.8 10^{12} meV cm^{-2}. This value is roughly two times higher than the corresponding exc-exc excitation induced broadening parameter D. This is explained considering the higher mobility of QFC with respect to the excitons, the latter having constrained degrees of freedom due to the Coulomb interaction between electron and hole. Similar estimation of the excitation-induced broadening coefficient for exc-exc scattering and QFC-exc scattering were performed for quantum well samples, also observing a higher value for the case of QFC-exc with respect to exc-exc scattering [147].

The peak shift resulting from QFC dynamic screening induced bandgap renormalization, given by the last parameter $\Delta E = E_{QFC} n_{QFC}$=1.2 meV cm^{-2}*n$_{QFC}$ is on the same order of magnitude of the blue-shift induced by exciton dynamic screening, given by $\alpha = \varepsilon_{r_{dyn}}/n_x(t)$ via Eq. 6.12. A more detailed description and analysis of the two last mentioned parameters will be given at the end of this subsection. First though, in the attempt of better comprehend this model, it is important to understand that it is from these competing effects, combined with the exciton formation time τ_e, that the blue or red-shift of the exciton resonance is determined after photoexcitation for monolayers WS_2 and, presumably, also in other two-dimensional materials with reduced screening.

To better understand the last statement, it is possible to isolate the contribution of different quasiparticles to the broadening and peak shift of the exciton upon photoexcitation. I recall once more the comparison of resonant/above-resonance pumping experiment introduced in section 6.1.1. In particular, I discuss the above-resonance pumping case by visually disentangling all the contributing factors to the peak shift and broadening, analogously at the isolation of the exciton effects in the resonant pumping performed in section 6.2.2.

Fig. 6.16 shows the peak shift and linewidth broadening as a function of delay for the above-resonance pumping with an initial photoexcitation density of 3.1 10^{12} cm^{-2}, same as the above-resonance pumping data from the experiment of section 6.2.1. The best fits obtained from the global fit are also reported on the same axis with the grey traces.

By evaluating the separate contributions in Eqs. 6.18 and 6.17 I disentangle the relative contribution of the QFC and exciton to the exciton dynamic response, including also the thermal effects. Starting from the broadening, shown in the bottom

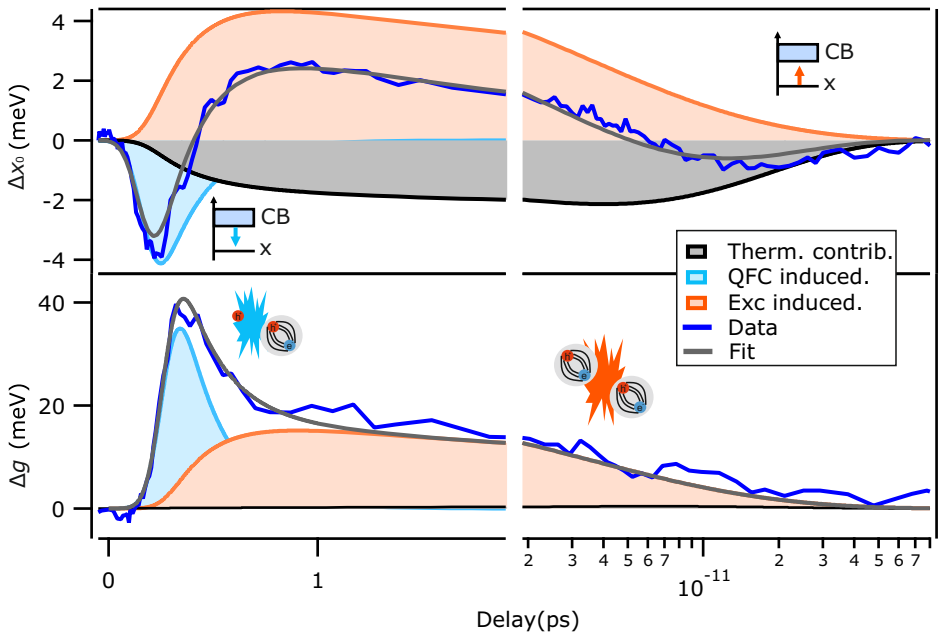

FIGURE 6.16: Top panel: Exciton peak shift as a function of time delay, for above resonant pumping with n_0=3.1 10^{12} cm^{-2}, and corresponding fit with Eq. 6.18. The contributions to the peak shift originating from the transient presence of QFC and exciton are shown with with the light blue and orange solid trace, respectively. The thermal induced shift is shown with the black trace. Bottom panel: photoinduced broadening and respective fit with Eq. 6.17. Contribution to the broadening originating from QFC-exc and exc-exc scattering, in light blue and orange solid traces, respectively.

panel of Fig. 6.16, when a QFC density is photoexcited in the system, it quickly relaxes, eventually forming exciton. When the QFC are present, they scatter with exciton and induce a linewidth broadening through QFC-exciton scattering, reported with the solid light blue trace. When the QFC density diminishes, thus increasing the exciton density in the system, the exc-exc scattering becomes the dominant mechanism of linewidth broadening, as reported with the solid orange trace. Thermal effects in the linewidth broadening, discussed in the first chapter section2.1.4 are negligible, as shown by the solid grey trace that is barely distinguishable from the x-axis. The maximal temperature increase across the experiments performed in this work is of 4/5 K.

Analogously to the broadening case, the different contributions to the peak shift are discussed. In Fig. 6.16 top panel, the contributions to the peak shift originating from the presence of QFC and exciton in the system are shown. When the QFC density is present at early time delays, the QFC dynamic screening, reproduced with an effective bandgap renormalization, is the main origin of the effective red-shift, outlined with the solid light blue trace. Once the QFC relax forming excitons, the main contribution to the shift is the one arising from the effective dynamic screening-induced exciton binding energy reduction, depicted with the solid orange trace. Furthermore, in the case of above-resonance pumping, the temperature-induced shift, due to the inclusion of the QFC relaxation contribution, becomes significant already in the early stages after photoexcitation. Eventually, thermal effects become the dominant contribution to the shift for later time delays, as shown by the solid black trace.

The Fig. 6.16 is the clear demonstration of how this thesis can disentangle and isolate the different physical phenomena, specifically exciton and QFC dynamic screening, and thermal effects, competing in the exciton dynamic response upon photoexcitation.

It is now possible to go deeper, from a quantitative point of view, in the understanding of the effective screening parameters that are extracted from this model. This will ultimate provide a picture on the different and competing QFC and exciton dynamic screening. Firstly, it is important to spend some words on the binding energy reduction used to model the initial blueshift due to the transient presence of excitons in the system. It was shown that the time-dependence of the exciton binding energy, given by Eq. 6.12 (shown also in Eq. 6.19) is in the effective dielectric permittivity $\varepsilon = \varepsilon_s + \alpha n_x(t)$. It is notable that for the parameters extracted from the fitting $\alpha n_x(t) \ll \varepsilon_s$ (0.02 $\ll$ =2.5 obtained for n_x= 3.1 10^{12} cm^{-2}, corresponding to the maximum exciton density used in this work). Under such conditions, it is then possible to linearize the exciton-induced binding energy change as follow:

$$\Delta E_B = \frac{e^2}{4\pi r_0 \varepsilon_0}\left(\frac{1}{\varepsilon_{r_{static}}} - \frac{1}{\varepsilon_{r_{static}} + \alpha n_x(t))}\right) \approx \frac{e^2}{4\pi r_0 \varepsilon_0}\left(\frac{\alpha n_x(t))}{\varepsilon^2_{r_{static}}}\right) = \frac{E_{B_0}\alpha}{\varepsilon_{r_{static}}} n_x(t) = E_x n_x(t) \tag{6.19}$$

where in the last equality we defined $E_x = E_{B_0}\alpha/\varepsilon_{r_{static}}$. The last expression of ΔE_B

means that, for the case of small dynamic relative permittivity αn_x, the blue-shift originating from binding energy reduction is linear in the exciton density, through the coefficient E_x. This expression enables the comparison of exciton-induced blueshift with the QFC-induced redshift. In fact the expression of the peak shift, given by Eq. 6.18 becomes:

$$\Delta x_0(t) = +\beta * \Delta T(t) - E_{QFC} * n_{QFC}(t) + E_x * n_x(t) \tag{6.20}$$

From the last expression of $\Delta x_0(t)$ it is clear that E_x and E_{QFC} can be compared. When substituting the values of the parameter for calculating E_x we obtain E_x = 1.6 10^{-12} meV/cm^2. This value can be compared E_{QFC}=1.2 meV cm^{-2}. It is clear that the effective blueshift originating from exciton-induced screening is stronger than the redshift modelled with bandgap renormalization due to the presence of QFC. Nevertheless, the two values are in the same ball park but, considering the presence of double the amount of QFC in the system with respect to exciton in the case of same absorbed photon density, this implies a stronger QFC induced red-shift, thus explaining the comparably large effect of carrier screening on the free particle band gap.

Talking now about the physical meaning of the effective screening coefficients E_x and E_{QFC}, it is important to understand their origin and their actual meaning. It is well known that, when quasi-free carriers are present in the system, their screening induces simultaneous exciton binding energy reduction, through screening of the attractive Coulomb interaction of electron and hole, and bandgap renormalization, due to the changes in the self-energy originating by the screening of the repulsive electron-electron interaction [148]. This can be written as:

$$-E_{QFC}n_{QFC} = -E_{BGR}^{QFC} * n_{QFC}(t) + \frac{E_{B_0}\alpha'_{QFC}}{\varepsilon_{r_{static}}} n_{QFC} \tag{6.21}$$

Here the first term corresponds to the real QFC induced BGR, linear in the QFC density through the coefficient E_{BGR}. The second term is, instead, the QFC-induced BER. The real binding energy reduction depends on the parameter α'_{QFC} which is proportional to the screening of QFC per unit of quasiparticle. In the same way, when excitons are present in the system, they induce exciton binding energy reduction, but they can also induce bandgap renormalization due to the dipolar screening of the repulsive electron-electron interaction, ultimately inducing changes in the exciton self-energy. Formalizing the last statement into the last equation, we obtain:

$$E_x n_x = -E_{BGR}^{x} * n_x(t) + \frac{E_{B_0}\alpha'_x}{\varepsilon_{r_{static}}} n_x \tag{6.22}$$

It is immediately concluded that, when QFC are present in the system, the bandgap renormalization is stronger with respect to the binding energy reduction. Instead, when excitons are present in the system the second effect is the dominant one. This is a clear result. The crucial point that needs to be emphasised now is that the

two/three level model is an effective phenomenological model and the contributions to the exciton-induced BER and QFC-induced BGR to the shift are effective contributions. Nevertheless, this model is still fundamentally important because it captures quantitatively the effective resulting competition of the real BGR and BER when either QFC or excitons are present in the system. This is a milestone since it provides a predictive model that can be used for experimentalist, providing material properties, and also be used for comparison of theory studies with experimental ones.

From here it is possible to tentatively compare the relative contributions from the competing effects. Based on the discussion presented in the theory chapter (section 2.2.2), we could argue that exciton screening is less efficient than quasi free carriers screening due to the various degrees of localization of the two quasiparticle species. Therefore this could lead to a negligible BGR effect, with respect to the BGR effect that the same QFC density would provoke. Thus, we could argue that the first term in Eq. 6.22 could be neglected. In such a tight approximation we have that $\alpha'_x = \alpha$. If we rewrite 6.21, by multiplying and dividing the last term by α, we obtain:

$$-E_{QFC}n_{QFC} = -E_{BGR}^{QFC}n_{QFC}(t) + \frac{E_{B_0}\alpha}{\varepsilon_{r_{static}}}\frac{\alpha'_{QFC}}{\alpha}n_{QFC}(t) \tag{6.23}$$

Here the fraction $\frac{\alpha'_{QFC}}{\alpha}$ is a ratio of the coefficient determining the real screening of the Coulomb attractive interaction originating from the presence of QFC or excitons. We previously assumed that the screening of QFC is more efficient than exciton screening. Therefore it is legitimate to assume that $\alpha'_{QFC} \gg \alpha$. In this case then, it is immediately concluded that the actual bandgap renormalization is stronger than the effective BGR captured from the two/three-level model. Futhermore, it is seen that in this case the E_{BGR}^{QFC} is higher in magnitude than $\frac{E_{B_0}\alpha}{\varepsilon_{r_{static}}}$, but E_{QFC} is smaller than the binding energy reduction. The last relations means that the real BGR is stronger than the real QFC or exciton-induced BER, and also stronger than the effective bandgap renormalization captured by $E_{QFC}n_{QFC}$.

This last conclusion must be interpreted as a speculation, which ultimately explain the physical meaning of the effective screening coefficients. From the measurement presented in this thesis it is not possible to retrieve the single contributions to Eqs. 6.21 and 6.22. Other measurements techniques which are sensitive to the actual binding energy or quasi-free particle bandgap are necessary to prove if the initial assumption is accurate. A clever method to reveal the transient exciton binding energy upon photoexcitation with optical techniques was reported by Cunnhingham et al [30]. They report that the presence of excitons induces simultaneously BER and BGR, with the two effects being in the same order of magnitude but with opposite signs. The resulting peak shift of the excitonic resonance is then one order of magnitude less than the changes in binding energy, with values comparable to the one observed in this thesis. This work was also supported by a theoretical paper from Steinhoff et al. [90] where they report a similar trend of BGR due to the presence of

exciton, despite with a slightly smaller amplitude.

If we now retake the discussion from Eqs. 6.21 and 6.22 but this time neglecting the hypotesis of negligible E^x_{BGR}, based on the last paragraph. We can still assume that $\alpha'_{QFC} > \alpha'_x$ due to the higher polarizability of QFC with respect to excitons [90]. This means that $\frac{E_{B_0}\alpha'_x}{\varepsilon_{r_{static}}} < \frac{E_{B_0}\alpha'_{QFC}}{\varepsilon_{r_{static}}}$ meaning that the real binding energy reduction is stronger when QFC are present in the system with respect to excitons. In the case of QFC dynamic screening, it is also clear that the real BGR is stronger than the BER, since the resulting effect of the competition of those two effects results in a redshift, :

$$\frac{E_{B_0}\alpha'_{QFC}}{\varepsilon_{r_{static}}} < E^{QFC}_{BGR} \tag{6.24}$$

Analogously, the opposite is true for the exciton dynamic screening where the competing effect result in a blue-shift of the excitonic resonance, thus:

$$E^x_{BGR} < \frac{E_{B_0}\alpha'_x}{\varepsilon_{r_{static}}} \tag{6.25}$$

Bringing now everything together, for the same absorbed photon density (i.e. $n_{QFC} = 2n_x$) density, under the previous assumption of $\alpha'_{QFC} > \alpha'_x$, we obtain:

$$E^x_{BGR} < \frac{E_{B_0}\alpha'_x}{\varepsilon_{r_{static}}} < 2\frac{E_{B_0}\alpha'_{QFC}}{\varepsilon_{r_{static}}} < 2E^{QFC}_{BGR} \tag{6.26}$$

This relation means that, considering always the presence of two QFC for every exciton as in the experiment, the real bandgap renormalization when excitons are present in the system is weaker than the corresponding exciton dynamic screening-induced binding energy reduction. The real exciton dynamic screening induced BER, in turn, is smaller than the corresponding QFC induced real BER. Ultimately the stronger effect is the QFC dynamic screening induced real BGR. Eq. 6.26 is obtaining similar conclusions derived in the case of negligible E^x_{BGR}. The discussion and conclusion just presented is also compatible with previously reported experiment and theoretical predictions [90, 30].

The relation of the relative strength of BER and BGR originating from QFC and exciton screening is also an important result. This in fact explains the different quasiparticle dynamic screening nature of the two quasiparticle species. Nevertheless, the assumptions in this discussion require confirmation. Further experiments that measure the single real BER or BGR contributions are needed to confirm such predictions.

The clear conclusion though from our data is that when QFC are present in the system, the real BGR is stronger than the binding energy reduction effectively resulting in the redshift of the exciton. Instead, when excitons are present, the BER is the dominant mechanism, and the effective screening originating per exciton particle (E_x) results in a blueshift, stronger in magnitude with respect to the effective

BGR originating from the presence of a single QFC (E_{QFP}). Based on the argumentation reported in section 2.2.2 regarding the higher polarizability of the electron-hole plasma with respect to excitons, we could tentatively hypothesize that the absolute magnitude of BGR and BER could be smaller in the case of exciton screening with respect to the QFC counterpart. Further experiments must be performed to confirm this hypotesis, possibly with experimental techniques that are sensitive to either the free-particle bandgap or to the binding energy, such as tr-photoemission experiments.

This section showed how such an essential three-level model could unravel the contribution due to the presence of different quasiparticles transiently present in the system. The excellent agreement of the model with the extracted peak shift and linewidth broadening, supported by the agreement of the fit parameters with literature values, justified the assumptions made in the derivation of the model. Not only the role of the QFC in the dynamics was unravelled, but also the ones arising from the exciton and the temperature-induced effects. In particular, the presence of QFC in the system induces linewidth broadening of the excitonic resonance through QFC-exc scattering and an red-shift of the excitonic resonance that can be modelled with an effective bandgap renormalization. It was found that effectively the exciton screen more efficiently the Coulomb interaction resulting in a stronger blueshift then QFC induced red-shift per unit particle. Given the fact that the QFC are double the number of the excitons for same absorbed density, the comparably large effect of carrier screening on the free particle band gap is observed. Ultimately, this section shines light on the complex interplay of electronic and thermal processes contributing to the dynamical response of the exciton upon photoexcitation. The essential but comprehensive picture of the dynamical exciton response in a monolayer WS_2 is then reported in the following section, and the applicability of this model is discussed.

6.2.4 Discussion and Summary

Section 6.1 hypothesized that the dielectric environment influences the steady-state absorption spectra but not the time-dependent exciton response upon photoexcitation. The latter seemed to depend mainly on the excitation conditions, particularly on the initial photoexcited particle density. This suggested that the dynamic screening could be the main origin of the observed dynamics. The question that was posed at the beginning of this section on how different photo-excited quasiparticles influences the exciton dynamics and which relaxation mechanisms are involved after photoexcitation was answered in this section.

In summary, the formalism introduced in section 6.1 was applied to access and investigate the pump photon energy- and fluence-dependent exciton dynamic response of a monolayer WS_2 from time-resolved reflectance contrast measurements. In particular, excitons and quasi-free carriers were selectively excited in the system

by means of resonant/above-resonance optical pumping. The following recombination dynamics of the microscopical excited quasiparticles population and the lattice temperature were described with a two/three-level phenomenological model and related to the macroscopic optical observables of peak shift and linewidth broadening.

Sections 6.2.2 and 6.2.3 showed how both models confidently reproduce the exciton dynamic response upon resonant and above-resonance photoexcitation fully and including multiple crossover regions. The fit returned extracted parameters in good agreement with previously reported literature values. This implies that the models are based on appropriate assumptions and that the most essential mechanisms influencing the exciton non-equilibrium response are an accurate description of the dominating processes.

From this, it was revealed that the excited quasiparticle population governs the observed peak shift through dynamic screening and induces the linewidth broadening through scattering between the photoexcited quasiparticles. In particular, when photo-excited excitons are present in the system, an effective blueshift of the excitonic resonance modelled with a dynamic screening induced effective binding energy reduction is observed. Furthermore, exciton-exciton scattering is the main source of linewidth broadening. The QFC effects of the dynamics can be described with a different dynamic screening induced effective bandgap renormalization manifesting in a red-shift of the excitonic resonance. Moreover, the presence of QFC, through exciton-QFC scattering, induces a stronger broadening of the excitonic resonance when compared to exciton-exciton scattering.

The blue-shift and red-shift originating from the presence of excitons and QFC, respectively, originate from the competing effects of BER and BGR due to dynamic screening of the CIA occurring in both cases. The resulting effective exciton induced blueshift is stronger per unit of quasiparticle than the QFC induced red-shift. The presence of double the amount of QFC per excitons, for the same excitation density, explains the comparatively larger effect of the latter.

These results provide the most basic but still accurate and comprehensive picture of the competing phenomena that govern the exciton dynamic response in monolayers WS_2. Thus, these results are fundamental for the complete understanding of the non-equilibrium dynamics in TMDC and other 2D materials.

Regarding the applicability of the two/three-level model, for higher initial excitation densities, the phenomenological model described in this section loses reliability because of two reasons. Firstly, the excitation density gets closer to the Mott density when the excitons are densely packed, eventually forming the so-called electron-hole plasma. Secondly, when many excitons recombine through the Auger channel, it is not possible to neglect anymore the presence of QFC, also in the case of resonant pumping, for instance. This is due to the fact that when an exciton recombines through Auger scattering, another exciton is excited to a higher-lying state in the CB

for energy conservation reasons. At higher exciton densities, the Auger recombination becomes more and more the prominent recombination channel. In this situation, the fraction of excited excitons, which substantially are QFC, with respect to the total number will not be negligible anymore, and the corresponding contribution should be included in the model.

Nevertheless, for intermediate initial excitation densities, it was unravelled that the dynamic response of the exciton upon photoexcitation in WS_2 monolayer is mainly governed by the dynamic screening due to the presence of different quasiparticles. Dynamic screening effects compete with temperature-induced effects that, despite in minor part, are also essential in the dynamic exciton response of monolayer WS_2. Though I did not investigate the case of different static dielectric environments, and I did not either confirm or neglect the hypothesis that the static screening is not influencing the exciton dynamic response. The following section will try to prove one or the other option.

6.3 Dielectric environment role in exciton dynamic response

In section 6.1 I developed a formalism that allowed the extraction of the complex dielectric function of the monolayer WS_2 upon photoexcitation. The main conclusion of that section was the evidence that the static screening, particularly the environment's local dielectric disorder, influences the steady-state excitonic properties. This was not true for the dynamic response instead. The latter is governed principally by the excited quasiparticle population present in the system through dynamic screening and scattering, as carefully analyzed and explained in section 6.2. The latter section provided a model that quantitatively isolates the contribution of the dynamic screening of the excitons and QFC, QFC-exciton and exciton-exciton scattering, and also thermally induced effects. From the previous sections, though, It was not possible to discern if the *static* dielectric environment also influences the *dynamical* response of the exciton because of the very similar dielectric permittivity ε_{st} of the investigated samples. This exact question is the central question of this section.

In order to unravel an eventual correlation between the exciton dynamic response in monolayer WS_2 and the static dielectric screening, it is necessary to change the dielectric environment in which the monolayer WS_2 is placed. Sapphire is an ideal substrate because it has a higher relative permittivity than the FS. Furthermore, it is transparent and flat, offering an easy platform to transfer monolayer WS_2 onto.

I, therefore, investigate the pump fluence- and pump photon energy-dependent tr-TC of a monolayer WS_2 placed on a *sapphire* substrate. I extract the excitonic contribution to the dielectric function using the formalism introduced in section 6.1.3, and track its time evolution upon photoexcitation. The role of the quasiparticle dynamics, in terms of effective screening coefficient and excitation-induced broadening parameters, is then unravelled by using the phenomenological two/three-level models described in section 6.2. By quantitatively comparing the exciton dynamic response between the case of the sapphire substrate and the one on Si/SiO_2, the influence of the static screening on the exciton dynamical response is eventually found. Finally, the conclusion is that the linewidth broadening due to scattering is independent of the environment screening. Instead, the dynamic exciton screening changes for varying dielectric screening. On the contrary, the QFC screening is not as affected by the dielectric environment as the exciton screening.

Before proceeding with the analysis of the tr-TC experiments on the WS_2 monolayer on the sapphire, I would like to emphasize that section 6.2.2 compared the exciton dynamic response upon photoexcitation of two different samples. Those were both WS_2, but one placed on fused silica and the second one placed on a Si/SiO_2 substrate. The main conclusion of that subsection was that the dynamical response of the exciton could be reproduced with roughly the same parameters of the simplified phenomenological model in the two cases. This experiment can be seen as a

comparison of the exciton dynamic response between two different dielectric environments. In this case, the dielectric environment was just slightly different between the two samples, thus meaning that the local dielectric disorder does not influence the exciton dynamic response.

Ultimately, this section provides a prototypical example of applying both the formalism to extract the complex dielectric function of the monolayer WS_2 upon photoexcitation and the modelling of the exciton dynamic response with the simplified two/three-level model. The results reported in the following are not comparable in quality to the data reported in the previous sections, and to confirm the conclusions, further experiments need to be performed. Nevertheless, the conclusions of this section are preliminary results that provide the basis and guidelines for future experiments along the same research line.

6.3.1 Static dielectric screening vs exciton dynamic screening

From the theory chapter and section 6.1, it is known that the dielectric environment influences the steady-state excitonic response. However, from the previous chapter, it was not possible to draw any conclusion regarding the influence of the dielectric environment on the dynamical response. Therefore, it becomes necessary to investigate the dynamical exciton response of a monolayer WS_2 placed on a substrate with a different relative permittivity.

To do that, this section investigates the impact that the static dielectric screening has on the exciton induced dynamic screening. This is achieved by investigating the fluence dependence of the exciton peak shift and linewidth broadening extracted from the resonant pumping tr-TC experiments on a monolayer WS_2 placed on a sapphire substrate. Sapphire has a higher dielectric permittivity with respect to the fused silica. In particular the relative permittivity of the sapphire is ε_{static}=11 [149], roughly three times higher that the FS substrate. First, the exciton peak shift and linewidth broadening of the exciton upon photoexcitation are extracted employing the 2D linearized model introduced in section 6.1.3. I then fit the two-level model introduced in section 6.2.2 to compare the exciton effective dynamic screening and excitation induced broadening parameters between this experiment and the value obtained for the case of Si/SiO_2 obtained in section 6.2.2. Eventually, I demonstrate that qualitatively it is possible to reproduce the observed excitonic dynamical response with this model, and the discussion of the extracted parameters is postponed to section 6.3.3.

The tr-TC of a monolayer WS_2 placed on a sapphire substrate is investigated. The experimental configuration and the analysis of the static spectrum and for extracting the dynamical exciton evolution upon photoexcitation is the same as the case of the monolayer WS_2 placed on a FS substrate described in sections 6.1.1 and 6.1.3. The only differences are the values used for the dielectric function of the sapphire and fused silica substrate, which is taken from [150, 149]. Analogously, the absorbance of the monolayer placed on a sapphire substrate and the initial photoexcitation density

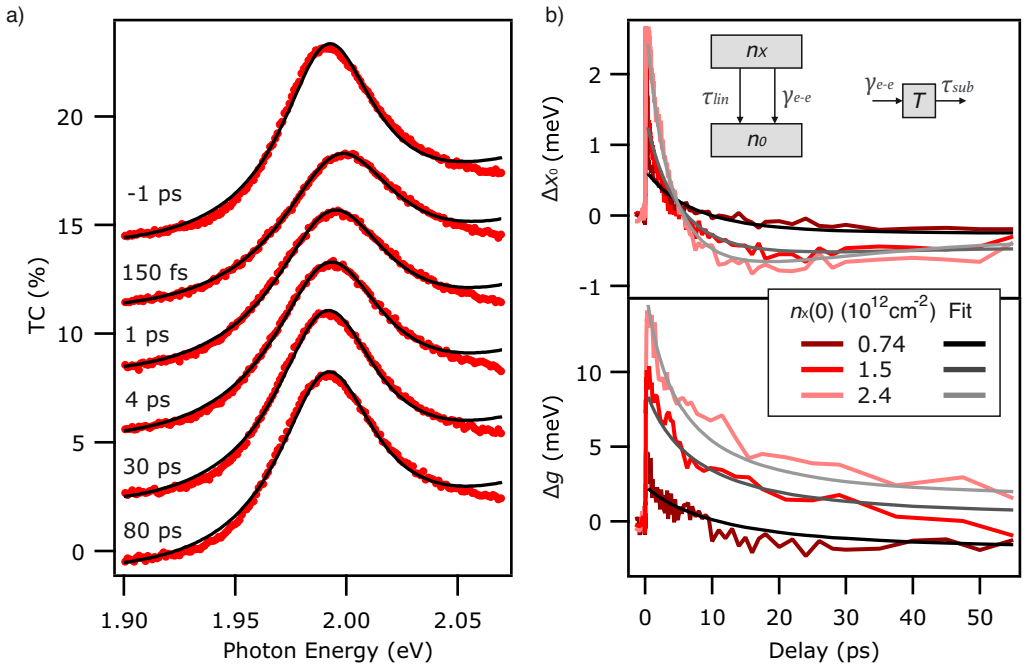

FIGURE 6.17: a) TC spectra (colored markers) as a function of photon energy for various selected delays and respective fits using the 2 linearized model (grey traces). The traces are vertically shifted for clarity. b) Exciton peak shift and linewidth broadening as a function of time delay for different fluence for resonant pumping of monolayer WS_2 placed on a sapphire substrate. Respective fits with Eq. 6.13 and Eq. 6.11

are calculated. This was achieved with the same method used for the fused silica substrate. The only difference is that the substrate dielectric function was changed to the sapphire one as described in detail in appendix B.

Fig. 6.17.a) reports the TC spectra for few selected delays as a function of the probe photon energy. The steady-state spectrum corresponds to the negative time delay one taken at -1 ps. In analogy to the fused silica substrate case, the observed peak in the spectra is attributed to the A exciton. It is evident that the resonance undergoes peak shift and broadening upon photoexcitation.

To quantify these effects, I make use of the formalism introduced in the case of TC of a monolayer WS_2 on a transparent substrate reported in section 6.1.1. Using a Lorentzian oscillator and the analytical expression of the TC spectrum given by the 2D linearized model [93], the exciton contribution to the complex dielectric function is quantified. This allows accessing the exciton resonance energy, linewidth and spectral weight. Finally, the same fitting procedure is applied to the spectra taken at different time delays, therefore tracking the evolution of the excitonic parameters upon photoexcitation.

Fig. 6.17.b) reports the exciton peak shift and broadening as a function of time delay for different fluences for the resonance pumping of a monolayer WS_2 placed on a sapphire substrate. It is seen that the overall trend of the observed dynamics qualitatively matches the observed dynamics described for the sample placed on Si/SiO_2 substrate reported in section 6.2.2. An initial blueshift of the exciton is observed, followed by a redshift of the resonance for later time delays. The linewidth broadening increases instantaneously with the pump and recovers to the equilibrium, the faster, the higher the excitation density.

I now extract quantitative information about the dynamic response of the exciton by making use of the two-level model developed in the previous section and sketched in the inset of Fig. 6.17.b). A global fit of the time-dependent exciton peak shift and linewidth broadening is performed with Eq. 6.13 and Eq. 6.11, respectively, in total analogy as the case of Si/SiO_2 or fused silica substrate reported in section 6.2.2. The fit parameters are left free to change with respect to the parameters obtained from the Si/SiO_2 substrate or fused silica cases, but those values are used as an initial guess for this global fit. In the case of the sapphire substrate, the relative effective permittivity of the dielectric environment is fixed to a value of ε_{st}= 6. This value is obtained by calculating the average of the dielectric permittivity of the air and the substrate according to $\varepsilon_{st} = (\varepsilon_{sub} + \varepsilon_{air})/2$. ε_{st} for the sapphire substrate is then higher than the SiO_2 value of 2.45, index of a more effective dielectric screening of the environment.

The best fits of exciton peak shift and linewidth broadening are reported in Fig. 6.17.b), showing a good agreement with the data. This agreement confirms that the dynamic response of the exciton energy can be explained with the binding energy reduction due to the dynamic screening originating from the presence of a density of photoexcited excitons in the system. Furthermore, the collisional broadening and,

more precisely, the exciton-exciton scattering seems to be the primary source of photoinduced broadening.

Ultimately this subsection used the formalism , introduced in 6.1.1 and 6.1.3, to extract the time-dependent exciton contribution to the complex dielectric function for the case of a monolayer WS_2 placed on a sapphire substrate. It was demonstrated that this method is accurate in tracking the time-dependent exciton response independently of the substrate of choice. Furthermore, the data are consistent with the two-level model, which ultimately captures the dynamic response of the exciton peak shift and linewidth broadening. This means that the photo-induced blueshift can be reproduced with an effective binding energy reduction, due to exciton dynamic screening. The scattering between excitons, leading to the photo-induced broadening is also captured from the model as the primary origin of the observed dynamics. The quantitative details of the model are also crucial to evaluate the accuracy of the latter, particularly to understand how the different permittivity of the substrate influences the dynamics. Before discussing the quantitative aspects of the extracted parameters, which are reported in section 6.3.3, it is necessary to investigate the role of the QFC on the dynamical exciton response upon photoexcitation.

6.3.2 Static dielectric screening vs QFC dynamic screening

In the previous subsection, I showed that, also for the case of a monolayer WS_2 placed on a sapphire substrate, the exciton dynamic response upon photoexcitation can be reproduced using the two-level model. Thus, the photo-induced peak shift can be modelled with an effective exciton binding energy renormalization due to exciton dynamic screening, which competes with thermal induced redshift. Furthermore, the collisional broadening due to exciton-exciton scattering is the primary source of linewidth broadening. Analogously to the monolayer on a SI/SiO_2 substrate case reported in section 6.2.3, I now investigate the effects on the exciton dynamical response originating from the transient presence of QFC.

I investigate the fluence dependence of the exciton peak shift and linewidth broadening of the monolayer WS_2 placed on the sapphire substrate in the case of the above-resonance pumping. Fitting the simplified three-level model, introduced in section 6.2.3, allows the isolation the role of the QFC in the observed dynamics. Ultimately it is qualitatively demonstrated that the transient presence of a QFC density induces a redshift of the exciton, modelled with bandgap renormalization, and the QFC-exc scattering introduces an additional linewidth broadening mechanism to the exc-exc scattering.

I investigate the tr-TC of the same monolayer WS_2 placed on the sapphire substrate measured in the previous subsection. In the case of the above-resonance pumping, the pump photon energy is tuned at 3.1 eV photon energy. The procedure used to extract the time-dependent exciton energy and linewidth of the exciton resonance is analogous to the resonant case reported in section 6.3.1.

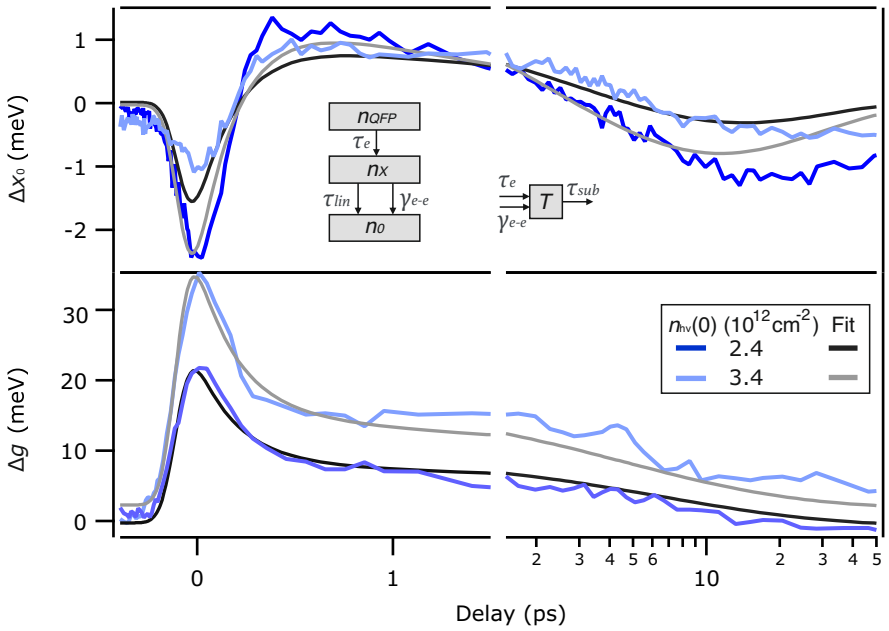

FIGURE 6.18: Exciton peak shift and linewidth broadening as a function of time delay for different fluence for above-resonance pumping experiment on a monolayer WS_2 placed on a sapphire substrate, with respective fits with Eq. 6.18 and Eq. 6.17

Fig. 6.18 reports the exciton peak shift Δx_0 and linewidth broadening Δg as a function of time delay for two different fluences upon above-resonance photoexcitation. The excitonic resonance shows a more complicated dynamical response with respect to the resonant pumping case, but qualitatively similar trends as the experiment performed on the monolayer placed on a Si/SiO_2, shown in section 6.2.3. It is seen that the overall trend of the observed dynamics qualitatively matches the observed dynamics described for the sample placed on Si/SiO_2 substrate reported in section 6.2.2. Particularly the initial redshift, rapidly turning in the blueshift, and a stronger linewidth broadening of the excitonic resonance for early time delays are observed signs of the presence of QFC in the system as observed in the Si/SiO_2 experiment.

A global fit of $\Delta x_0(t)$ and $\Delta g(t)$ using the phenomenological three-level model, described in section 6.2.3 and sketched on the inset of Fig. 6.15, is performed. The common parameters of the three-level model with the two-level model are fixed at the values extracted from the previous section in the case of resonant pumping.

The best fits are reported in Fig. 6.18, in agreement with the data, thus allowing us to conclude that the simplified three-level model is a good approximation also for the case of the dynamical response of the exciton for the monolayer WS_2 placed on the sapphire substrate. Notably, the early stage extracted dynamics of the exciton peak shift and linewidth broadening can be modelled with a bandgap renormalization induced redshift and a QFC-exc scattering induced broadening mechanism.

Together with the previous subsection, these results confirm that the simplified

two/three-level model is, at least qualitatively, accurate in tracking the excitonic dynamical response of a monolayer WS_2 upon photoexcitation. The model's validity lasts for different fluences, excitation conditions, and dielectric environments. In particular, these simplified models isolate the effects originating from the transient presence of different quasiparticles in the system and unravel the electronic and thermal effects that lead to the observed dynamics.

It is still unclear how the static screening influences the dynamical exciton response, and this question will be answered in the following subsection by analyzing the quantitative results and parameters of this fit.

6.3.3 Discussion

After presenting the global fit with the phenomenological two- and three-level model to the resonant and above-resonance pumping exciton dynamics of a monolayer WS_2 placed on a sapphire substrate, I can now answer the question if the static dielectric environment influences the exciton dynamical response.

To answer this question, this subsection reports the best-fit parameters that approximate the exciton dynamics in the case of the sapphire substrate, which are then compared to the ones extracted in the case of Si/SiO_2 substrate, obtained in section 6.2.3. By comparing the extracted best-fit parameters of the two/three level model for the monolayer WS_2 placed on sapphire and Si/SiO_2substrates in Table **??**, it is determined that the broadening dynamics are not affected by the static dielectric permittivity of the environment. This means that the exc-exc and QFC-exciton induced broadening parameters D and K are independent of the dielectric environment. Thus, considering the collisional scattering scenario, implies that the scattering probability of exciton-exciton and/or QFC, is independent of the substrate dielectric screening. Instead, it was found that the exciton dynamic screening seems to have a dependence on the static dielectric screening, particularly showing a higher effective dynamic screening for higher permittivity of the substrate. On the contrary, the QFC screening seems to be independent of it.

I now investigate the resulting parameters extracted from the global fits performed in sections 6.3.1 and 6.3.2. The parameters are reported in the following table, and they are compared with the parameters extracted in the case of the monolayer WS_2 placed on a Si/SiO_2 substrate, shown in section 6.2.3.

With regard to the timescales of the quasiparticle relaxation processes, all the timescales of the different relaxation processes are in agreement with each other. Particularly, the timescale of the electronic relaxation processes for the exciton formation time, the linear recombination channel and the Auger scattering rate are comparable also in the two experiments. Especially the agreement of the Auger scattering rate is surprising, considering that it was reported that such value could vary depending on defect density and substrate of choice [65]. The time constant τ_{sub} for the thermal energy transfer to the substrate, and the relative coefficient of proportionality β, are also confident within the two reported experiments. The agreement of all those

	Si/SiO_2 ε_{st}=2.45	Sapphire ε_{st}=6	Unit meas.
τ_{lin}	18 ± 5	23 ± 5	ps
γ_{e-e}	0.07 ± 0.01	0.07 ± 0.02	cm^2/s
τ_e	200 ± 10	210 ± 10	fs
τ_{sub}	14 ± 8	20 ± 10	ps
β	(0.4 ± 0.2)	(0.4 ± 0.2)	meV/K
α	$(6.6 \pm 0.6)\ 10^{-15}$	$(2.9 \pm 0.5)\ 10^{-14}$	cm^2
E_{QFC}	$(1.2 \pm 0.1)\ 10^{-12}$	$(1.0 \pm 0.1)\ 10^{-12}$	meV cm^2
D	$(5.6 \pm 0.2)\ 10^{-12}$	$(5.3 \pm 0.2)\ 10^{-12}$	meV cm^2
K	$(9.8 \pm 0.2)\ 10^{-12}$	$(9.9 \pm 0.2)\ 10^{-12}$	meV cm^2

TABLE 6.6: Comparison of Two/three-level model best fit parameters for two monolayers WS_2 placed on different substrates

parameters with the ones extracted Si/SiO_2, which were already proven to be confident with previously reported literature values, suggests that such a basic model, restricted to the most fundamental interactions can quantitatively track the exciton dynamic response upon photoexcitation also for different dielectric environment.

From this we can draw the conclusion regarding the effect of screening and scattering on the dynamical exciton response upon photoexcitation by analyzing the remaining parameters that were not discussed yet.

In order to do that it is important to specify that, as it was mentioned in the previous section 6.2, the main result of our simplified phenomenological model is the isolation of the effects due to the presence of different quasiparticles in the broadening kinetics and the peak shift. I now summarize the effects due to the transient presence of excitons and QFC in the system for the two different dielectric environments through the analysis of the remaining parameters. Regarding the linewidth broadening, the excitation induced broadening parameters for the two experiments shows a stunning agreement between the parameters D and K. This implies that the QFC-exc and exc-exc scattering rates that lead to the observed broadening are independent of the static dielectric environment. This allows to conclude that the photo-induced broadening dynamics are independent from the dielectric environment. Particularly, the scattering probability between photoexcited excitons or QFC and excitons is not affected by a more screened environment.

On the other hand, despite the independence of the broadening dynamics from the static dielectric environment, the situation is quite different regarding the peak shift. Before comparing the effective screening parameters α and E_{QFC}, it is necessary to spend some words regarding the equilibrium binding energy. The two/three-level model provides an estimation of the equilibrium exciton binding energy. It is crucial to note that such value comes simply from parameters of the model which are arbitrarilly fixed and do not result from the fitting. Precisely the parameters that determine the equilibrium binding energy are the r_0, fixed to 1 nm,corresponding to the exciton Bohr radius[6], and to the ε_{st}. It is evident that in the case of a monolayer WS_2 placed on a sapphire substrate, the calculated value of $E_B(eq)$=0.24 eV is smaller

than the value obtained in the case of Si/SiO_2 of $E_B(eq)$=0.58 eV. Such different values for the equilibrium binding energy are easily explained in the theory chapter, section 2.2.1, and in literature [78]. Despite the binding energy in our model result from a simplified treatment of the Coulomb interaction between the electron and the hole constituting the exciton, the trend of smaller binding energy for higher substrate dielectric permittivity just mentioned is respected. A higher permittivity of the dielectric environment screens more efficiently the Coulomb interaction between the electron and the hole constituting the exciton, therefore leading to a lower exciton binding energy. Furthermore, the screening induces a quasi-free particle bandgap renormalization due to screening of the repulsive Coulomb interaction. The equilibrium exciton resonance energy tends to be similar because the two effects tend to cancel out.

After this, I can now discuss the effective screening parameters. When comparing the parameter E_{QFC} in the two experiments, corresponding to the effective QFC induced bandgap renormalization, it is observed that the two values are confident with each other. Instead, in the case of exciton induced binding energy reduction, the parameter α is different in the two experiments.

This result is puzzling. In fact, a facto of five difference in the parameter αs implies that for the same amount of excitons in the system. This would initially lead to the suspect that the binding energy reduction is more efficient in the case of higher dielectric permittivity. Unfortunately, this dependency is not straightforward since the change in binding energy depends also on the effective static dielectric permittivity of the environment ε_{st}. On the contrary, the effective bandgap renormalization used to model the red-shift of the exciton resonance, when QFC are present in the system, occurs with the same amplitude independently of the static dielectric screening, as shown by the comparable values of E_{QFC}. Before reaching to a conclusion, though, it is possible to investigate further the different parameters α for the two different substrates. As it was done at the end of subsection 6.2.3 we linearize the ΔE_B, provided the satisfied condition of $\alpha n_x(t) \ll \varepsilon_s$. In this case, recalling the formula 6.19 we have an effective exciton induced blueshift for the case of the sapphire substrate equal to $E_{x_{sapph}} = (1.2 \pm 0.2)\ 10^{-12}$ meV cm^2. This value must be compared to the corresponding value for the Si/SiO_2 substrate of $E_{x_{Si/SiO_2}} = (1.6 \pm 0.1)\ 10^{-12}$ meV cm^2. Those last two values despite not being confident with each other are much more similar that the two extracted parameters α. Interestingly, those values evidence that the competing effect of exciton BER and BGR results in an absolute blue-shift of the resonance which is lower in the case of the sapphire substrate than for the corresponding Si/SiO_2 counterpart. Now the last conclusion might sound contradicting the fact that the parameters alpha show the opposite trend. This is easily explainable by recalling the expression of E_x, as shown in the following.

$$E_x = \frac{E_{B_0}\alpha}{\varepsilon_{r_{static}}} = \frac{e^2}{4\pi\varepsilon_0\varepsilon_{r_{static}}}\frac{\alpha}{\varepsilon_{r_{static}}r_0} \tag{6.27}$$

By investigating the first equality, it becomes clear how, when dividing the parameter α by $\varepsilon_{r_{static}}$, the absolute magnitude of the blue-shift in the two cases becomes comparable, even though the different values of α. Therefore, despite a different coefficients α, the exciton induced blueshift is of a similar amount in the two substrates. The absolute magnitude of the peak shift is not such a good indicator for how effectively the exciton screening changes with varying dielectric environment. This is clear if we calculate the maximum percent ratio between BER and the equilibrium binding energy, specifically $E_x n_x / E_{B_0}$. In the case of the sapphire substrate, for an exciton density of $2\,10^{12}$ cm^{-2}, the effective blue-shift with respect to the equilibrium binding energy would be 1% and 0.5% for the case of the Si/SiO_2 substrate. Those two values confirm that the effective excitons dynamic screening is more efficient in the case of higher substrate dielectric constant.

To explain this last result, the difference can tentatively be attributed to the fact that, with the sapphire substrate, the more effective screening leads to lower exciton binding energy, meaning more delocalized excitons, as discussed in section 2.2.1. Therefore, the exciton radius is higher in the case of the WS_2 placed on a sapphire substrate with respect to the one placed on the Si/SiO_2. Such consideration does not affect the screening of the QFC, which are not influenced that drastically by the substrate of choice. The phenomenological two/three-level models does not include the dependency of the Bohr radius of the exciton on the static dielectric permittivity due to the complexity of the subject matter. Instead, a Bohr radius of the exciton in both cases to be equal to 1 nm was assumed. Intuitively when the radius of an exciton is higher, the electric field lines extends over a wider area, thus screening more effectively the other excitons in its proximity. This could therefore explain the higher value of the parameter α.

In our two/three-level model we fixed the value of r_0 arbitrarily but, when considering Eq. 6.27 it can be seen that the actual fit parameter α could be changed to α / r_0. A higher value for r_0 would imply a lower value for α, thereby confirming the hypothesis of larger exciton in more effectively screened environments.

This conclusion must be interpreted as a hypothesis. In fact, to the author's knowledge, an explicit dependency of the exciton Bohr radius on the dielectric permittivity of the surrounding has not been reported. Moreover, the estimation of the spatial extension of the exciton is not directly measurable with our experimental techniques. Further measurement with techniques which are sensitive to the spatial extension of the exciton are required to further clarify this and shine light on the competition between higher screening or larger Bohr radius of the exciton for more effectively screened environment.

Systematic studies of the exciton dynamic screening as a function of the dielectric permittivity of the environment are then needed. This would properly determine the influence of the static dielectric screening on the exciton dynamical response.

It can be concluded that the linewidth broadening dynamics do not depend on

the static dielectric screening but only on the presence of quasiparticles in the system through scattering. The QFC screening also does not depend on the dielectric environment, but on the contrary, it is evident that the exciton-induced screening depends on it. However, this does not preclude the validity of the result from section 6.1. There, it was hypothesized that the exciton dynamic response does not depend on the dielectric environment, but only on the excitation conditions. The variation of relative permittivity due to local dielectric disorder between the FS and Si/SiO_2 substrate had negligible influence on the exciton dynamical response. In fact, both cases were reproduced using the two-level model with the same value of effective relative permittivity $\varepsilon_{r_{st}}$ of the dielectric environment.

Summarizing, in this subsection, the best-fit parameters of the two/three-level model used to reproduce the exciton dynamics of a monolayer WS_2 are compared for two different dielectric environments. The first finding is that the lifetimes of the different quasiparticles relaxation processes are independent of the dielectric environment. Secondly, I found exc-exc and QFC-exciton scattering are independent of the dielectric environment. I finally found that the exciton dynamic screening seems to depend on the static dielectric screening and, on the contrary, the QFC screening is independent of it. This is tentatively attributed to the higher degree of delocalization for the exciton in a more effectively screened environment.

6.3.4 Summary and outlook

The question posed at the beginning of this section was if it would be possible to discern if the static dielectric environment influences the dynamical response of the exciton upon photoexcitation. This exact question would be then the central question of this section.

To evaluate and eventual role of the static dielectric screening in the dynamical exciton response, the pump fluence energy-dependent tr-TC of a monolayer WS_2 placed on a sapphire substrate was investigated. Furthermore, this section provided a case study using the formalism developed in the first two sections to investigate the exciton dynamic response of a monolayer WS_2 upon photoexcitation.

By using the formalism described in section 6.1, I extracted the excitonic contribution to the dielectric function upon photoexcitation. Eventually, the role of the different quasiparticles was isolated by fitting the phenomenological two/three-level models described in section 6.2. This allowed ultimately the unravelling the effective screening coefficient and excitation induced broadening parameters. Through the quantitative comparison of the parameters describing the exciton dynamical response of a monolayer WS_2 on a sapphire substrate and on Si/SiO_2, the influence that the static dielectric environment has on the exciton evolution upon photoexcitation was found. In particular, The conclusion is that the QFC-exc and exc-exc scattering, leading to the observed linewidth broadening, are independent of the static screening. Instead, the dynamic screening originating from the transient presence of exciton changes for varying dielectric screening. Instead, the QFC induced dynamic

screening is not changing as drastically depending on the dielectric environment as in the case of the exciton dynamic screening. This difference was attributed to the higher degree of delocalization of the exciton typical of dielectric environments with higher effective permittivity.

To further prove this theory, further measurements are needed. Those experiments would be beneficial to further clarify the effective dependence or independence of the QFC induced dynamic screening on the dynamic screening. Even more, a systematic study of the quasiparticle induced dynamic screening as a function of the effective dielectric permittivity would provide further insight on how the exciton induced dynamic screening changes with the environment. Ulterior implementation of an explicit phenomenological dependency of the exciton screening coefficient α on the static dielectric permittivity ε_{st} also have fundamental importance towards the understanding of the complex dynamics of the exciton upon photoexcitation.

However, the conclusion of this section provides the basis and fundamental insights towards the understanding of the complex topic of the role of the screening in 2D TMDC materials, as summarized in the following chapter.

Chapter 7

Conclusion and outlook

This chapter summarizes and draws the conclusion of the work done in this thesis. In the introduction, and chapter 5, I formulated the questions that this work tries to answer. Those questions are shown in the following:

- How do we extract quantitative information about the static and dynamic exciton response that also allows the comparison between different experiments, measurement techniques, samples, and substrate of choice?
- Which are the different relaxation mechanism that governs the recovery of the system after photoexcitation?
- How do the static and dynamic screening of the Coulomb interaction play a role in the exciton dynamic response upon photoexcitation, and how do they compete with the other phenomena?
- How do different quasiparticles (i.e. excitons and QFC) dynamically screen the Coulomb interaction, therefore contribute to the energetic structure renormalization of the exciton in TMDC?
- How do static and dynamic screening compete in the determination of the exciton response upon photoexcitation?

In the previous chapter, it was shown how, by investigating the pump energy and fluence dependence of the tr-RC/TC of monolayers WS_2 placed on various substrates, it is now possible to answer these questions. It was demonstrated that by describing the exciton contribution to the dielectric function with the Lorentz model, combined with either the 2D linearized model [93] of a Fresnell transfer formalism [92, 91] it is possible quantitatively extract the steady-state and dynamic exciton contribution to the dielectric function in the WS_2 response. This approach provides quantitative tracking of the excitonic resonance independently of the sample, measurement technique, substrate and excitation conditions. Therefore, these formalisms allow the reliable comparison, within the accuracy of the excited particle density determination, of the results between different experiments not only in this work on monolayer WS_2 but also for other two-dimensional semiconductors. This finding serves as the foundation for all the results reported in this work and for future studies, promising the reliable comparison of different experiments.

By applying these formalisms, it was possible to extract the excitonic resonance peak shift, linewidth broadening, and spectral weight variation as a function of time delay upon various photoexcitation conditions for a monolayer WS_2 placed on various substrates. The QFC and exciton population dynamics were described with a very basic two/three-level model, which was used to reproduce the non-equilibrium response of the exciton resonance upon photoexcitation. The model accurately reproduced the experimental data, also providing parameters in excellent agreement with the literature values. This agreement justified the assumptions used in the derivation of the model, thus their validity.

This approach allowed the isolation of the competing relaxation mechanisms that contribute to the recovery of the system to the equilibrium after an excitation. It was shown that, upon above resonance photoexcitation, a quasi-free carrier population is generated in the system, which quickly relaxes forming exciton on a timescale of roughly 200 fs. Excitons then recombine through two recombination channels, one linear and a quadratic one in the exciton density, with the second one being attributed to the non-radiative Auger recombination. The competition of the two relaxation channels for the exciton is fundamentally important since the Auger recombination sets a limit on the excitons that recombine through the linear channel. Furthermore, the presence of the non-radiative recombination channel implies the transfer of energy from the electronic system to the phonon bath, eventually increasing the lattice temperature of the monolayer. The presence of this channel then has a strong implication in the application of monolayer TMDC in devices, where the increase in temperature must be avoided in order to increase the efficiency of potential devices. Ultimately, the two/three-level model provides the first comprehensive picture, despite it being restricted to the most essential mechanisms, of the quasiparticles relaxation pathways and their interplay in the recovery of the system back to the equilibrium after photoexcitation, thereby answering the second question.

Moving forward to the third question on the role of the screening of the Coulomb interaction in the dynamics and the interplay with other phenomena such as thermal effects, phase-space-filling, and scattering. This work showed that, with the same two/three-level model, it is possible to isolate the different contributions of the aforementioned phenomena governing the exciton dynamical response. Specifically, the exciton dynamical response is governed mainly by the excited state population. In particular, the peak shift originates from the dynamic screening of the Coulomb interaction due to the transient presence of excited quasiparticles. Other effects, such as phase space filling effects, are negligible in the case of monolayer WS_2 at the initial photoexcitation densities used in this work. Thermal effects are not negligible in the exciton dynamic response instead. In fact, due to the presence of the Auger non-radiative recombination channel or to the relaxation of hot QFC in the conduction band forming excitons, some of the energy deposited in the system with the pump pulse is converted into heat, thus increasing the lattice temperature. This leads to a red-shiftred-shift of the excitonic resonance on a picosecond timescale, eventually

dominating the peak shift dynamics in later stages. Furthermore, it was unveiled that the broadening of the excitonic resonance is due to scattering between photoexcited quasiparticles in a collisional scattering scenario. Thermal effects do not significantly affect the linewidth broadening of the excitonic resonance.

The key finding of this work is the isolation of the excitons or QFC specific effective impact on the exciton dynamics. Tracking the populations of the photoexcited exciton and QFC separately as a function of time delays after photoexcitation allowed the determination of the various effects originating from the transient presence of one or the other quasiparticle species. Specifically, QFC induce a global red-shift of the exciton resonance, which can be reproduced with an effective QFC dynamic screening induced bandgap renormalization. Furthermore, QFC-exciton scattering is the dominant linewidth broadening mechanism when QFC are present in the system. Excitons, instead, induce linewidth broadening of the excitonic resonance through exc-exc scattering and a blue-shift, which can be reproduced with an exciton effective binding energy reduction due to dynamic screening.

Insights into the quasiparticle specific dynamic screening also resulted from this thesis. In fact, it is important to consider that the model does not capture the real changes of the binding energy and bandgap but the resulting effect from the competition between the two. Particularly, as it was shown in the literature, both exciton and QFC induce simultaneous binding energy reduction and bandgap renormalization. The model presented in this thesis provides the quantitative detail of their resulting effect. Specifically, the competition of the real BGR and BER due to QFC effective dynamic screening results in a red-shift which is minor than the exciton induced blue-shift for the same excited quasiparticle density. Considering the double amount of QFC with respect to excitons for the same absorbed photon density, though, the comparably larger effect of a QFC density on the exciton peak shift is explained. Moreover, under the assumption that the QFC screen the Coulomb interaction more effectively than excitons due to the localized nature of the latter and their minor polarizability, I retrieved the relative strength of the single BER and BGR contributions. The main conclusion is that, for the same absorbed photon density, the QFC induced quasi-free particle bandgap renormalization is the stronger effect, followed by the QFC induced binding energy reduction, exciton induced binding energy reduction and exciton induced bandgap renormalization.

Finally, it is possible to the static and dynamic screening role in the exciton steady-state and dynamic response. The static screening, due to the dielectric environment in which the WS_2 monolayer is placed, determines the steady-state excitonic properties of the material. Although some changes in the absolute exciton resonance energy are observed for substrates with the same dielectric permittivity and attributed to local dielectric disorder, it was hypothesized that the non-equilibrium response, at least for a small variation of the dielectric environment, does not depend on the static dielectric screening. Instead, the dynamic exciton response is

mainly governed by the dynamic screening due to the excited quasiparticles population. This last hypothesis was proven to be correct, as mentioned in the previous paragraphs and by isolating the dynamic screening contribution due to the different quasiparticle species.

Regarding the influence of the static screening, the final conclusion is that the broadening dynamics are independent of the environment dielectric screening, meaning that the QFC-exciton and exciton-exciton scattering do not depend on the effective dielectric permittivity of the substrate. Also, the effective QFC screening induced bandgap renormalization does not show any explicit dependence on the dielectric environment screening. Instead, the exciton dynamic screening induced binding energy reduction depends on the dielectric constant of the substrate, and it increases by increasing the effective dielectric permittivity of the environment. Such effect is tentatively attributed to the higher degree of delocalization of the exciton when placed in a more effectively screened environment that leads to a more efficient dynamic screening of the Coulomb interaction. Therefore, it is not possible to conclude that the static dielectric screening of the CIA does not influence the dynamic response of the exciton, as suggested at the end of section 6.1. However, the more precise conclusion is that in case of minor variation of the dielectric environment, such as the case of FS sample and Si/SiO_2 substrate or local dielectric disorder, the effect of a different dielectric permittivity of the environment on the exciton dynamic response can be neglected as shown by the conclusion of section 6.1. Instead, for more substantial variation of the dielectric environment, such as the comparison between the sapphire substrate and fused silica, the exciton dynamic screening depends on the static dielectric screening.

From the evidence that the exciton dynamic screening depends on the dielectric environment, it is easily possible to connect to the outlook of this work. In fact, it naturally follows that the first question arising from the conclusion is: how does the exciton dynamic screening change as a function of the static dielectric environment? To answer this question, a systematic study of the exciton dynamic screening as a function of the environment's effective dielectric constant must be carried out and accompanied by a relative modelling of the spatial extension (i.e. Bohr radius) of the exciton.

Regarding the relaxation channels of the quasiparticles, the nature of the linear recombination channel could not be determined in the framework of this thesis. Nevertheless, it is notable that a contribution of this recombination channel to the temperature increase did not need to be included in the model, suggesting radiative electron-hole recombination or trapping of the exciton. An eventual femtosecond time-resolved photoluminescence upconversion experiment could prove the nature of such a recombination process, determining if this is an ultrafast radiative process or not.

Another important aspect to univocally understand the complex non-equilibrium

physics of these materials, and to stimulate further directions of research, is the extension of the model to higher initial photoexcitation densities. In fact, the two/three-level model proposed in this work becomes inaccurate in the case of high initial photoexcited quasiparticle density, mainly due to the prevalence of exciton recombination through the Auger channel. This means that transiently, for every exciton that recombines through Auger recombination, another one is promoted to the QFC state. In the case of low fluence, as the one investigated in this work, such contribution is negligible but not in the case of higher fluences. To include this effect, the rate equation model of the two/three-level system must be changed, adding a quadratic filling term for the QFC state from the excitonic level. This approach could also extend the range of validity of the model for higher initial excitation densities, eventually up to the Mott threshold density.

The last question that arises from our conclusion is about the validity of the proposed two-three level model for other TMDC materials. If, for the case of the dielectric function determination presented in section one of the result chapter, the applicability is quite vast, possibly extending to every 2D material, this might not be the case for the two/three-level model. For the case of WSe_2 monolayers, considering the really similar physics of the latter with the WS_2, the reliability of this model to describe the exciton dynamics upon photoexcitation is most likely granted but still needs confirmation. However, this might not be the case for the exciton's dynamic response in Mo-based TMDC, where the lower conduction band at the K point is the bright exciton transition. Thanks to this, an eventual addition of a phase-space-filling contribution to the dynamics might be needed to correctly reproduce the exciton dynamic response, thus rendering the investigation of the applicability of this model to Mo-based TMDC intriguing.

Nevertheless, this work provides a simple but still accurate, comprehensive picture of the competing phenomena that govern the exciton dynamics in WS_2 upon photoexcitation, unveiling the role of the static and dynamic screening of the Coulomb interaction in determining the steady-state and dynamic exciton response, which is fundamental for the univocal understanding of the non-equilibrium dynamics in TMDC and other 2D materials.

Appendix A

Analytical expressions of the microscopic quantities for the two-level model

$$n_x(t) = \frac{n_x(0)}{e^{\frac{t}{\tau_{lin}}} - \gamma_{e-e}\tau_{lin}n0 + e^{\frac{t}{\tau_{lin}}}\gamma_{e-e}\tau_{lin}n_x(0)} \tag{A.1}$$

$$\begin{aligned} T(t) = &\frac{h\nu_x}{d\rho c_p \gamma_{e-e}^2 \tau_{lin}} e^{-\frac{t}{\tau_{sub}}} \left(1 + \gamma_{e-e}\tau_{lin}n_x(0)\right) + \Bigg(G - \frac{e^{\left(\frac{1}{\tau_{sub}} + \frac{1}{\tau_{lin}}\right)t}\gamma_{e-e}}{-\gamma_{e-e}\tau_{lin}n_x(0) + e^{-\frac{t}{\tau_{lin}}}\left(1 + \gamma_{e-e}\tau_{lin}n_x(0)\right)} \\ &+ \frac{1}{(\tau_{lin} + \tau_{sub})n_x(0)} \Bigg(Hyp2F1\left[1, \frac{\tau_{lin} + \tau_{sub}}{\tau_{sub}}, 2 + \frac{\tau_{lin}}{\tau_{sub}}, 1 + \frac{1}{\gamma_{e-e}\tau_{lin}n_x(0)}\right] \\ &- e^{\left(\frac{1}{\tau_{sub}} + \frac{1}{\tau_{lin}}\right)t} Hyp2F1\left[1, \frac{\tau_{lin} + \tau_{sub}}{\tau_{sub}}, 2 + \frac{\tau_{lin}}{\tau_{sub}}, 1 + \frac{e^{\frac{1}{\tau_{lin}}}\left(1 + \gamma_{e-e}\tau_{lin}n_x(0)\right)}{\gamma_{e-e}\tau_{lin}n_x(0)}\right] \Bigg) \Bigg) \end{aligned} \tag{A.2}$$

Appendix B

Calculation of absorbance and excited quasiparticle density

The initial photoexcited quasiparticle density is a fundamental parameter that determines the recovery dynamics of monolayers WS_2 upon photoexcitation, as clearly demonstrated in chapter 6. This quantity is determined by the absorbed photon density and its calculation requires great care, especially when 2D TMDC monolayers are investigated.

This appendix describes the methods used to calculate the absorbed photon density from a monolayer WS_2 placed on fused silica (FS), Si/SiO_2, and sapphire substrate, respectively, and for two different pump photon energies, precisely of 2 eV and 3.1 eV, used troughout this work. For an accurate determination of the absorbed photon density, the effective absorbance of the monolayer WS_2 at the corresponding energy range, and for the specific sample, must be calculated.

In the following, we first outline the calculation of the initial photoexcited quasiparticle density for resonant pumping, then moving forward to the same calculation for above-resonance pumping. We start by accurately determining the initial photoexcitation density for the case of resonant pumping by calculating the effective absorbance of the sample in the proximity of the exciton for the monolayers placed on the different substrates.

Generally, due to the excitonic absorbtion resonance in monolayer WS_2 a slight variation of pump photon energy can lead to consistent changes in the absorbed photon density and, therefore, consistent differences in the initial excited particle density. Even more, the absorbtion due to the exciton can significantly vary depending on sample, substrate and even different spots within the same samples due to impurities or absorbates due to effect of local dielectric disorder.

To accurately determine the absorbed photon density of the monolayer WS_2, and include all the above mentioned effects, we proceed differently according to the substrate where the monolayer is placed onto. For the monolayer deposited on a transparent FS substrate, we calculate the absorbance of the WS_2 sample starting from the dielectric function extracted from the steady-state TC fit, described in section 6.1.2, and making use of the 2D linearized model [93]. The analytical formula of the

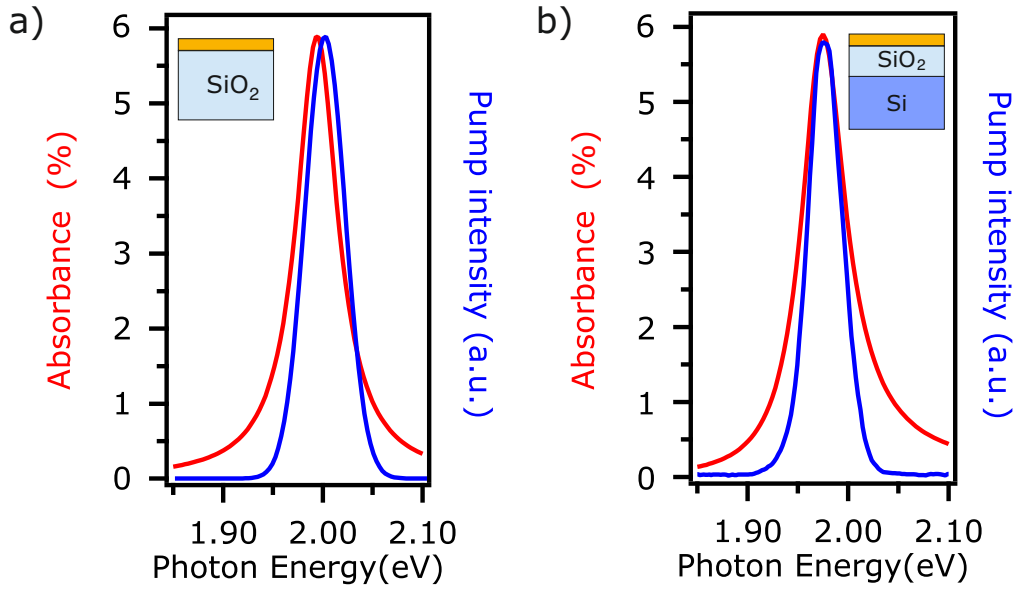

FIGURE B.1: a)Absorbance of monolayer WS_2 deposited on a FS substrate (red trace) as a function of photon energy, calculated using Eq. B.1. Pump spectra (blue trace) as a function of photon energy. b) Selective absorbance of monolayer WS_2 deposited on a layered Si/SiO_2 substrate (red trace) as a function of photon energy, calculated using a Matlab script. Pump spectra (blue trace) as a function of photon energy.

absorbance is given by [93]:

$$A = \frac{4}{|\,1 + n_{sub}\,|^2}\,[-i2\pi(\varepsilon_{WS_2} - 1)(d/\lambda)] \tag{B.1}$$

where n_{sub} and ε_{WS_2} are the complex refractive index of the substrate and the complex dielectric function of the monolayer WS_2, respectively. d is the thickness of the monolayer and λ the wavelength.

The dielectric function of the monolayer WS_2 is given by the Lorentzian with the parameters extracted from the fit to the steady-state TC spectra and reported in Section 6.1.1 and the refractive index of the fused silica is taken from literature [118]. The absorbtion spectrum, calculated with Eq. B.1, is shown in Fig. B.1. a). In this graph, we report the absorbance of the monolayer WS_2 on top of a thick substrate of fused silica (red trace) and the normalized pump spectrum (blue trace) as a funciton of photon energy. In the proximity of the excitonic resonance, a small shift of the pump photon energy, with respect to the exciton energy, could lead to a consistent differences in the effective absorbance. As previously mentioned, to accurately determine the absorbed photon density it becomes fundamental to compare the optical pump spectra to the absorbance spectra. In particular, the effective absorbance (i.e. the number of photons absorbed by the WS_2) is calculated by integrating, over the photon energy, the multiplication of the absorbance and the normalized pump lineshape. The latter procedure returns a value of 4.1% for the effective absorbance.

After determining the effective absorbance, the absorbed photon density is finally obtained by multiplying the incident fluence (0.025 mJ/cm^2) and the effective absorbance, returning a value of 3.2 E+12 cm^{-2}. The initial photoexcited quasiparticle density, for the resonant pumping case, corresponds to the absorbed photon density since, for every absorbed photon, an exciton is photogenerated in the system.

The procedure to calculate the absorbance, absorbed photon density and initial photoexcited particle density for the WS_2 monolayer placed on a sapphire substrate is analogous to the FS substrate, with the only difference that the n_{sub} is the refractive index of the sapphire, which is taken from literature [150].

After having established the method to accurately determine the initial photoexcited quasiparticle density for a monolayer WS_2 placed on FS or sapphire substrate, we move forward to the case of a monolayer WS_2 placed on the Si/SiO_2 substrate. In this case the the calculation of the initial quasiparticle density is more complicated because of the layered structure of the sample. As we already encountered in the main text in section 6.1.2, the reflections taking place at the multiple interfaces of the layered sample play a fundamental role in determining its optical properties, particularly influencing the selective absorbtion of the individual layers. To account for the multiple interfaces, we employed a Matlab script that allows the calculation of the selective absorption of a layer in a heterostructure, as introduced and discussed in detail by Jannin et al. in [94]. The script is based on the same transfer matrix formalism used in this text and extended to more general use for calculating optical observables of complex heterostructures starting from the dielectric functions of the constituents materials [91, 92]. Also in this case, in order to accurately accurately determine the local effective absorbance for the specific measurement, the script was modified to feed the dielectric function of the WS_2 given by the Lorentzian with the parameters retrieved in the fitting of the steady-state RC spectrum reported in section 6.1.2. The refractive index of silicon and fused silica instead were available in the library file of the script. The script, provided the geometry of the sample, calculates the WS_2 monolayer selective absorption and returns the absorption spectrum, which is reported as a function of photon energy in Fig. B.1.b) with the red trace. Analogously for the case of the transparent substrate, the normalized pump spectrum is shown also in the figure (blue trace). The procedure to calculate the absorbed photon density is then analogous to the case of the FS substrate. Specifically, the effective absorbance of the WS_2 layer is given again by integrating, over the energy, the multiplication of the absorbance and the normalized pump's lineshape. This returns a value for the effective absorbance of 4.6%. Finally, the absorbed photon density for the resonant pumping case of a monolayer WS_2 placed on a Si/SiO_2 substrate shown in section 6.1.2, is then given by the multiplication of the incident fluence (0.022 mJ/cm^2) and the effective absorbance returning a value of 3.1 E+12 cm^{-2}. The initial photoexcited particle density is again equal to the absorbed photon density.

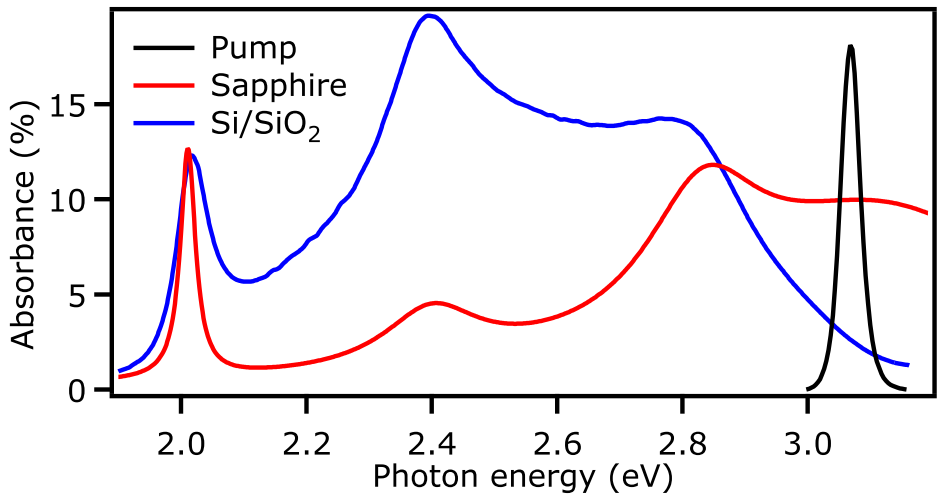

FIGURE B.2: a)Absorbance of monolayer WS_2 deposited on a sapphire substrate (red trace) as a function of photon energy, calculated using Eq. B.1 with literature values of ε_{WS_2}. Pump spectra (black trace) as a function of photon energy. Selective absorbance of monolayer WS_2 deposited on a layered Si/SiO_2 substrate (blue trace) as a function of photon energy, calculated using Matlab script from the literature value of ε_{WS_2}.

These two methods allow the determination of the initial photoexcited quasiparticle density, for the resonant pumping case, thanks to the accurate calculation of the effective absorbance in the energy range close to the excitonic resonance for different samples and different substrates.

Moving forward to the calculation of the initial photoexcited quasiparticle density in the above-resonance pumping case, the procedure and the assumptions are slightly different. Firstly, It is important to note that the UV absorbance of monolayer WS_2 is not affected particularly by the absorbtion from excitons, which for the WS_2 lay at lower photon energies. Therefore the absorbance of the monolayer WS_2 in the UV does not drastically depend on the dielectric screening of the environment and does not change drastically from sample to sample, or within different spots on the same sample due to dielectric disorder.

To estimate the absorbed photon density we need to determine the absorbance of the sample in the UV energy range. In this case pump, the probe pulse photon energy range used in this work does not extend up to the energy range around 3.1 eV. Therefore, we can not directly probe the absorbance in this spectral region. We turn then to make use of the fact that the absorbance is not sensitive to the dielectric environment in this energy range. Thus, for the monolayer WS_2 placed on a Si/SiO_2 substrate, we employ literature dielectric function for the monolayer WS_2 [117] and we feed the latter to the same Matlab script [94] used for the previous calculation of the absorbance in the proximity of the excitonic resonance, used in the resonant pumping case. This returns the WS_2 layer selective absorbance spectrum, shown in Fig. B.2 with the blue trace.

In the case of the sapphire substrate instead, the absorbance is calculated by using Eq. B.1, and feeding the literature value for the dielectric function of the WS_2 and the literature values for the refractive index of the sapphire [150]. The selective absorbance for the monolayer WS_2 placed on the sapphire substrate as a function of photon energy is also reported in Fig. B.2 with the red trace.

When comparing the two spectra, it is clearly evident that the absorbance for the monolayer on the Si/SiO_2 substrate is quenched in the UV and enhanced in the visible region of the spectra with respect to the sample on the sapphire substrate. Considering that the complex dielectric function ε_{WS_2} used to calculate the two absorbance spectra is the same in both cases, the different absorbance for different photon energies arises primarily because of the layered structure of the substrate and the corresponding interference at the multiple interfaces, as already mentioned in the main text, section 6.1.2.

Nevertheless, once the absorbance spectra are calculated, the procedure to calculate the effective absorbance and the initial photoexcited quasiparticle density is analogous to the procedure described before. The effective absorbance for above-resonance pumping, given by the integral over the energy of the multiplication of absorbance and nomalized pump lineshape, returns values of 10% for the sapphire substrate, and only 1.8% for the case of the Si/SiO_2 substrate. A one order of magnitude difference in effective absorbance between two same samples but with different substrates clearly shows how great care must be taken when calculating the excited quasiparticle density when working with monolayers TMDC, especially when using layered substrates.

Finally, the absorbed photon density is obtained by multiplicating of the incident fluence and the effective absorbance. In the case of the above-resonance pumping the initial photoexcited quasiparticle density corresponds to two times the absorbed photon density due to the fact that for every absorbed photon, a quasi free electron and a hole are generated.

Bibliography

[1] M. Faraday. *Experimental Researches in Electricity, Volume 1*. London, 1839.

[2] John L. Gustafson. "Moore's Law". In: *Encyclopedia of Parallel Computing*. Ed. by David Padua. Boston, MA: Springer US, 2011, pp. 1177–1184. ISBN: 978-0-387-09766-4. DOI: 10.1007/978-0-387-09766-4_81. URL: https://doi.org/10.1007/978-0-387-09766-4_81.

[3] R.W. Keyes. "Fundamental limits of silicon technology". In: *Proceedings of the IEEE* 89.3 (2001), pp. 227–239. DOI: 10.1109/5.915372.

[4] Igor L. Markov. "Limits on fundamental limits to computation". In: *Nature* 512.7513 (2014), pp. 147–154. DOI: 10.1038/nature13570. URL: https://doi.org/10.1038/nature13570.

[5] Deji Akinwande et al. "Graphene and two-dimensional materials for silicon technology". In: *Nature* 573.7775 (2019), pp. 507–518. DOI: 10.1038/s41586-019-1573-9. URL: https://doi.org/10.1038/s41586-019-1573-9.

[6] Gang Wang et al. "Colloquium: Excitons in atomically thin transition metal dichalcogenides". In: *Rev. Mod. Phys.* 90 (2 2018), p. 021001. DOI: 10.1103/RevModPhys.90.021001. URL: https://link.aps.org/doi/10.1103/RevModPhys.90.021001.

[7] Deep Jariwala et al. "Emerging Device Applications for Semiconducting Two-Dimensional Transition Metal Dichalcogenides". In: *ACS Nano* 8.2 (2014). PMID: 24476095, pp. 1102–1120. DOI: 10.1021/nn500064s. eprint: https://doi.org/10.1021/nn500064s. URL: https://doi.org/10.1021/nn500064s.

[8] Manish Chhowalla, Debdeep Jena, and Hua Zhang. "Two-dimensional semiconductors for transistors". In: *Nature Reviews Materials* 1.11 (2016), p. 16052. DOI: 10.1038/natrevmats.2016.52. URL: https://doi.org/10.1038/natrevmats.2016.52.

[9] Sohail Ahmed and Jiabao Yi. "Two-Dimensional Transition Metal Dichalcogenides and Their Charge Carrier Mobilities in Field-Effect Transistors". In: *Nano-Micro Letters* 9.4 (2017), p. 50. DOI: 10.1007/s40820-017-0152-6. URL: https://doi.org/10.1007/s40820-017-0152-6.

[10] Kin Fai Mak et al. "Atomically Thin MoS_2: A New Direct-Gap Semiconductor". In: *Phys. Rev. Lett.* 105 (13 2010), p. 136805. DOI: 10.1103/PhysRevLett.105.136805. URL: https://link.aps.org/doi/10.1103/PhysRevLett.105.136805.

[11] B. Radisavljevic et al. “Single-layer MoS2 transistors”. In: *Nature Nanotechnology* 6.3 (2011), pp. 147–150. DOI: 10.1038/nnano.2010.279. URL: https://doi.org/10.1038/nnano.2010.279.

[12] Sujay B. Desai et al. “MoS₂ transistors with 1-nanometer gate lengths”. In: *Science* 354.6308 (2016), pp. 99–102. DOI: 10.1126/science.aah4698. eprint: https://www.science.org/doi/pdf/10.1126/science.aah4698. URL: https://www.science.org/doi/abs/10.1126/science.aah4698.

[13] Tong Wu and Jing Guo. “Multiobjective Design of 2-D-Material-Based Field-Effect Transistors With Machine Learning Methods”. In: *IEEE Transactions on Electron Devices* 68.11 (2021), pp. 5476–5482. DOI: 10.1109/TED.2021.3085701.

[14] P. Dawson et al. “Free excitons in room-temperature photoluminescence of GaAs-$Al_xGa_{1-x}As$ multiple quantum wells”. In: *Phys. Rev. B* 28 (12 1983), pp. 7381–7383. DOI: 10.1103/PhysRevB.28.7381. URL: https://link.aps.org/doi/10.1103/PhysRevB.28.7381.

[15] Deep Jariwala et al. “Emerging Device Applications for Semiconducting Two-Dimensional Transition Metal Dichalcogenides”. In: *ACS Nano* 8.2 (2014). PMID: 24476095, pp. 1102–1120. DOI: 10.1021/nn500064s. eprint: https://doi.org/10.1021/nn500064s. URL: https://doi.org/10.1021/nn500064s.

[16] Fengnian Xia et al. “Two-dimensional material nanophotonics”. In: *Nature Photonics* 8.12 (2014), pp. 899–907. DOI: 10.1038/nphoton.2014.271. URL: https://doi.org/10.1038/nphoton.2014.271.

[17] Veluru Jagadeesh Babu et al. “Review of one-dimensional and two-dimensional nanostructured materials for hydrogen generation”. In: *Phys. Chem. Chem. Phys.* 17 (5 2015), pp. 2960–2986. DOI: 10.1039/C4CP04245J. URL: http://dx.doi.org/10.1039/C4CP04245J.

[18] Kartikey Thakar and Saurabh Lodha. “Optoelectronic and photonic devices based on transition metal dichalcogenides”. In: *Materials Research Express* 7.1 (2020), p. 014002. DOI: 10.1088/2053-1591/ab5c9c. URL: https://doi.org/10.1088/2053-1591/ab5c9c.

[19] Suresh C Pillai and Priyanka Ganguly, eds. *2D Materials for Energy Storage and Conversion*. 2053-2563. IOP Publishing, 2021. ISBN: 978-0-7503-3319-1. DOI: 10.1088/978-0-7503-3319-1. URL: https://dx.doi.org/10.1088/978-0-7503-3319-1.

[20] Jiacheng Cao et al. “Recent Development of Gas Sensing Platforms Based on 2D Atomic Crystals”. In: *Research* 2021 (2021), p. 9863038. DOI: 10.34133/2021/9863038. URL: https://doi.org/10.34133/2021/9863038.

[21] John R. Schaibley et al. "Valleytronics in 2D materials". In: *Nature Reviews Materials* 1.11 (2016), p. 16055. DOI: 10.1038/natrevmats.2016.55. URL: https://doi.org/10.1038/natrevmats.2016.55.

[22] Sage R Bauers et al. "Metal chalcogenides for neuromorphic computing: emerging materials and mechanisms". In: *Nanotechnology* 32.37 (2021), p. 372001. DOI: 10.1088/1361-6528/abfa51. URL: https://doi.org/10.1088/1361-6528/abfa51.

[23] Archana Raja et al. "Coulomb engineering of the bandgap and excitons in two-dimensional materials". In: *Nature Communications* 8.1 (2017), p. 15251. DOI: 10.1038/ncomms15251. URL: https://doi.org/10.1038/ncomms15251.

[24] "Two-Dimensional Transition-Metal Dichalcogenides Alexander V. Kolobov and Junji Tominaga: Springer, 2016 538 pages, 229.00(*e* − *book*179.00) ISBN 978-3-319-31449-5". In: *MRS Bulletin* 42.6 (2017), 471–471. DOI: 10.1557/mrs.2017.135.

[25] Andrey R. Klots et al. "Controlled dynamic screening of excitonic complexes in 2D semiconductors". In: *Scientific Reports* 8.1 (2018), p. 768. DOI: 10.1038/s41598-017-18803-y. URL: https://doi.org/10.1038/s41598-017-18803-y.

[26] Alexey Chernikov et al. "Electrical Tuning of Exciton Binding Energies in Monolayer WS_2". In: *Phys. Rev. Lett.* 115 (12 2015), p. 126802. DOI: 10.1103/PhysRevLett.115.126802. URL: https://link.aps.org/doi/10.1103/PhysRevLett.115.126802.

[27] Eva A. A. Pogna et al. "Photo-Induced Bandgap Renormalization Governs the Ultrafast Response of Single-Layer MoS2". In: *ACS Nano* 10.1 (2016). PMID: 26691058, pp. 1182–1188. DOI: 10.1021/acsnano.5b06488. eprint: https://doi.org/10.1021/acsnano.5b06488. URL: https://doi.org/10.1021/acsnano.5b06488.

[28] Sheng Li. *Semiconductor Physical Electronics*. Berlin, Heidelberg: Springer-Verlag, 2006. ISBN: 0387288937.

[29] L. Gierster, S. Vempati, and J. Stähler. "Ultrafast generation and decay of a surface metal". In: *Nature Communications* 12.1 (2021), p. 978. DOI: 10.1038/s41467-021-21203-6. URL: https://doi.org/10.1038/s41467-021-21203-6.

[30] Paul D. Cunningham et al. "Photoinduced Bandgap Renormalization and Exciton Binding Energy Reduction in WS2". In: *ACS Nano* 11.12 (2017). PMID: 29227085, pp. 12601–12608. DOI: 10.1021/acsnano.7b06885. eprint: https://doi.org/10.1021/acsnano.7b06885. URL: https://doi.org/10.1021/acsnano.7b06885.

[31] E. J. Sie et al. "Observation of Exciton Redshift–Blueshift Crossover in Monolayer WS2". In: *Nano Letters* 17.7 (2017). PMID: 28621953, pp. 4210–4216. DOI: 10.1021/acs.nanolett.7b01034. eprint: https://doi.org/10.1021/acs.nanolett.7b01034. URL: https://doi.org/10.1021/acs.nanolett.7b01034.

[32] Claudia Ruppert et al. "The Role of Electronic and Phononic Excitation in the Optical Response of Monolayer WS2 after Ultrafast Excitation". In: *Nano Letters* 17.2 (Feb. 2017), pp. 644–651. DOI: 10.1021/acs.nanolett.6b03513. URL: https://doi.org/10.1021/acs.nanolett.6b03513.

[33] Alexey Chernikov et al. "Population inversion and giant bandgap renormalization in atomically thin WS2 layers". In: *Nature Photonics* 9.7 (2015), pp. 466–470. DOI: 10.1038/nphoton.2015.104. URL: https://doi.org/10.1038/nphoton.2015.104.

[34] Chiara Trovatello et al. "The ultrafast onset of exciton formation in 2D semiconductors". In: *Nature Communications* 11.1 (2020), p. 5277. DOI: 10.1038/s41467-020-18835-5. URL: https://doi.org/10.1038/s41467-020-18835-5.

[35] Qiannan Cui et al. "Transient Absorption Microscopy of Monolayer and Bulk WSe2". In: *ACS Nano* 8.3 (Mar. 2014), pp. 2970–2976. DOI: 10.1021/nn500277y. URL: https://doi.org/10.1021/nn500277y.

[36] Timothy C. Berkelbach, Mark S. Hybertsen, and David R. Reichman. "Theory of neutral and charged excitons in monolayer transition metal dichalcogenides". In: *Phys. Rev. B* 88 (4 2013), p. 045318. DOI: 10.1103/PhysRevB.88.045318. URL: https://link.aps.org/doi/10.1103/PhysRevB.88.045318.

[37] Sajedeh Manzeli et al. "2D transition metal dichalcogenides". In: *Nature Reviews Materials* 2.8 (2017), p. 17033. DOI: 10.1038/natrevmats.2017.33. URL: https://doi.org/10.1038/natrevmats.2017.33.

[38] K. S. Novoselov et al. "Electric Field Effect in Atomically Thin Carbon Films". In: *Science* 306.5696 (2004), pp. 666–669. DOI: 10.1126/science.1102896. eprint: https://www.science.org/doi/pdf/10.1126/science.1102896. URL: https://www.science.org/doi/abs/10.1126/science.1102896.

[39] Caterina Soldano, Ather Mahmood, and Erik Dujardin. "Production, properties and potential of graphene". In: *Carbon* 48.8 (2010), pp. 2127–2150. ISSN: 0008-6223. DOI: https://doi.org/10.1016/j.carbon.2010.01.058. URL: https://www.sciencedirect.com/science/article/pii/S0008622310000928.

[40] Deji Akinwande et al. "A review on mechanics and mechanical properties of 2D materials—Graphene and beyond". In: *Extreme Mechanics Letters* 13 (2017), pp. 42–77. ISSN: 2352-4316. DOI: https://doi.org/10.1016/j.eml.2017.01.008. URL: https://www.sciencedirect.com/science/article/pii/S235243161630236X.

[41] Maurizio Donarelli and Luca Ottaviano. "2D Materials for Gas Sensing Applications: A Review on Graphene Oxide, MoS2, WS2 and Phosphorene". In: *Sensors* 18.11 (2018). ISSN: 1424-8220. DOI: 10.3390/s18113638. URL: https://www.mdpi.com/1424-8220/18/11/3638.

[42] D. Pacilé et al. "The two-dimensional phase of boron nitride: Few-atomic-layer sheets and suspended membranes". In: *Applied Physics Letters* 92.13 (2008), p. 133107. DOI: 10.1063/1.2903702. eprint: https://doi.org/10.1063/1.2903702. URL: https://doi.org/10.1063/1.2903702.

[43] Fengnian Xia, Han Wang, and Yichen Jia. "Rediscovering black phosphorus as an anisotropic layered material for optoelectronics and electronics". In: *Nature Communications* 5.1 (2014), p. 4458. DOI: 10.1038/ncomms5458. URL: https://doi.org/10.1038/ncomms5458.

[44] Jae Yoon Lee et al. "Two-Dimensional Semiconductor Optoelectronics Based on van der Waals Heterostructures". In: *Nanomaterials* 6.11 (2016). ISSN: 2079-4991. DOI: 10.3390/nano6110193. URL: https://www.mdpi.com/2079-4991/6/11/193.

[45] J.A. Wilson and A.D. Yoffe. "The transition metal dichalcogenides discussion and interpretation of the observed optical, electrical and structural properties". In: *Advances in Physics* 18.73 (1969), pp. 193–335. DOI: 10.1080/00018736900101307. eprint: https://doi.org/10.1080/00018736900101307. URL: https://doi.org/10.1080/00018736900101307.

[46] Sheneve Z. Butler et al. "Progress, Challenges, and Opportunities in Two-Dimensional Materials Beyond Graphene". In: *ACS Nano* 7.4 (2013). PMID: 23464873, pp. 2898–2926. DOI: 10.1021/nn400280c. eprint: https://doi.org/10.1021/nn400280c. URL: https://doi.org/10.1021/nn400280c.

[47] Rafael Roldán et al. "Electronic properties of single-layer and multilayer transition metal dichalcogenides MX2 (M = Mo, W and X = S, Se)". In: *Annalen der Physik* 526.9-10 (2014), pp. 347–357. DOI: https://doi.org/10.1002/andp.201400128. eprint: https://onlinelibrary.wiley.com/doi/pdf/10.1002/andp.201400128. URL: https://onlinelibrary.wiley.com/doi/abs/10.1002/andp.201400128.

[48] Yongjie Zhan et al. "Large-Area Vapor-Phase Growth and Characterization of MoS2 Atomic Layers on a SiO2 Substrate". In: *Small* 8.7 (2012), pp. 966–971. DOI: https://doi.org/10.1002/smll.201102654. eprint: https://onlinelibrary.wiley.com/doi/pdf/10.1002/smll.201102654. URL: https://onlinelibrary.wiley.com/doi/abs/10.1002/smll.201102654.

[49] Z. Y. Zhu, Y. C. Cheng, and U. Schwingenschlögl. "Giant spin-orbit-induced spin splitting in two-dimensional transition-metal dichalcogenide semiconductors". In: *Phys. Rev. B* 84 (15 2011), p. 153402. DOI: 10.1103/PhysRevB.84.153402. URL: https://link.aps.org/doi/10.1103/PhysRevB.84.153402.

[50] K. Kośmider, J. W. González, and J. Fernández-Rossier. "Large spin splitting in the conduction band of transition metal dichalcogenide monolayers". In: *Physical Review B* 88.24 (2013). ISSN: 1550-235X. DOI: 10.1103/physrevb.88.245436. URL: http://dx.doi.org/10.1103/PhysRevB.88.245436.

[51] Ting Cao et al. "Valley-selective circular dichroism of monolayer molybdenum disulphide". In: *Nature Communications* 3.1 (2012), p. 887. DOI: 10.1038/ncomms1882. URL: https://doi.org/10.1038/ncomms1882.

[52] E.J. Sie. *Coherent Light-Matter Interactions in Monolayer Transition-Metal Dichalcogenides*. Springer Theses. Springer International Publishing, 2017. ISBN: 9783319695532. URL: https://books.google.de/books?id=6KqNtAEACAAJ.

[53] Robert S. Knox. *Theory of excitons*. New York: Academic Press, 1963. ISBN: 0126077657 9780126077650.

[54] Guowei Zhang et al. "Determination of layer-dependent exciton binding energies in few-layer black phosphorus". In: *Science advances* 4.3 (2018), eaap9977. ISSN: 2375-2548. DOI: 10.1126/sciadv.aap9977. URL: https://europepmc.org/articles/PMC5856490.

[55] J. Frenkel. "On the Transformation of light into Heat in Solids. I". In: *Phys. Rev.* 37 (1 1931), pp. 17–44. DOI: 10.1103/PhysRev.37.17. URL: https://link.aps.org/doi/10.1103/PhysRev.37.17.

[56] Gregory H. Wannier. "The Structure of Electronic Excitation Levels in Insulating Crystals". In: *Phys. Rev.* 52 (3 1937), pp. 191–197. DOI: 10.1103/PhysRev.52.191. URL: https://link.aps.org/doi/10.1103/PhysRev.52.191.

[57] Gwang-Hun Jung, SeokJae Yoo, and Q-Han Park. "Measuring the optical permittivity of two-dimensional materials without a priori knowledge of electronic transitions". In: *Nanophotonics* 8.2 (2019), pp. 263–270. DOI: doi:10.1515/nanoph-2018-0120. URL: https://doi.org/10.1515/nanoph-2018-0120.

[58] Alexey Chernikov et al. "Exciton Binding Energy and Nonhydrogenic Rydberg Series in Monolayer WS_2". In: *Phys. Rev. Lett.* 113 (7 2014), p. 076802. DOI: 10.1103/PhysRevLett.113.076802. URL: https://link.aps.org/doi/10.1103/PhysRevLett.113.076802.

[59] A R Beal, J C Knights, and W Y Liang. "Transmission spectra of some transition metal dichalcogenides. II. Group VIA: trigonal prismatic coordination". In: *Journal of Physics C: Solid State Physics* 5.24 (1972), pp. 3540–3551. DOI: 10.1088/0022-3719/5/24/016. URL: https://doi.org/10.1088/0022-3719/5/24/016.

[60] Diana Y. Qiu, Felipe H. da Jornada, and Steven G. Louie. "Optical Spectrum of MoS_2: Many-Body Effects and Diversity of Exciton States". In: *Phys. Rev. Lett.* 111 (21 2013), p. 216805. DOI: 10.1103/PhysRevLett.111.216805. URL: https://link.aps.org/doi/10.1103/PhysRevLett.111.216805.

[61] Shuo Dong et al. "Direct measurement of key exciton properties: Energy, dynamics, and spatial distribution of the wave function". In: *Natural Sciences* 1.1 (2021). ISSN: 2698-6248. DOI: 10.1002/ntls.10010. URL: http://dx.doi.org/10.1002/ntls.10010.

[62] Xiao-Xiao Zhang et al. "Magnetic brightening and control of dark excitons in monolayer WSe2". In: *Nature Nanotechnology* 12.9 (2017), pp. 883–888. DOI: 10.1038/nnano.2017.105. URL: https://doi.org/10.1038/nnano.2017.105.

[63] Archana Raja et al. "Enhancement of Exciton–Phonon Scattering from Monolayer to Bilayer WS2". In: *Nano Letters* 18.10 (Oct. 2018), pp. 6135–6143. DOI: 10.1021/acs.nanolett.8b01793. URL: https://doi.org/10.1021/acs.nanolett.8b01793.

[64] Wei-Ting Hsu et al. "Dielectric impact on exciton binding energy and quasiparticle bandgap in monolayer WS 2 and WSe 2". In: 6.2 (2019), p. 025028. DOI: 10.1088/2053-1583/ab072a. URL: http://dx.doi.org/10.1088/2053-1583/ab072a.

[65] Bhaskar Kaviraj and Dhirendra Sahoo. "Physics of excitons and their transport in two dimensional transition metal dichalcogenide semiconductors". In: *RSC Advances* 9.44 (2019), pp. 25439–25461. DOI: 10.1039/C9RA03769A. URL: http://dx.doi.org/10.1039/C9RA03769A.

[66] Zhiwei Peng et al. "Strain engineering of 2D semiconductors and graphene: from strain fields to band-structure tuning and photonic applications". In: *Light: Science & Applications* 9.1 (2020), p. 190. DOI: 10.1038/s41377-020-00421-5. URL: https://doi.org/10.1038/s41377-020-00421-5.

[67] Jiani Huang, Thang B. Hoang, and Maiken H. Mikkelsen. "Probing the origin of excitonic states in monolayer WSe2". In: *Scientific Reports* 6.1 (2016), p. 22414. DOI: 10.1038/srep22414. URL: https://doi.org/10.1038/srep22414.

[68] Ampadu P. Wolpert D. *Temperature Effects in Semiconductors.* Springer, New York, NY, 2012. ISBN: 9781461407478. URL: https://doi.org/10.1007/978-1-4614-0748-5_2.

[69] Hsiang-Lin Liu et al. "Temperature-dependent optical constants of monolayer $${\text {MoS}}_2$$, $${\text {MoSe}}_2$$, $${\text {WS}}_2$$, and $${\text {WSe}}_2$$: spectroscopic ellipsometry and first-principles calculations". In: *Scientific Reports* 10.1 (2020), p. 15282. DOI: 10.1038/s41598-020-71808-y. URL: https://doi.org/10.1038/s41598-020-71808-y.

[70] Malte Selig et al. "Excitonic linewidth and coherence lifetime in monolayer transition metal dichalcogenides". In: *Nature Communications* 7.1 (2016), p. 13279. DOI: 10.1038/ncomms13279. URL: https://doi.org/10.1038/ncomms13279.

[71] Weijie Zhao et al. "Origin of Indirect Optical Transitions in Few-Layer MoS2, WS2, and WSe2". In: *Nano Letters* 13.11 (Nov. 2013), pp. 5627–5634. DOI: 10.1021/nl403270k. URL: https://doi.org/10.1021/nl403270k.

[72] Yu Kobayashi et al. "Growth and Optical Properties of High-Quality Monolayer WS2 on Graphite". In: *ACS Nano* 9.4 (Apr. 2015), pp. 4056–4063. DOI: 10.1021/acsnano.5b00103. URL: https://doi.org/10.1021/acsnano.5b00103.

[73] Jason S. Ross et al. "Electrical control of neutral and charged excitons in a monolayer semiconductor". In: *Nature Communications* 4.1 (2013), p. 1474. DOI: 10.1038/ncomms2498. URL: https://doi.org/10.1038/ncomms2498.

[74] Dominik Christiansen et al. "Phonon Sidebands in Monolayer Transition Metal Dichalcogenides". In: *Phys. Rev. Lett.* 119 (18 2017), p. 187402. DOI: 10.1103/PhysRevLett.119.187402. URL: https://link.aps.org/doi/10.1103/PhysRevLett.119.187402.

[75] Galan Moody et al. "Intrinsic homogeneous linewidth and broadening mechanisms of excitons in monolayer transition metal dichalcogenides". In: *Nature Communications* 6.1 (2015), p. 8315. DOI: 10.1038/ncomms9315. URL: https://doi.org/10.1038/ncomms9315.

[76] Archana Raja et al. "Dielectric disorder in two-dimensional materials". In: *Nature Nanotechnology* 14.9 (2019), pp. 832–837. DOI: 10.1038/s41565-019-0520-0. URL: https://doi.org/10.1038/s41565-019-0520-0.

[77] Kathleen M. McCreary et al. "The Effect of Preparation Conditions on Raman and Photoluminescence of Monolayer WS2". In: *Scientific Reports* 6.1 (2016), p. 35154. DOI: 10.1038/srep35154. URL: https://doi.org/10.1038/srep35154.

[78] Soohyung Park et al. "Direct determination of monolayer MoS2and WSe2exciton binding energies on insulating and metallic substrates". In: *2D Materials* 5.2 (2018), p. 025003. DOI: 10.1088/2053-1583/aaa4ca. URL: https://doi.org/10.1088/2053-1583/aaa4ca.

[79] Yuxuan Lin et al. "Dielectric Screening of Excitons and Trions in Single-Layer MoS2". In: *Nano Letters* 14.10 (2014). PMID: 25216267, pp. 5569–5576. DOI: 10.1021/nl501988y. eprint: https://doi.org/10.1021/nl501988y. URL: https://doi.org/10.1021/nl501988y.

[80] Wei-Ting Hsu et al. "Dielectric impact on exciton binding energy and quasiparticle bandgap in monolayer WS2and WSe2". In: 6.2 (2019), p. 025028. DOI: 10.1088/2053-1583/ab072a. URL: https://doi.org/10.1088/2053-1583/ab072a.

[81] Nikola Šibalić and Charles S Adams. *Rydberg Physics*. 2399-2891. IOP Publishing, 2018. ISBN: 978-0-7503-1635-4. DOI: 10.1088/978-0-7503-1635-4. URL: https://dx.doi.org/10.1088/978-0-7503-1635-4.

[82] D. R. Wake et al. "Response of excitonic absorption spectra to photoexcited carriers in GaAs quantum wells". In: *Phys. Rev. B* 46 (20 1992), pp. 13452–13460. DOI: 10.1103/PhysRevB.46.13452. URL: https://link.aps.org/doi/10.1103/PhysRevB.46.13452.

[83] K. Güven and B. Tanatar. "Simplified calculations of band-gap renormalization in quantum-wells". In: *Superlattices and Microstructures* 20.1 (1996), pp. 81–85. ISSN: 0749-6036. DOI: https://doi.org/10.1006/spmi.1996.0052. URL: https://www.sciencedirect.com/science/article/pii/S074960369690052X.

[84] Falco Hüser, Thomas Olsen, and Kristian S. Thygesen. "Quasiparticle GW calculations for solids, molecules, and two-dimensional materials". In: *Phys. Rev. B* 87 (23 2013), p. 235132. DOI: 10.1103/PhysRevB.87.235132. URL: https://link.aps.org/doi/10.1103/PhysRevB.87.235132.

[85] Hongliang Shi et al. "Quasiparticle band structures and optical properties of strained monolayer MoS_2 and WS_2". In: *Phys. Rev. B* 87 (15 2013), p. 155304. DOI: 10.1103/PhysRevB.87.155304. URL: https://link.aps.org/doi/10.1103/PhysRevB.87.155304.

[86] Tawinan Cheiwchanchamnangij and Walter R. L. Lambrecht. "Quasiparticle band structure calculation of monolayer, bilayer, and bulk MoS_2". In: *Phys. Rev. B* 85 (20 2012), p. 205302. DOI: 10.1103/PhysRevB.85.205302. URL: https://link.aps.org/doi/10.1103/PhysRevB.85.205302.

[87] A. Steinhoff et al. "Influence of Excited Carriers on the Optical and Electronic Properties of MoS2". In: *Nano Letters* 14.7 (2014). PMID: 24956358, pp. 3743–3748. DOI: 10.1021/nl500595u. eprint: https://doi.org/10.1021/nl500595u. URL: https://doi.org/10.1021/nl500595u.

[88] G. W. Fehrenbach et al. "Transient Optical Spectra of a Dense Exciton Gas in a Direct-Gap Semiconductor". In: *Phys. Rev. Lett.* 49 (17 1982), pp. 1281–1284. DOI: 10.1103/PhysRevLett.49.1281. URL: https://link.aps.org/doi/10.1103/PhysRevLett.49.1281.

[89] Daniel Wegkamp. "Ultrafast electron dynamics and the role of screening". PhD thesis. 2015. URL: http://dx.doi.org/10.17169/refubium-7587.

[90] A. Steinhoff et al. "Exciton fission in monolayer transition metal dichalcogenide semiconductors". In: *Nature Communications* 8.1 (2017), p. 1166. DOI: 10.1038/s41467-017-01298-6. URL: https://doi.org/10.1038/s41467-017-01298-6.

[91] Olaf Stenzel. *The Physics of Thin Film Optical Spectra*. Springer-Verlag Berlin Heidelberg, 2005.

[92] E. Hecht. *Optics*. Pearson, 2012. ISBN: 9788131718070. URL: https://books.google.de/books?id=wcMWpBMMzIkC.

[93] Yilei Li and Tony F Heinz. "Two-dimensional models for the optical response of thin films". In: *2D Materials* 5.2 (2018), p. 025021. DOI: 10.1088/2053-1583/aab0cf. URL: https://doi.org/10.1088/2053-1583/aab0cf.

[94] Nikolai Christian Passler, Mathieu Jeannin, and Alexander Paarmann. "Layer-resolved absorption of light in arbitrarily anisotropic heterostructures". In: *Phys. Rev. B* 101.165425 (2020).

[95] Albert Einstein. "Zur Quantentheorie der Strahlung". In: *Phys. Z.* 18 (1917), pp. 121–128.

[96] Amnon. Yariv. *Quantum electronics*. eng. 3rd ed. New York: Wiley, 1989. ISBN: 0471617717.

[97] Rodney Loudon. *The Quantum Theory of Light*. Oxford: Clarendon Press, 1973. URL: https://cds.cern.ch/record/105699.

[98] Selene Mor. "Fundamental interactions governing the (non-)equilibrium electronic structure in low dimensions". In: 2019.

[99] Laura Foglia. "Ultrafast dynamics and energy loss channels at a hybrid organic inorganic interface". Doctoral Thesis. Berlin: Technische Universität Berlin, 2015. DOI: 10.14279/depositonce-4907. URL: http://dx.doi.org/10.14279/depositonce-4907.

[100] D. E. Spence, P. N. Kean, and W. Sibbett. "60-fsec pulse generation from a self-mode-locked Ti:sapphire laser". In: *Opt. Lett.* 16.1 (1991), pp. 42–44. DOI: 10.1364/OL.16.000042. URL: http://ol.osa.org/abstract.cfm?URI=ol-16-1-42.

[101] R. L. Fork, O. E. Martinez, and J. P. Gordon. "Negative dispersion using pairs of prisms". In: *Opt. Lett.* 9.5 (1984), pp. 150–152. DOI: 10.1364/OL.9.000150. URL: http://ol.osa.org/abstract.cfm?URI=ol-9-5-150.

[102] O. Martinez. "Design of high-power ultrashort pulse amplifiers by expansion and recompression". In: *IEEE Journal of Quantum Electronics* 23.8 (1987), pp. 1385–1387. DOI: 10.1109/JQE.1987.1073518.

[103] Robert W. Boyd. "Chapter 1 - The Nonlinear Optical Susceptibility". In: *Nonlinear Optics (Third Edition)*. Ed. by Robert W. Boyd. Third Edition. Burlington: Academic Press, 2008, pp. 1–67. ISBN: 978-0-12-369470-6. DOI: https://doi.org/10.1016/B978-0-12-369470-6.00001-0. URL: https://www.sciencedirect.com/science/article/pii/B9780123694706000010.

[104] D. Wegkamp et al. "Phase retrieval and compression of low-power white-light pulses". In: *Applied Physics Letters* 99.10 (2011), p. 101101. DOI: 10.1063/1.3635396. eprint: https://doi.org/10.1063/1.3635396. URL: https://doi.org/10.1063/1.3635396.

[105] Alexander L. Gaeta. "Catastrophic Collapse of Ultrashort Pulses". In: *Phys. Rev. Lett.* 84 (16 2000), pp. 3582–3585. DOI: 10.1103/PhysRevLett.84.3582. URL: https://link.aps.org/doi/10.1103/PhysRevLett.84.3582.

[106] M. Bradler, P. Baum, and E. Riedle. "Femtosecond continuum generation in bulk laser host materials with sub-microJ pump pulses". In: *Applied Physics B* 97.3 (2009), p. 561. DOI: 10.1007/s00340-009-3699-1. URL: https://doi.org/10.1007/s00340-009-3699-1.

[107] Federico Cilento et al. "Ultrafast insulator-to-metal phase transition as a switch to measure the spectrogram of a supercontinuum light pulse". In: *Applied Physics Letters* 96.2 (2010), p. 021102. DOI: 10.1063/1.3291105. eprint: https://doi.org/10.1063/1.3291105. URL: https://doi.org/10.1063/1.3291105.

[108] Erik Zeek et al. "Pulse compression by use of deformable mirrors". In: *Opt. Lett.* 24.7 (1999), pp. 493–495. DOI: 10.1364/OL.24.000493. URL: http://ol.osa.org/abstract.cfm?URI=ol-24-7-493.

[109] Santanu Das et al. "Synthesis, Properties, and Applications of 2-D Materials: A Comprehensive Review". In: *Critical Reviews in Solid State and Materials Sciences* 39.4 (2014), pp. 231–252. DOI: 10.1080/10408436.2013.836075. eprint: https://doi.org/10.1080/10408436.2013.836075. URL: https://doi.org/10.1080/10408436.2013.836075.

[110] Jin Liu et al. "A comprehensive comparison study on the vibrational and optical properties of CVD-grown and mechanically exfoliated few-layered WS2". In: *J. Mater. Chem. C* 5 (43 2017), pp. 11239–11245. DOI: 10.1039/C7TC02831H. URL: http://dx.doi.org/10.1039/C7TC02831H.

[111] Fang Liu et al. "Direct Determination of Band-Gap Renormalization in the Photoexcited Monolayer MoS_2". In: *Phys. Rev. Lett.* 122 (24 2019), p. 246803. DOI: 10.1103/PhysRevLett.122.246803. URL: https://link.aps.org/doi/10.1103/PhysRevLett.122.246803.

[112] Sujay B. Desai et al. "Gold-Mediated Exfoliation of Ultralarge Optoelectronically-Perfect Monolayers". In: *Advanced Materials* 28.21 (2016), pp. 4053–4058. DOI: https://doi.org/10.1002/adma.201506171. eprint: https://onlinelibrary.wiley.com/doi/pdf/10.1002/adma.201506171. URL: https://onlinelibrary.wiley.com/doi/abs/10.1002/adma.201506171.

[113] Malte Selig et al. "Ultrafast dynamics in monolayer transition metal dichalcogenides: Interplay of dark excitons, phonons, and intervalley exchange". In: *Phys. Rev. Research* 1 (2 2019), p. 022007. DOI: 10.1103/PhysRevResearch.1.022007. URL: https://link.aps.org/doi/10.1103/PhysRevResearch.1.022007.

[114] Zeynep Ezgi Eroglu et al. "Ultrafast dynamics of exciton formation and decay in two-dimensional tungsten disulfide (2D-WS2) monolayers". In: *Phys. Chem. Chem. Phys.* 22 (30 2020), pp. 17385–17393. DOI: 10.1039/D0CP03220D. URL: http://dx.doi.org/10.1039/D0CP03220D.

[115] Fang Liu et al. "Direct Determination of Band-Gap Renormalization in the Photoexcited Monolayer ${\mathrm{MoS}}_{2}$". In: *Physical Review Letters* 122.24 (June 2019), pp. 246803–. DOI: 10.1103/PhysRevLett.122.246803. URL: https://link.aps.org/doi/10.1103/PhysRevLett.122.246803.

[116] Stefano Calati et al. "Ultrafast evolution of the complex dielectric function of monolayer WS2 after photoexcitation". In: *Phys. Chem. Chem. Phys.* 23 (39 2021), pp. 22640–22646. DOI: 10.1039/D1CP03437E. URL: http://dx.doi.org/10.1039/D1CP03437E.

[117] Narges Ansari and Farinaz Ghorbani. "Light absorption optimization in two-dimensional transition metal dichalcogenide van der Waals heterostructures". In: *J. Opt. Soc. Am. B* 35.5 (2018), pp. 1179–1185. DOI: 10.1364/JOSAB.35.001179. URL: http://josab.osa.org/abstract.cfm?URI=josab-35-5-1179.

[118] I. H. Malitson. "Interspecimen Comparison of the Refractive Index of Fused Silica*,†". In: *J. Opt. Soc. Am.* 55.10 (1965), pp. 1205–1209. DOI: 10.1364/JOSA.55.001205. URL: http://www.osapublishing.org/abstract.cfm?URI=josa-55-10-1205.

[119] Martin Weismann and Nicolae C. Panoiu. "Theoretical and computational analysis of second- and third-harmonic generation in periodically patterned graphene and transition-metal dichalcogenide monolayers". In: *Phys. Rev. B* 94.035435 (2016), p. 035435.

[120] Liang Guo et al. "Lineshape characterization of excitons in monolayer WS2 by two-dimensional electronic spectroscopy". In: *Nanoscale Adv.* 2 (6 2020), pp. 2333–2338. DOI: 10.1039/D0NA00240B. URL: http://dx.doi.org/10.1039/D0NA00240B.

[121] Jin Liu et al. "A comprehensive comparison study on the vibrational and optical properties of CVD-grown and mechanically exfoliated few-layered WS2". In: *J. Mater. Chem. C* 5 (43 2017), pp. 11239–11245. DOI: 10.1039/C7TC02831H. URL: http://dx.doi.org/10.1039/C7TC02831H.

[122] Farhan Rana, Okan Koksal, and Christina Manolatou. "Many-body theory of the optical conductivity of excitons and trions in two-dimensional materials". In: *Phys. Rev. B* 102 (8 2020), p. 085304. DOI: 10.1103/PhysRevB.102.085304. URL: https://link.aps.org/doi/10.1103/PhysRevB.102.085304.

[123] Dmitry K. Efimkin and Allan H. MacDonald. "Many-body theory of trion absorption features in two-dimensional semiconductors". In: *Phys. Rev. B* 95 (3 2017), p. 035417. DOI: 10.1103/PhysRevB.95.035417. URL: https://link.aps.org/doi/10.1103/PhysRevB.95.035417.

[124] G. Wang et al. "Valley dynamics probed through charged and neutral exciton emission in monolayer ${\mathrm{WSe}}_{2}$". In: *Physical Review B* 90.7 (Aug. 2014), pp. 075413–. DOI: 10.1103/PhysRevB.90.075413. URL: https://link.aps.org/doi/10.1103/PhysRevB.90.075413.

[125] D. E. Aspnes and A. A. Studna. "Dielectric functions and optical parameters of Si, Ge, GaP, GaAs, GaSb, InP, InAs, and InSb from 1.5 to 6.0 eV". In: *Phys. Rev. B* 27 (2 1983), pp. 985–1009. DOI: 10.1103/PhysRevB.27.985. URL: https://link.aps.org/doi/10.1103/PhysRevB.27.985.

[126] Stefano Calati et al. *Dynamic screening of quasiparticles in WS_2 monolayers*. 2022. DOI: 10.48550/ARXIV.2204.02125. URL: https://arxiv.org/abs/2204.02125.

[127] N. Del Fatti et al. "Temperature-dependent electron-lattice thermalization in GaAs". In: *Phys. Rev. B* 59 (7 1999), pp. 4576–4579. DOI: 10.1103/PhysRevB.59.4576. URL: https://link.aps.org/doi/10.1103/PhysRevB.59.4576.

[128] Paul D. Cunningham et al. "Resonant optical Stark effect in monolayer WS2". In: *Nature Communications* 10.1 (2019), p. 5539. DOI: 10.1038/s41467-019-13501-x. URL: https://doi.org/10.1038/s41467-019-13501-x.

[129] Edbert J. Sie et al. "Valley-selective optical Stark effect in monolayer WS2". In: *Nature Materials* 14.3 (2015), pp. 290–294. DOI: 10.1038/nmat4156. URL: https://doi.org/10.1038/nmat4156.

[130] Malte Selig et al. "Dark and bright exciton formation, thermalization, and photoluminescence in monolayer transition metal dichalcogenides". In: 5.3 (2018), p. 035017. DOI: 10.1088/2053-1583/aabea3. URL: http://dx.doi.org/10.1088/2053-1583/aabea3.

[131] Robert Wallauer et al. "Momentum-Resolved Observation of Exciton Formation Dynamics in Monolayer WS2". In: *Nano Letters* 21.13 (2021). PMID: 34165994, pp. 5867–5873. DOI: 10.1021/acs.nanolett.1c01839. eprint: https://doi.org/10.1021/acs.nanolett.1c01839. URL: https://doi.org/10.1021/acs.nanolett.1c01839.

[132] Kin Fai Mak et al. "Tightly bound trions in monolayer MoS2". In: *Nature Materials* 12.3 (2013), pp. 207–211. DOI: 10.1038/nmat3505. URL: https://doi.org/10.1038/nmat3505.

[133] Bo Liu et al. "Engineering Bandgaps of Monolayer MoS2 and WS2 on Fluoropolymer Substrates by Electrostatically Tuned Many-Body Effects". In: *Advanced Materials* 28.30 (2016), pp. 6457–6464. DOI: https://doi.org/10.1002/adma.201504876. eprint: https://onlinelibrary.wiley.com/doi/pdf/10.1002/adma.201504876. URL: https://onlinelibrary.wiley.com/doi/abs/10.1002/adma.201504876.

[134] Dezheng Sun et al. "Observation of Rapid Exciton–Exciton Annihilation in Monolayer Molybdenum Disulfide". In: *Nano Letters* 14.10 (Oct. 2014), pp. 5625–5629. DOI: 10.1021/nl5021975. URL: https://doi.org/10.1021/nl5021975.

[135] Paul D. Cunningham, Kathleen M. McCreary, and Berend T. Jonker. "Auger Recombination in Chemical Vapor Deposition-Grown Monolayer WS2". In: *The Journal of Physical Chemistry Letters* 7.24 (2016). PMID: 27973899, pp. 5242–5246. DOI: 10.1021/acs.jpclett.6b02413. eprint: https://doi.org/10.1021/acs.jpclett.6b02413. URL: https://doi.org/10.1021/acs.jpclett.6b02413.

[136] Yiling Yu et al. "Fundamental limits of exciton-exciton annihilation for light emission in transition metal dichalcogenide monolayers". In: *Phys. Rev. B* 93 (20 2016), p. 201111. DOI: 10.1103/PhysRevB.93.201111. URL: https://link.aps.org/doi/10.1103/PhysRevB.93.201111.

[137] Shuangping Han et al. "Incoherent phonon population and exciton-exciton annihilation dynamics in monolayer WS2 revealed by time-resolved Resonance Raman scattering". In: *Optics Express* 27.21 (2019), pp. 29949–29961. DOI: 10.1364/OE.27.029949. URL: http://www.opticsexpress.org/abstract.cfm?URI=oe-27-21-29949.

[138] Yang Fu et al. "Effect of Dielectric Environment on Excitonic Dynamics in Monolayer WS2". In: *Advanced Materials Interfaces* 6.23 (2019), p. 1901307. DOI: https://doi.org/10.1002/admi.201901307. eprint: https://onlinelibrary.wiley.com/doi/pdf/10.1002/admi.201901307. URL: https://onlinelibrary.wiley.com/doi/abs/10.1002/admi.201901307.

[139] Maurizia Palummo, Marco Bernardi, and Jeffrey C. Grossman. "Exciton Radiative Lifetimes in Two-Dimensional Transition Metal Dichalcogenides". In: *Nano Letters* 15.5 (May 2015), pp. 2794–2800. DOI: 10.1021/nl503799t. URL: https://doi.org/10.1021/nl503799t.

[140] Haining Wang et al. "Fast exciton annihilation by capture of electrons or holes by defects via Auger scattering in monolayer metal dichalcogenides". In: *Physical Review B* 91.16 (Apr. 2015), pp. 165411–. DOI: 10.1103/PhysRevB.91.165411. URL: https://link.aps.org/doi/10.1103/PhysRevB.91.165411.

[141] C. Poellmann et al. "Resonant internal quantum transitions and femtosecond radiative decay of excitons in monolayer WSe2". In: *Nature Materials* 14.9 (2015), pp. 889–893. DOI: 10.1038/nmat4356. URL: https://doi.org/10.1038/nmat4356.

[142] Frank Ceballos et al. "Exciton formation in monolayer transition metal dichalcogenides". In: *Nanoscale* 8 (22 2016), pp. 11681–11688. DOI: 10.1039/C6NR02516A. URL: http://dx.doi.org/10.1039/C6NR02516A.

[143] Fabio Caruso. "Nonequilibrium Lattice Dynamics in Monolayer MoS2". In: *The Journal of Physical Chemistry Letters* 12.6 (Feb. 2021), pp. 1734–1740. DOI: 10.1021/acs.jpclett.0c03616. URL: https://doi.org/10.1021/acs.jpclett.0c03616.

[144] Philipp Steinleitner et al. "Direct Observation of Ultrafast Exciton Formation in a Monolayer of WSe2". In: *Nano Letters* 17.3 (Mar. 2017), pp. 1455–1460. DOI: 10.1021/acs.nanolett.6b04422. URL: https://doi.org/10.1021/acs.nanolett.6b04422.

[145] Paul D. Cunningham, Kathleen M. McCreary, and Berend T. Jonker. "Auger Recombination in Chemical Vapor Deposition-Grown Monolayer WS2". In: *The Journal of Physical Chemistry Letters* 7.24 (Dec. 2016), pp. 5242–5246. DOI: 10.1021/acs.jpclett.6b02413. URL: https://doi.org/10.1021/acs.jpclett.6b02413.

[146] Yang Fu et al. "Effect of Dielectric Environment on Excitonic Dynamics in Monolayer WS2". In: *Advanced Materials Interfaces* 6.23 (2019), p. 1901307. DOI: https://doi.org/10.1002/admi.201901307.

[147] A. Honold et al. "Collision broadening of two-dimensional excitons in a GaAs single quantum well". In: *Physical Review B* 40.9 (Sept. 1989), pp. 6442–6445. DOI: 10.1103/PhysRevB.40.6442. URL: https://link.aps.org/doi/10.1103/PhysRevB.40.6442.

[148] J. G. Gay. "Screening of Excitons in Semiconductors". In: *Phys. Rev. B* 4 (8 1971), pp. 2567–2575. DOI: 10.1103/PhysRevB.4.2567. URL: https://link.aps.org/doi/10.1103/PhysRevB.4.2567.

[149] Alang Kasim Harman, Susumu Ninomiya, and Sadao Adachi. "Optical constants of sapphire (Al2O3) single crystals". In: *Journal of Applied Physics* 76.12 (1994), pp. 8032–8036. DOI: 10.1063/1.357922.

[150] Raymond L. Kelly. "Program of the 1972 Annual Meeting of the Optical Society of America". In: *J. Opt. Soc. Am.* 62.11 (1972), pp. 1336–1336. DOI: 10.1364/JOSA.62.001336. URL: http://www.osapublishing.org/abstract.cfm?URI=josa-62-11-1336.

Acknowledgements

First of all, I want to reserve an exceptional thank you to Julia, for supervising my project and your huge help in the last few years. Thanks for allowing me to develop new ideas and always providing the needed adjustment and support. I know that sometimes, maybe, especially when I was writing up thesis and papers, you had to cope with some very very long, sometimes even redundant, phrases that I wrote, but other than the jokes, you really guided my development as a scientist and as a person.

I want to thank Martin Wolf for the opportunity he gave me to work in the Fritz-Haber-institute's amazing facilities and in the PC department's stimulant atmosphere. Furthermore, thank you for reviewing my thesis.

The same thanks are extended to the Humboldt University for providing the infrastructures through my last year of PhD. I want to thank Prof. Dr. Oliver Benson for co-supervising my thesis.

A huge thank goes to Selene because you guided me through my first years of PhD, being a mentor scientifically and non-scientifically. In good memory of the long nights in the lab, the dinners and all the DB.

Obviously I need to thank the eDynamiX group, with all its former and present members, because without you the PhD would have been much much harder. Particular thanks to Lukas, Sam, Sarah and Sesha for the very nice and fundamental discussions. Obviously thank to Subhadra for taking forward the work that I started. Not to forget, Angelika, Boubacar, Elsie, Marco, Philipp, Conny, Sergey, Radoslaw, Katarina, Laura thanks to all of you.

I want to thank all the technicians in the FHI. Sven (Always tutti paletti), Albrecht, Daniel, Harald, Joachim, and Reinhard for the technical support and the amazing moments! Obviously, a special mention goes to Marcel because of the constant support in and out of the FHI. Not to forget the PC-sek, Daria and Manuel, I can't even say how much you helped me out. Thanks to all the non-scientific staff of the PC department because you fundamentally contribute to make it the amazing place it is.

Talking of the PC department, many thanks to all the scientific staff as well, I had unforgettable memories with so many people that it is impossible to mention all of them. A few special mentions go to Alex for the good times when sharing the office, obviously Ivana and the cool kidz. Thanks to Ralph and Alex because the discussion with you, either in front of a cigarette or in conferences, lead to some breakthrough of my research.

I want to extend a HUGE thank to the people of Mehringdamm 65, present and past members, with whom I shared a house and always had a place that I looked forward to returning to. Suru, obviously, you became more than a friend and this bond is going to last for very long time. It was wonderful sharing those years with

you, sharing the PhD life and all the marvellous moments that are going to stay with me.

Johannes, I can't thank you enough for how good of a friend and a person you are. The super deep discussion on your terrace and the support you gave me are not quantifiable in words.

I want to thank all the other friends that made my years in Berlin unforgettable: Martina, Paolo, Luc, Kathy, Laura, Dennis, Sophie… all the others! I can't name all of you because you are too many.

And now I switch to Italian…

Grazie Simone, siamo amici da una vita e la distanza non è diventato un problema ma anzi, ci ha forse unito ancora di più. Non è possibile quantificare quanto tu sia stato d'aiuto. Sei una persona speciale.

Grazie a tutti gli amici storici, rendete Brescia un posto meraviglioso in cui tornare. Un ringraziamento alle mie fantastiche sorelle, Nicole, Chiara ed Elena, perché la famiglia è sempre la famiglia e non posso quantificare il bene che vi voglio. Siete speciali. Grazie anche a tutto il resto della famiglia Calati e Fusaro.

Ovviamente per finire mamma e papà, come avrei potuto fare tutto questo senza di voi? Grazie mille per avermi sempre lasciato libero di crescere e prendere la mia strada. Sapere di avere delle fondamenta come voi e un posto dove sentirsi a casa non è descrivibile a parole. Grazie.

And to finish, I am sure that I am forgetting someone, because you know, it's me at the end of the day. I would ultimately thank all of you, aforementioned and not, in person.